REDUCED WAVELENGTH SPECTRAL IMAGING FOR GRADING DEFECT AND ASYMPTOMATIC FUSARIUM DETECTION IN WHITE MAIZE

by

Kate Sendin

Dissertation presented for the degree of
Doctor of Philosophy (Food Science)
in the Faculty of AgriScience at Stellenbosch University

Supervisor: Dr Paul J. Williams

Co-supervisor: Prof. Marena Manley

March 2020

Stellenbosch University https://scholar.sun.ac.za

DECLARATION

By submitting this thesis electronically, I declare that the entirety of the work contained therein is my own, original work, that I am the sole author thereof (save to the extent explicitly otherwise stated), that reproduction and publication thereof by Stellenbosch University will not infringe any third party rights and that I have not previously in its entirety or in part submitted it for obtaining any qualification.

Kate Sendin
March 2020

Copyright © 2020 Stellenbosch University
All rights reserved

Stellenbosch University https://scholar.sun.ac.za

ACKNOWLEDGMENTS

I would like to express my sincere gratitude to my supervisors Dr Paul Williams and Prof. Marena Manley for their continuous support of my research. As my supervisors throughout my five years as a Master's and Doctoral student, your patience, motivation and wisdom were greatly appreciated. Dr Williams, your eagerness to collaborate, travel and take research a step further has enriched my post-graduate experience and has broadened my horizons. Thank you to you both, under your guidance I have grown immeasurably as a scientist and researcher.

I would like to extend my most sincere thanks to the following people and institutions for their contribution to the successful completion of this study:

Dr. Janine Colling for your help with my hyperspectral imaging (not to mention countless hours of your company while sitting at PC4 slogging away at data analysis!);

Wiana Louw, Hannelien Meyer, Ben van der Linde and the graders at the South African Grain Laboratory and Kim O'Kennedy at Pioneer Foods for going out of their way to gather samples on my behalf;

Dr Lindy Rose and her post-graduate assistants at the Department of Plant Pathology, Stellenbosch University for the identification and confirmation of the asymptomatically *Fusarium* infected maize kernels;

All staff and post-graduate students in the Food Science Department for a warm and friendly working environment. I cannot believe that my nine year tenure in the department has finally come to an end! Special thanks to the head of our department, Prof. Gunnar Sigge;

Marguerite Vermeulen for kindly translating my thesis abstract to Afrikaans – jy's 'n engel; and

The National Research Fund (NRF) (Freestanding Doctoral Bursary; Grant number 112569) are hereby acknowledged for financial support (any opinion, findings and conclusions or recommendations expressed in this material are those of the author and therefore the NRF does not accept any liability in regard thereto).

Last but not least, I would like to thank my parents Billy and Heidi, my brother William, my special friends Bronwyn, Keagan, Jessy, Megan, Julia and Marc for their continued support and encouragement (and the occasional welcome distraction) throughout my writing of this thesis.

Stellenbosch University https://scholar.sun.ac.za

ABSTRACT

The aim of this dissertation was to present the South African maize industry with an accurate and affordable automated analytical technique for white maize grading and for identifying asymptomatic *Fusarium* fungal contamination. This was achieved by using near infrared (NIR) hyperspectral imaging, chemometric classification model development, optimal waveband selection and hierarchical modelling.

White maize grade is assigned based on the content of 5 main categories in a maize consignment, namely sound white maize, defective white maize, pinked white maize, yellow maize and foreign materials. Defective white maize and foreign materials comprise further sub-categories, giving a total of 17 classes. All of the categories stipulated in South African maize grading legislation were simultaneously classified (1044 samples; 60 kernels of each class) using NIR hyperspectral imaging and partial least squares discriminant analysis (PLS-DA) models assembled in a hierarchical decision pathway. The hierarchical model divided the task into 25 small steps (binary and ternary PLS-DA models), which progressed from the most easily classified classes to the most difficult. The hierarchical model was based on the full NIR spectrum (288 wavebands) and performed with an overall accuracy of 93.3% for the main categories. The classification of sound white maize (88.3%), pinked white maize (83.3%) and yellow maize (75.0%) should ideally be improved before the method is implemented for industry grading. Pinked white maize and yellow maize are distinguishable due to the presence of anthocyanin and beta-carotene, respectively, which both exhibit maximum absorption in the visible region and do not interact with NIR radiation. The use of a spectral imaging system including the visible region is expected to improve the classification of these classes.

Following the encouraging success of maize grading using the full NIR spectrum, waveband reduction and optimisation was conducted to attempt simplified but accurate grading of white maize using a recalculated hierarchical decision pathway. Three waveband selection techniques were employed, namely waveband windows (48 wavebands), variable importance in projection (VIP) (21 wavebands) and covariance selection (CovSel) (13 wavebands). There was a loss of performance in all three reduced waveband models. The waveband windows (87.1% main category classification accuracy) and VIP waveband sets (84.5% main category classification accuracy) performed with similar classification accuracies across the numerous categories, but the VIP waveband set utilised less than half of the spectral variables. The CovSel waveband set used the fewest wavebands but exhibited an unacceptable loss of classification accuracy (81.9% main category classification accuracy). Overall, the VIP waveband set (964, 1127, 1159, 1323, 1356, 1388, 1421, 1716, 1847, 1879, 1912, 1945, 2043, 2239, 2272, 2305, 2337, 2403, 2435, 2468 and 2501 nm), which was based on only 7.3% of the 288 original spectral variables, was recommended as the best trade-off between instrument performance and expected cost of the system.

A second issue in the South African maize industry was addressed, namely the detection of single asymptomatically *Fusarium* infected kernels. NIR hyperspectral images of 224 visibly sound (healthy) kernels were acquired prior to germination of the kernels in individual sterile containers. Germination caused internal

Stellenbosch University https://scholar.sun.ac.za

Fusarium infections to become visibly identifiable as external fungal growth, which was later confirmed by conventional microbial testing. While only 3.3% of the kernels in the bulk samples exhibited visible rotting symptoms (flagged during visual inspection), 32.1% of germinated kernels were asymptomatically infected and capable of producing harmful fumonisin mycotoxins. Some of these bulk samples contained fumonisin levels of 8 ppm (double the limit) but would have been declared safe for human consumption based on manual inspection methods. This lack of correlation between visible symptoms and safety emphasised the need for additional analytical methods to determine *Fusarium* related risks. The pre-germination spectral images of the uninfected and asymptomatically infected kernels were divided into two classes, and a PLS-DA model classified the maize kernels with a classification accuracy of 67.0%. Considering the high food safety risk associated with fumonisins, NIR hyperspectral imaging is not a viable method for detecting asymptomatic *Fusarium* infections during South African white maize processing.

The results of this study demonstrated that NIR hyper- and multispectral imaging are promising analytical techniques for automated maize grading, but not for the detection of asymptomatic *Fusarium* infection. However, the results of the *Fusarium* germination study provided insight into the status of *Fusarium* infection and fumonisins in the South African maize industry that have not yet appeared in literature and emphasised the need for industry-friendly mycotoxin testing methods.

Stellenbosch University https://scholar.sun.ac.za

OPSOMMING

Die doel van hierdie proefskrif was om die Suid-Afrikaanse mieliebedryf voor te stel aan 'n akkurate en bekostigbare outomatiese analitiese tegniek vir witmielie-gradering en die identifisering van asimptomatiese *Fusarium*-swambesmetting. Dit is bewerkstellig deur gebruik te maak van naby-infrarooi (NIR) hiperspektrale beelding, chemometriese klassifikasies modelontwikkeling, optimale golfband selektering en hiërargiese modellering.

Witmielie-graad word op grond van die inhoud van vyf hoofkategorieë in 'n mieliebesending, naamlik gesonde witmielies, foutiewe witmielies, pienk witmielies, geelmielies en vreemde materiale toegeken. Foutiewe witmielies en vreemde materiale bestaan uit verdere subkategorieë, wat 'n totaal van 17 klasse gee. Al die kategorieë, soos uiteengesit in Suid-Afrikaanse mielie-graderingswetgewing, is gelyktydig geklassifiseer (1044 monsters; 60 pitte van elke klas) deur gebruik te maak van NIR-hiperspektrale beeldvorming en parsiële kleinste kwadrate-diskriminantanalise (PLS-DA) modelle wat in 'n hiërargiese besluitweg saamgestel is. Die hiërargiese model het die taak in 25 klein stappe (binêre en ternêre PLS-DA-modelle) verdeel, wat van die maklikste klassifiseerbare klasse tot die moeilikste gevorder het. Die hiërargiese model was op die volledige NIR-spektrum (288 golfbande) gebaseer en is vir die hoofkategorieë met 'n algehele akkuraatheid van 93.3% uitgevoer. Die klassifikasie van gesonde witmielies (88.3%), pienk witmielies (83.3%) en geelmielies (75.0%) moet verkieslik verbeter word voordat die metode vir industrie-gradering geïmplementeer word. Pienk witmielies en geelmielies kan as gevolg van die teenwoordigheid van antosianien en beta-karoteen, respektiewelik, onderskei word wat beide 'n maksimum absorpsie in die sigbare gebied het en nie ‘n interaksie met NIR-bestraling het nie. Die gebruik van 'n spektrale beeldstelsel, insluitend die sigbare streek, sal na verwagting die klassifikasie van hierdie klasse verbeter.

Na die bemoedigende sukses van mielie-gradering deur die volledige NIR-spektrum te gebruik, is golfbandvermindering en -optimalisering gedoen om 'n vereenvoudigde, maar noukeurige gradering van witmielies te bewerkstellig met behulp van 'n herberekende hiërargiese besluitneming. Drie golfbandseleksietegnieke is aangewend, naamlik golfbandvensters (48 golfbande), veranderlike belang in projeksie (VIP) (21 golfbande) en seleksie van kovariansie (CovSel) (13 golfbande). Daar was in al drie die golfbandmodelle 'n verlies aan prestasie. Die golfbandvensters (87.1% van die hoofkategorie-klassifikasie-akkuraatheid) en VIP-golfbandstelle (84,5% van die hoofkategorie-klassifikasie-akkuraatheid) is uitgevoer met soortgelyke klassifikasie-akkuraatheid in die verskillende kategorieë, maar die VIP-golfbandstel het minder as die helfte van die spektrale veranderlikes gebruik. Die CovSel-golfbandstel het die minste golfbande gebruik, maar het 'n onaanvaarbare verlies aan klassifikasie-akkuraatheid getoon (81.9% in die hoofkategorie-klassifikasie-akkuraatheid). In die algemeen is die VIP-golfbandstel (964, 1127, 1159, 1323, 1356, 1388, 1421, 1716, 1847, 1879, 1912, 1945, 2043, 2239, 2272, 2305, 2337, 2403, 2435, 2468 en 2501 nm), wat op slegs 7,3% van die 288 oorspronklike spektrale veranderlikes gebaseer was, is aanbeveel as die beste inruiling tussen instrumentprestasie en die verwagte koste van die stelsel.

Stellenbosch University https://scholar.sun.ac.za

'n Tweede kwessie in die Suid-Afrikaanse mieliebedryf is geadresseer, naamlik die opsporing van enkele asimptomaties *Fusarium*-besmette pitte. NIR hiperspektrale beelde van 224 sigbare (gesonde) pitte is verkry voor die pitte, in individuele steriele houers, ontkieming ondergaan het. Ontkieming het veroorsaak dat interne *Fusarium*-infeksies sigbaar identifiseerbaar word as eksterne swamgroei, wat later deur konvensionele mikrobiese toetsing bevestig is. Alhoewel slegs 3.3% van die pitte in die massamonsters sigbare verrottingsimptome vertoon het (wat tydens visuele inspeksie gemerk is), was 32.1% van die ontkiemde pitte asimptomaties besmet en is in staat om skadelike fumonisien-mikotoksiene te produseer. Sommige van hierdie grootmaatmonsters bevat fumonisienvlakke van 8 dpm (dubbel die wettige limiet), maar sou op grond van handmatige inspeksiemetodes veilig vir menslike verbruik verklaar word. Hierdie gebrek aan korrelasie tussen sigbare simptome en veiligheid beklemtoon die behoefte aan addisionele analitiese metodes om *Fusarium*-verwante risiko's te bepaal. Die voor-ontkiemende spektrale beelde van die onbesmette en asimptomaties besmette pitte is in twee klasse verdeel, en 'n PLS-DA-model het die mieliepitte met 'n klassifikasie-akkuraatheid van 67.0% geklassifiseer. Met inagneming van die hoë voedselveiligheidsrisiko verbonde aan fumonisiene, is NIR hiperspektrale beelding nie 'n uitvoerbare metode om asimptomatiese *Fusarium*-infeksies tydens die verwerking van Suid-Afrikaanse witmielies op te spoor nie.

Die resultate van hierdie studie het getoon dat NIR hiper- en multispektrale beelding belowende analitiese tegnieke vir outomatiese mielie gradering is, maar nie vir die opsporing van asimptomatiese *Fusarium*-infeksie nie. Die resultate van die *Fusarium*-ontkiemingsstudie het egter insig gegee in die status van *Fusarium*-infeksie en fumonisiene in die Suid-Afrikaanse mieliebedryf, wat nog nie in die literatuur verskyn het nie, en het die behoefte aan industrie-vriendelike mikotoksien-toetsmetodes beklemtoon.

Stellenbosch University https://scholar.sun.ac.za

TABLE OF CONTENTS

Stellenbosch University https://scholar.sun.ac.za

Stellenbosch University https://scholar.sun.ac.za

Stellenbosch University https://scholar.sun.ac.za

LIST OF FIGURES

Stellenbosch University https://scholar.sun.ac.za

LIST OF TABLES

Stellenbosch University https://scholar.sun.ac.za

Table S3 CovSel hierarchical model structure, consisting of 3 main levels, 15 sub-levels and 25 PLS-DA classification models. Each object enters the decision pathway at Level 1 and follows the relevant instructions according to classification result by the PLS-DA model.

Stellenbosch University https://scholar.sun.ac.za

LIST OF ABBREVIATIONS

3D three dimensional

ANN artificial neural networks

AOTF acousto-optic tunable filter

ARS adaptive reweighted sampling

BPNN back propagation neural network

CARS competitive adaptive reweighted sampling

CCD charged coupled device

CMOS complementary metal oxide semiconductor

CovSel covariance selection

COW correlation optimised warping

DON deoxynivalenol

EDF exponentially decreasing function

FAO United Nation's Food and Agricultural Organisation

FI firmness index

FMCIA first-derivative and mean centring iteration algorithm

GA genetic algorithm

GM genetically modified

HgCdTe mercury-cadmium-telluride

ICA independent component analysis

InGaAs indium-gallium-arsenide

IR infrared

KM Kubelka-Munk

LC-MS liquid chromatography with mass spectrometry

LCTF liquid crystal tunable filter

LED light emitting diode

LS-SVM least square support vector machines

Stellenbosch University https://scholar.sun.ac.za

LV latent variable

MAP modified atmosphere packaging

MC mean-centering

MC moisture content

MLR multiple linear regression

MNF minimum noise fraction

MOG matter other than grain

MSC multiplicative scatter correction

ND not detected

NIR near infrared

NIV nivalenol

PC principal component

PCA principal component analysis

PCR principal component regression

PLS partial least squares

PLS-DA partial least squares discriminant analysis

PPC psychrotrophic plate count

Q^2 cross-validated coefficient of determination

qRT-PCR quantitative real-time polymerase chain reaction

R^2 coefficient of determination

RBF radial basis function

RC regression coefficient

RGB red-green-blue

RMSECV root mean square error of cross validation

RMSEP root mean square error of prediction

ROI region of interest

SAGL South African Grain Laboratory

SAM spectral angle mapping

Stellenbosch University https://scholar.sun.ac.za

SANAS South African National Accreditation System

SEP standard error of prediction

SNV standard normal variate

SPA successive projections algorithm

SS sum of squares

SSC soluble solids content

SVM support vectors machine

SWIR short wave infrared UV ultra-violet

SWR stepwise regression

TAC total anthocyanin content

TVB-N total volatile basic nitrogen

TVC total viable count

UV ultraviolet

UVE uninformative variable elimination

VIP variable importance in projection

VIS visible

WHC water holding capacity

WM1 white maize grade 1

WM2 white maize grade 2

WM3 white maize grade 3

ZEA zearalenone

Stellenbosch University https://scholar.sun.ac.za

CHAPTER 1:
INTRODUCTION

Agriculture is one of the South Africa's most important economic sectors, and a national grand challenge of advancing the bio-economy has been set. The Department of Science and Technology have challenged South Africans to use biotechnology to improve human health, address food security and subsequently contribute to economic growth and improved quality of life. Maize (*Zea mays L.*) is South Africa's most important grain crop (Meyer et al., 2019). It is grown in diverse environments throughout the country and includes white maize, predominantly for human consumption, and yellow maize, for animal feed. Maize is consumed as an unfermented white maize meal by South Africans from a wide range of socio-economic backgrounds. As one of the country's largest crops and most important staple foods, scientific and technological advancement in maize and maize product production would have a substantial impact.

Hyperspectral imaging has been used extensively in cereal research in an array of applications (Sendin et al., 2018). The technology has been demonstrated as an alternative to conventional methods for the prediction of maize hardness (Manley et al. 2009; McGoverin and Manley 2012; Williams et al. 2009), variety (Wang et al. 2015b), moisture content (Cogdill et al., 2004), oil content (Weinstock et al., 2006) and fungal deterioration (Del Fiore et al. 2010; Williams et al. 2012; Vermeulen et al. 2017a). The technique is based on spatially resolved spectral data, where a spectrum is measured for each pixel in the image of a sample. The near infrared (NIR) region (1000 – 2500 nm) is often used in the study of food and agricultural products. Wavebands in this region excite organic molecules consisting mainly of C–H, C=O, O–H and N–H (Manley, 2014). Thus, NIR hyperspectral imaging can be used to evaluate samples based on differences in chemical components which contain these chemical groups (e.g. starch, sugars, proteins, fat and moisture). A key advantage of combining spatial and spectral information is the ability of offer single kernel assessments within a bulk scan. While single kernel conventional spectroscopic approaches are possible (Fox & Manley, 2014), bulk scans are more suited to industry implementation. Grain samples are heterogenous, where a single sample regularly contains both healthy kernels and small amounts of severely damaged kernels. When only a small portion of a large bulk sample is scanned, the resulting average measurement may not reflect the presence of unsafe materials. Spectral imaging takes a spectral measurement for every pixel within a sample and no part of the surface facing the camera is not scanned. Thus, the entirety of a heterogenous sample is measured. By spatially resolving the spectral information, one may compare the properties of one kernel with another, such as genetically modified (GM) and non-GM maize kernels (Feng et al., 2017) or observe the variation of properties between the anatomical components of a single kernel, such as water absorption patterns during wheat conditioning (Manley et al., 2011).

Hyperspectral imaging technology has been shown to be powerful and promising but is still largely underutilised in South African agro-product industries. The main barrier to entry is the high cost of the imaging system. In a developing country such as South Africa, labour is widely available at relatively low cost. Thus,

Stellenbosch University https://scholar.sun.ac.za

the industry tends to resist changing to automated solutions with high initial investment costs. In response, hyperspectral imaging research has increasingly focused on optimal waveband selection (Pu et al., 2015). Variable selection techniques are employed to identify a small number of wavebands required to accurately predict a specific property. The main advantage of minimising the number of wavebands is that a simplified application-specific instrument can be built for a much lower cost. Thus, the maize industry could use multispectral imaging to replace important conventional tests by developing a cheaper instrument for a single routine application. Recent studies aimed at offering industry-friendly alternatives to conventional methods for the inspection of cereal samples have increasingly investigated optimal waveband selection. While properties such as variety (Wang et al., 2015b), genetic modification (Feng et al., 2017), texture (Wang et al., 2015a) and adulterant presence (Su & Sun, 2016) have been successfully evaluated, many of the properties considered in South African maize grading legislation are yet to be investigated.

Maize grading is a labour-intensive step that is conducted throughout the maize market value chain. Visual inspection by a skilled grader is used to establish a grade (indication of maize condition and health) and assign a fair price as maize is traded between a farmer, silo owner, trader and miller. The South African maize industry utilises a very simple grading method. A sample (150 g minimum) of the maize consignment is visually inspected to identify any content other than sound white maize, such as defective or foreign materials. The contents of any identified undesirable materials are weighed and referenced to maximum levels stipulated for each material's category. The grade is allocated solely on the contents of undesirable materials within a sample. There are three white maize classes, WM1 (best), WM2 and WM3. The South African maize grading legislation (Government Gazette No. 32190 of May 8 2009, Regulation No. R.473) stipulates five main categories which a kernel/object can fall into, namely sound (healthy) white maize, defective white maize, pinked white maize, other colour (yellow) maize, and foreign materials. The legislation also identifies sub-categories for defective kernels and foreign materials. Defective kernels include broken maize kernels (screenings), fungal damage, heat damage, water damage, frost damage, pest damage (rodent and insect), sprouted kernels and immature kernels. Foreign materials include other common commodities, including soy, sorghum, sunflower seeds and wheat, as well as miscellaneous plant materials.

A human grader can visually distinguish all of the 17 abovementioned categories and sub-categories from one another, although this may become tedious and inconsistent as grading is continuously conducted. To automate this complicated process, an analytical technique must also be capable of separating all of the necessary categories simultaneously. Separating this large number of classes is rarely done in hyperspectral imaging studies. The multivariate classification modelling techniques commonly used in hyperspectral imaging studies, such as partial least squares discriminant analysis (PLS-DA), are most accurate when separating two or three classes. A 17-way PLS-DA model would not be capable of fully separating all closely-related classes within its high dimensional and noisy feature spaces, and the resulting accuracy would be very low (Myles & Brown, 2004). Instead of attempting to calibrate multi-class models to evaluate all classes, hierarchical modelling may be the best solution for problems such as grading. This approach breaks the process down into a series of classification steps, for instance a two-way PLS-DA model for each class under investigation. These

Stellenbosch University https://scholar.sun.ac.za

refined simple multivariate models are assembled into a single a multi-level decision tree, where the analysis in one step is guided by the result of the previous step. Each sample is presented to the decision tree and assigned the single most suitable predicted class.

A second process in maize and maize product evaluation that could be drastically improved is the identification of harmful fungal deterioration. The South African maize industry is widely affected by one pathogenic species in particular, *Fusarium*. Infection by *Fusarium* spp. not only results in reduced yield and poor quality, but also produces harmful secondary metabolites called mycotoxins within the kernel. The strain of most concern in South Africa is *Fusarium verticillioides.* The mycotoxins produced by *F. verticillioides* are fumonisins (fumonisin B_1, B_2 and B_3), and can cause oesophageal cancer in humans and severe illness in livestock (Norred & Voss, 1994).. Conventional testing for mycotoxins using liquid chromatography-mass spectrometry (LC-MS) is expensive, with commercial laboratories charging *ca.* ZAR 1 500 (USD 100) per sample. Conventional methods based on immunoassays, such as lateral flow devices and enzyme-linked immunosorbent assays (ELISA), may alternatively be used. Chromatographic and immunoassay techniques require sample preparation, such as sample milling and liquid extraction, and cannot be tested conveniently and quickly within a maize processing facility (Cross & Hornshaw, 2016). For decades, the industry has instead relied on visual inspection by maize graders to establish if there is an unacceptable amount of fungal damaged kernels in a maize consignment. A consignment with little to no fungal damaged kernels is declared safe for human consumption by the grader and is processed into an end-product. Legislative limits on fumonisins have been very recently introduced in 2016. As conventional analytical methods are complicated and expensive, this industry has resisted the implementation of testing.

It has been widely established that fumonisins can be produced before rotting occurs and visible symptoms become apparent (Stumpf et al., 2013). These infected but visually healthy kernels are referred to as asymptomatically infected and can contain dangerous levels of fumonisins. While a human grader inspects for differences between healthy kernels and infected kernels based on differences in the visible region (375 – 780 nm), a NIR hyperspectral imaging camera detects differences in a completely different region (900 – 2500 nm). Prior to developing visible surface damage, the fungal activity may cause internal depletion of chemical components by the fungus (e.g. protein, starch or moisture) to which NIR spectroscopy is sensitive. A NIR hyperspectral imaging instrument capable of detecting these differences between healthy and asymptomatically *Fusarium* infected kernels could be used as a screening tool for targeted mycotoxin analysis. If a consignment is found to be at risk of mycotoxin contamination (i.e. *Fusarium* infection is detected), additional mycotoxin testing is necessary before being declared fit for human consumption. As the industry has been resistant to the implementation of expensive fumonisin testing, maize producers and processors may be more likely to conduct testing with the knowledge that it is targeted and only conducted where necessary. Unfortunately, NIR spectroscopic techniques do not provide the sensitivity required for quantitative mycotoxin analysis (Bart et al., 2012), and are better suited as a screening method to indicate whether the further testing is required.

The aim of this dissertation was to present the South African maize industry with an accurate and affordable automated analytical technique for white maize grading and for identifying asymptomatic *Fusarium*

Stellenbosch University https://scholar.sun.ac.za

fungal contamination. This was achieved by using NIR hyperspectral imaging, chemometric classification model development, optimal waveband selection and hierarchical modelling. Specific objectives were:

1. grading of white maize by simultaneously evaluating all categories stipulated in South African maize grading legislation using NIR hyperspectral imaging and a hierarchical decision pathway;
2. identification of optimal wavebands for simplified but accurate grading of white maize;
3. grading of white maize using optimal waveband spectral imaging and a hierarchical decision pathway;
4. germinating visibly sound (healthy) maize kernels to identify asymptomatically *Fusarium* infected kernels; and
5. classify single asymptomatically *Fusarium* infected kernels using NIR hyperspectral imaging.

REFERENCES

Bart, J. C., Gucciardi, E. & Cavallaro, S. (2012). Quality assurance of biolubricants. In: *Biolubricants: science and technology*. Pp. 396-450. Cambridge, UK: Elsevier.

Cogdill, R. P., Hurburgh, C., Rippke, G. R., Bajic, S. J., Jones, R. W., McClelland, J. F., Jensen, T. C., and Liu, J. (2004). Single-kernel maize analysis by near-infrared hyperspectral imaging. *Transactions of the ASAE,* **47**, 311.

Cross, T. G. & Hornshaw, M. P. (2016). Can LC and LC-MS ever replace immunoassays? *Journal of Applied Bionalysis,* **2,** 108.

Del Fiore, A., Reverberi, M., Ricelli, A., Pinzari, F., Serranti, S., Fabbri, A., Bonifazi, G., and Fanelli, C. (2010). Early detection of toxigenic fungi on maize by hyperspectral imaging analysis. *International Journal of Food Microbiology,* **144**, 64-71.

Feng, X., Zhao, Y., Zhang, C., Cheng, P. & He, Y. (2017). Discrimination of transgenic maize kernel using NIR hyperspectral imaging and multivariate data analysis. *Sensors,* **17,** 1894.

Fox, G., & Manley, M. (2014). Applications of single kernel conventional and hyperspectral imaging near infrared spectroscopy in cereals. *Journal of the Science of Food and Agriculture,* **94**, 174-179.

Manley, M. (2014). Near-infrared spectroscopy and hyperspectral imaging: non-destructive analysis of biological materials. *Chemical Society Reviews,* **43**, 8200-8214.

Manley, M., Du Toit, G. & Geladi, P. (2011). Tracking diffusion of conditioning water in single wheat kernels of different hardnesses by near infrared hyperspectral imaging. *Analytica chimica acta,* **686,** 64-75.

Manley, M., Williams, P., Nilsson, D., & Geladi, P. (2009). Near infrared hyperspectral imaging for the evaluation of endosperm texture in whole yellow maize (Zea maize L.) kernels. *Journal of Agricultural and Food Chemistry,* **57**, 8761-8769.

McGoverin, C., & Manley, M. (2012). Classification of maize kernel hardness using near infrared hyperspectral imaging. *Journal of Near Infrared Spectroscopy,* **20**, 529.

Meyer, H., Skhosana, Z. D., Motlanthe, M., Louw, W. & Rohwer, E. (2019). Long Term Monitoring (2014–2018) of Multi-Mycotoxins in South African Commercial Maize and Wheat with a Locally Developed and Validated LC-MS/MS Method. *Toxins,* **11,** 271.

Stellenbosch University https://scholar.sun.ac.za

Myles, A. J. & Brown, S. D. (2004). Decision pathway modeling. *Journal of Chemometrics,* **18,** 286-293.

Norred, W. P. & Voss, K. A. (1994). Toxicity and role of fumonisins in animal diseases and human esophageal cancer. *Journal of Food Protection,* **57,** 522-527.

Pu, H., Kamruzzaman, M., & Sun, D.W. (2015a). Selection of feature wavelengths for developing multispectral imaging systems for quality, safety and authenticity of muscle foods-a review. *Trends in Food Science & Technology,* **45**, 86-104.

Sendin, K., Williams, P. J., & Manley, M. (2018). Near infrared hyperspectral imaging in quality and safety evaluation of cereals. *Critical Reviews in Food Science and Nutrition, 58*(4), 575-590.

Stumpf, R., Santos, J. d., Gomes, L. B., Silva, C., Tessmann, D. J., Ferreira, F., Machinski Junior, M. & Del Ponte, E. M. (2013). Fusarium species and fumonisins associated with maize kernels produced in Rio Grande do Sul State for the 2008/09 and 2009/10 growing seasons. *Brazilian Journal of Microbiology,* **44,** 89-95.

Su, W.-H. & Sun, D.-W. (2016). Facilitated wavelength selection and model development for rapid determination of the purity of organic spelt (Triticum spelta L.) flour using spectral imaging. *Talanta,* **155,** 347-357.

Vermeulen, P., Ebene, M., Orlando, B., Fernández Pierna, J., & Baeten, V. (2017). Online detection and quantification of particles of ergot bodies in cereal flour using near-infrared hyperspectral imaging. *Food Additives & Contaminants: Part A,* **34**, 1312-1319.

Wang, L., Pu, H., Sun, D.-W., Liu, D., Wang, Q. & Xiong, Z. (2015). Application of hyperspectral imaging for prediction of textural properties of maize seeds with different storage periods. *Food Analytical Methods*, **8**, 1535-1545.

Wang, L., Sun, D. W., Pu, H., & Zhu, Z. (2015). Application of Hyperspectral Imaging to Discriminate the Variety of Maize Seeds. *Food Analytical Methods,* **9**, 1-10.

Weinstock, B. A., Janni, J., Hagen, L., & Wright, S. (2006). Prediction of oil and oleic acid concentrations in individual corn (Zea mays L.) kernels using near-infrared reflectance hyperspectral imaging and multivariate analysis. *Applied spectroscopy,* **60**, 9-16.

Williams, P. J., Geladi, P., Britz, T. J., & Manley, M. (2012). Investigation of fungal development in maize kernels using NIR hyperspectral imaging and multivariate data analysis. *Journal of Cereal Science,* **55**, 272-278.

Williams, P. J., Geladi, P., Fox, G., & Manley, M. (2009). Maize kernel hardness classification by near infrared (NIR) hyperspectral imaging and multivariate data analysis. *Analytica Chimica Acta,* **653**, 121-130.

Stellenbosch University https://scholar.sun.ac.za

CHAPTER 2: REVIEW OF LITERATURE

Part I: Optimal waveband based spectral imaging in food product evaluation

ABSTRACT

As the food industry moves toward methods that are non-destructive, non-invasive, simple and on-line, hyperspectral imaging research has thrived. The chemical and physical information contained in a hyperspectral image can be used to classify or quantify properties that may be impossible to determine using manual or conventional methods. However, issues with cost and expeditiousness have left the technique underutilised in industry. An alternative to using a hyperspectral instrument, which utilises a full spectral range, is the development of an application-specific multispectral system for routine analysis by selecting a handful of optimal wavebands that correlate closely with the property under investigation. This review investigates the underlying principles of spectroscopy and spectral imaging, and introduces the waveband selection methods most commonly used in the evaluation of food and food products. The application of these methods spans research conducted on meat and meat products, fish and shellfish, cereals and legumes, fruit and vegetables, and tea, where the aim of most studies is preliminary investigation into waveband selection for systems that provide the food industry with reliable and accurate real-time monitoring at relatively low costs.

Stellenbosch University https://scholar.sun.ac.za

INTRODUCTION

Food and food products are characterised by varying chemical compositions and physical properties which provide an indication of quality, safety and nutritional status. To ensure the conformity and safety of products for consumers, quality control regimes are widely implemented in all phases of production and may be conducted using a variety of methods. Traditionally, manual handling has been used to evaluate external features including colour, shape, size, surface texture and external defects. However, these methods are highly laborious and time consuming, and studies have demonstrated the limited human capacity to reproduce a consistent estimation of quality (Lorente et al., 2012). Furthermore, properties invisible to the human eye cannot be evaluated using manual inspection. Internal quality and safety may be measured using traditional laboratory methods which often require reagent-costly chemical analyses and result in sample destruction (Pu, Kamuzzaman & Sun, 2015a).

In response to the challenges of both manual sorting and traditional analytical techniques, recent developments in food science research and the food industry have favoured methods which are non-destructive, require little sample preparation, and may be implemented on-line. In addition, there is always pressure on the development of these new techniques to match the high accuracy of established traditional analytical methods. Near infrared (NIR) spectroscopy has gained huge popularity in practical settings, as the technique meets these aforementioned requirements (Manley, 2014). The advent of NIR spectroscopy in the last few decades has given rise to the development of new spectroscopic techniques, including spectral imaging. Recent developments in spectral imaging research have explored strategies for optimal waveband selection. These approaches aim to remove redundant spectral information to improve the accuracy and simplicity of applications. Based on preliminary hyperspectral imaging research, they are often the starting point for the development of industry-friendly multispectral imaging systems. Research based on these waveband selection strategies have been successfully applied in most sectors of food science research, including the study of meat (Barbin, ElMasry, Sun, Allen & Morsy, 2013; Kamruzzaman, Makino & Oshita, 2016), fish (Cheng, Sun & Pu, 2016; He & Sun, 2015), cereals (Feng, Zhao, Zhang, Cheng & He, 2017; Su & Sun, 2016) and fresh produce (Li et al., 2018; Rahman, Faqeerzada & Cho, 2018).

This review addresses the importance of optimal wavelength selection for the evaluation of food and food products using spectral imaging. The benefits of using multispectral imaging for routine analysis are explained, and the multivariate data analysis techniques and optimal waveband selection strategies used in the field are introduced and discussed. Recent applications utilising these strategies are reviewed.

FUNDAMENTALS OF VIBRATIONAL SPECTROSCOPY

Spectroscopy analyses a sample by describing the energy transfer between light and matter (Pasquini, 2003). The ultraviolet (UV), visible (VIS), near-infrared (NIR) and infrared (IR) regions of the electromagnetic spectrum can be measured by spectral instruments. The UV and VIS regions are categorised as electronic spectroscopic techniques, and the NIR and IR regions as vibrational. Vibrational spectroscopy, specifically NIR spectroscopy, has gained huge popularity as a tool for determining the chemical and physical properties of food

Stellenbosch University https://scholar.sun.ac.za

products. The NIR region covers a small part of the electromagnetic spectrum between the visible and infrared regions from 780 to 2500 nm. Radiation in this range is sufficient to raise molecules to their lowest excited vibrational states, a fundamental vibrational transition, but does not provide enough energy for electron excitation (except for some rare earth compounds). The most prominent bands seen during NIR analyses are due to overtones of stretching vibrations and stretching-bending combinations involving major X–H bonds (Ozaki et al., 2006). All molecules containing these bonds will give rise to a measurable NIR spectrum, such as O–H bonds (e.g. moisture, carbohydrate and fat), C–H bonds (most organic compounds), N–H bonds (e.g. proteins and amino acids) and S–H bonds (e.g. proteins and amino acids). Consequently, NIR analysis is highly suited to the study of biomaterials such as food and food products.

Vibrational spectroscopy is based on the concept that the bonds between atoms within molecules vibrate with defined frequencies (Pasquini, 2003). When a molecule absorbs light that corresponds with the vibration's frequency, it becomes excited to a higher vibrational energy level (v). The energy gap from the ground state (v=0) to the first level, the fundamental state (v=1), may be measured as one quantum. If light carries a photon with the energy of one quantum, it is absorbed, and the molecule is excited from ground to fundamental state. If a photon possesses two quanta, the first overtone is excited (v=2), and so on to higher overtones. In addition to the ability of an overtone to be produced at multiples of the fundamental vibrational frequency, combination tones occur where two or more fundamental and/or overtone vibrations combine (through addition and subtraction of energies) to give a single band. Fundamental vibrations of molecules generally originate from absorption in the IR region, while spectra in the NIR region comprise of overtones and combination bands (Manley, 2014). Overtones and combination bands are much less likely to occur than the fundamentals, and thus absorption is usually 10 to 100 times lower for first overtones with subsequent overtones and combinations continuing to decrease in strength.

Electronic spectroscopy involving the UV and VIS regions (160 – 780 nm) is based on similar principles to vibrational spectroscopy, however the excitation by the higher energy UV-VIS radiation gives rise to transitions through electronic energy levels (Sathyanarayana, 2001). This occurs when electrons moved from an occupied orbital in the ground state to an appropriate orbital in a higher energy state. Information regarding the covalent bonds within the sample molecules is revealed, and can be used for the identification of inorganic and organic species, such as highly conjugated organic compounds or transition metal ions.

Spectroscopy utilises these interactions between electromagnetic radiation and the sample material to provide a detailed fingerprint of the sample. As the energy from the light must be equal to the energy difference between two energy levels, there is a selective response from the molecular system in the sample to the incident light. In the wavelength or spectral range utilised, frequencies corresponding to bonds present will be readily absorbed, others that do not correspond will not be absorbed, and some will be partially absorbed. Plotting this absorption versus wavelength produces the spectrum of a sample, which allows qualitative and quantitative assessment of chemical and physical features. However, extracting meaningful information from the spectra, especially in the widely used NIR region, is often not straightforward. As food products contain thousands of X–H bonds, an NIR spectrum contains a large number of bands from overtones and combination bands that

Stellenbosch University https://scholar.sun.ac.za

overlap heavily with one another. This is referred to as the multicollinearity problem, and results in a spectrum with smooth, broad bands (Manley, 2014). It is difficult to assign spectral features to specific chemical components in the sample, and visually interpreting the spectrum is not as simple as with other forms of spectroscopy. It is due to this complexity that NIR spectroscopy is currently the analytical technique in which chemometrics is most often applied. Chemometrics is the use of mathematical and statistical techniques to extract relevant information from analytical data by recognising patterns and associating these with the chemical and physical properties under investigation (Esbensen & Geladi, 1989). Chemometrics and NIR technology have evolved together, and as NIR spectroscopy achieves more robust identification and extends its applicability, new challenges arise that motivate the improvement of chemometric techniques.

INTEGRATION OF SPECTROSCOPY AND IMAGING

The food industry has widely applied both imaging and spectroscopic technologies for quality and safety evaluation (Gowen et al., 2007). Spectral imaging integrates the two technologies by combining their main features to acquire spatial and spectral information simultaneously. Conventional imaging technology is one of the mostly widely used alternatives to manual inspection and has become an integral part of the food industry's move towards automation (Sun, 2010). Imaging methods permit the quantification or classification of a sample's spatial and colour attributes. External characteristics are often important factors in consumers' perception of a food product, such as assessing quality and maturity. Thus, imaging technologies are widely used for monitoring the colour, shape, size, surface texture and external defects in food and agricultural products (Park & Liu, 2015). Imaging systems include computer vision by a camera utilising either monochromatic (single colour) or polychromatic (many colours) light. The camera is complemented with image processing and analysis, involving mathematics and computer programming for automated evaluation of products. These systems acquire either two- or three-dimensional spatial information and can often assess several objects per second, leading to very high on-line throughput (Elmasry & Sun, 2011). However, as imaging technologies only utilise visible wavelengths, an image of the external view is acquired that cannot be used to detect or assess the intrinsic physical and chemical properties of a sample. Furthermore, imaging systems may have difficulty performing complex classifications such as distinguishing similar colours or detecting invisible defects.

As discussed, spectroscopy offers superior detection results and is used extensively in the food industry to perform a wide range of qualitative and quantitative analyses. Diffusely reflected light is recorded as the spectral response, which contains information about absorbing chemical groups near the surface of a sample. These analyses are conducted on the basis that a correlation exists between the spectral response and a specific chemical or physical property of the food product. Spectroscopy is widely used in industry to replace current conventional analytical methods as it is non-invasive, non-destructive, rapid and easy to implement on-line (Sun, 2010). Furthermore, once spectral information has been gathered in a single scan, the resulting dataset has the potential to be used for evaluating multiple chemical or physical properties. A constraint of conventional spectroscopic methods is that the information is not spatially resolved. Certain applications require the spatial distribution of chemical or physical properties. Instead, only a small portion of the sample is scanned, and an

Stellenbosch University https://scholar.sun.ac.za

average spectrum or prediction value is acquired. However, the scan may not be representative of the entire sample or sample group, especially if it is heterogeneous. If a defect or contaminant is confined to a small area on the sample, the area may not be scanned at all and will remain undetected. Furthermore, if the aim of the analysis is to sort or separate defective food products, an average difference in spectral response may be observed but the individual defective objects will not be identified.

The respective merits and shortcomings of conventional imaging and spectroscopic techniques highlight the advantages of combining the two platforms into one analytical system. Acquiring spatial positional information of the spectra gives spectral imaging the capability to measure, inspect, sort, and grade food products with remarkable accuracy and efficiency (Sendin et al., 2018b). The applicability in the food industry is largely due to the fact that food and agricultural products exhibit large variations in properties and composition within an individual sample (e.g. bruised and unbruised areas of an apple) or in a sample group (e.g. ripe and unripe apples). Spatially resolved spectral information can be used, for example, to identify or separate individual samples in a sample group based on chemical or physical properties (e.g. bruised tissue), or map spatial distributions (e.g. distribution of moisture) throughout a sample or sample group. Spectral imaging systems provide the food industry with a real-time, non-destructive alternative to manual or conventional methods that delivers cost effective, consistent, rapid and accurate results.

FUNDAMENTALS OF SPECTRAL IMAGING

Principles of spectral imaging

Hyperspectral imaging is the simultaneous acquisition of spatial images in numerous spectrally congruent bands (Burger and Geladi, 2006). Multispectral imaging uses wavebands that are not necessarily congruent, but are instead irregularly spaced to coincide only with very specific regions of the sample's spectrum that contain the most relevant information. However, both techniques are based on the same principles. A spectral image is a stack of two-dimensional grayscale image planes, with one image plane for each waveband. Hundreds of these image planes will be acquired in hyperspectral imaging, while multispectral imaging only acquires a handful (*ca.* 2 – 20). The spectral image thus consists of three dimensions, two spatial dimensions, length (x) by width (y), and one spectral dimension (λ). This three-way data matrix is generally termed the hypercube, or alternatively spectral cube, data cube, or spectral volume (Manley, 2014).

The hypercube can be examined in various useful ways. First, one can extract individual image planes of the sample at a single waveband. For example, moisture distribution may be observed throughout a sample at a key waveband (e.g. 1450 nm), or image segmentation may be performed using the image plane of a waveband that maximises the difference between the sample and background. Second, one may use the spectrum of a single pixel to investigate the chemical composition of a specific point. This is due to the stacking of congruent image planes, which gives each pixel a light intensity reading for each waveband. Plotting the light intensity of each waveband in the spectral range generates a full spectrum or spectral signature. With appropriate reference materials and data analysis, these spectral signatures can be used to routinely classify, detect or differentiate the given materials in every pixel of a sample's hypercube.

Stellenbosch University https://scholar.sun.ac.za

Basic spectral system components and set-up

Typical spectral imaging systems consist of four main parts, namely an imaging unit, a light source, a sample stage, and a computer. The specific parts, configuration and image acquisition mode will be dictated by the desired application. One of the most important considerations is the spectral range, which is the wavelength region covered by the instrument (Elmasry & Sun, 2011). Spectral imaging systems may operate in the UV, visible, NIR or IR regions, with the visible and NIR regions being most popular in food analysis applications. In addition, the spectral and spatial resolution must be considered. The spectral resolution relates to the ability to distinguish two adjacent wavebands, while spatial resolution describes the minimum size of a distinguishable object in the image. Both resolution parameters will affect the quality of the acquired image dataset, but will also determine its size. One must consider that having high quality data is important for achieving accurate calibrations and results, but large datasets may not be suitable for applications requiring rapid analysis times.

The imaging unit, arguably the most important element, is made up of a zoom lens, a spectrograph and a camera. The function of a spectrograph is to disperse the light reflected from the sample through the lens into a continuous spectral range which will be recorded by the camera. Most spectrographs achieve this by including optical devices, each suited for different acquisition modes, such as a prism, diffraction grating, liquid crystal tunable filter (LCTF) or acousto-optic tunable filter (AOTF) (Pu, 2015). When operating in the visible and NIR range of 400 to 1000 nm, cameras will utilise a less expensive charge-coupled-device (CCD) or complementary metal oxide semiconductor (CMOS) silicon-based camera to collect both spectral and spatial information (Sendin et al., 2018b). If NIR wavelengths of 1100 nm to 2500 nm are required, a more costly indium gallium arsenide (InGaAs) or mercury cadmium telluride (HgCdTe) array detector is used. A light source is required to illuminate the sample in radiation of the desired region. The type of light source used will also be determined by the spectral range of the instrument. When operating in the visible and NIR regions, tungsten-halogen lamps are most commonly used (Sendin, 2018b). This is due to their durability, stability, and capability to emit light of a broad spectral range (400 – 2500 nm). Other possible light sources include quartz-halogen lamps, light emitting diodes (LEDs), tunable lasers, and heated xenon lamps. LED sources are, however, restricted to a narrow range of 400 to 900 nm.

Three instrumentation approaches are used to acquire spectral images. These approaches are known as staring scan, push-broom (line) scan, or whisk-broom (point) scan (Dale et al., 2013). Spectral image data is a three-dimensional hypercube, but there are currently no means of acquiring all three dimensions simultaneously. Instead, there are different combinations in which one or two of these dimensions are gathered either simultaneously or sequentially. The simplest approach is staring, where the image field of view is fixed, and an image plane is collected at one waveband after another. In other words, both spatial dimensions are acquired simultaneously, and the spectral dimension is acquired sequentially. Acquiring an image at different wavelengths using this configuration requires a spectrograph with a tunable filter, such as a LCTF or AOTF (Elmasry and Sun, 2011). As this process is inherently slow, it is only preferable when fewer wavebands are used, and is well-suited to multispectral imaging. In addition to the obvious issue of time restraints in industrial

Stellenbosch University https://scholar.sun.ac.za

uses, lengthy image acquisition times (often several minutes) may be a concern when working with certain food samples which may undergo changes due to heating by the continuous illumination from the light source. Lastly, the sample must remain in a fixed position during image acquisition, and thus this mode would not be suitable for production line implementation.

The second approach is whisk-broom or point scan, where the full spectrum of each point is acquired individually. All three dimensions are acquired separately as the sample is moved in a zigzag pattern on a grid of points covering the whole image. As the entire spectrum is gathered for an individual pixel at once, a tunable filter is not required, and instead an optical grating, prism or a similar dispersing element is utilised. This acquisition mode is popular for microscopic imaging where the acquisition time is usually not a problem. However, since a double scan (i.e. spatial and spectral) is required, this mode is also not suitable for implementation on a production line.

The third mode, and currently most popular in desktop spectral imaging, is push-broom or line scan. This method acquires the full spectrum of one line of pixels at a time. Thus, the spectral dimension and one spatial dimension are acquired simultaneously, while the second spatial dimension is acquired sequentially as the sample is moved in a straight line underneath the camera. As with whisk-broom instruments, a dispersing element is used in the spectrograph. However, as an entire line of pixels is recorded at once, a two-dimensional dispersing element and a two-dimensional detector array are required. This method does not require the changing of filters and the sample only moves in one direction (the direction of the second spatial dimension), and is thus well suited to implementation on a conveyor system at speeds around 5 to 10 seconds per metre (hyperspectral imaging).

Multispectral imaging vs. hyperspectral imaging

Capturing a full spectral measurement over a continuous wavelength range for every pixel in an image results in hyperspectral imaging datasets containing a wealth of information. This includes sample's chemical components, for example of moisture, carbohydrates, proteins and other hydrogen bonded constituents, as well as physical properties, such as size, shape and texture. Hyperspectral imaging is ideal for research purposes, as there is little constraint of time and computing power in a research laboratory and acquiring a large and complete hyperspectral dataset allows for more sophisticated analysis to be conducted. As a result, an abundance of hyperspectral imaging research in food science and beyond has demonstrated the ability of hyperspectral imaging to evaluate food product properties vital to the food industry (Cheng et al., 2017; Pu et al., 2015b; Sendin et al., 2018b). Despite demonstrating this huge potential for food industry implementation, it is not often implemented for routine analysis in the food industry. Two primary constraints discourage widespread use. First, hyperspectral systems are high in cost, and second, they generate extremely large amounts of data in a short time, resulting in high computational loads that hinder the development of efficient real-time applications.

Hyperspectral imaging units, plus the required computing power and data storage, are expensive. While the technique offers numerous benefits to the food industry, the initial cost associated with implementing a hyperspectral imaging system often seems to be a deterrent. Multispectral imaging is a cheaper alternative ($15

Stellenbosch University https://scholar.sun.ac.za

000 vs. $400 000), but the system must be tailor-made for the application by selecting the most appropriate wavelengths for the specific sample. Many of the studies discussed in this review were conducted as preliminary hyperspectral imaging research to develop reliable and accurate real-time monitoring systems for specific food quality or safety parameters based on a handful of the most suitable wavebands. By reducing the number of wavebands recorded, the system can be built using simpler, and thus less expensive, components.

While desktop computing and software have improved substantially since the advent of hyperspectral imaging, some production lines simply move samples too quickly for the image acquisition and analysis times currently offered by push-broom hyperspectral imaging instruments. These times are restricted as hyperspectral image datasets are huge and include large amounts of redundant information. Acquiring the dataset and extracting the important information to generate a result requires a relatively long time using today's computing power. Again, multispectral imaging developed through optimal waveband selection may be used to overcome this issue by reducing the amount of data to be captured and processed (2 seconds vs. 10 seconds per metre conveyor belt).

A third issue often overlooked in hyperspectral imaging research is multicollinearity. This is due to the large number of overtones and combination tones that occur in the contiguous wavebands, which begin to overlap and give rise to spectra with broad bands instead of sharp peaks. Due to this overlap, it is difficult to relate a waveband to the chemical constituent under investigation. It has been found that the high spectral resolution of NIR hyperspectral images does not necessarily lead to increased analytical precision, and prediction capability is often improved by reducing the dimensionality of the dataset (Elmasry et al., 2012). If a waveband does not carry useful spectral information, it will only add noise to a chemometric model. Despite the use of complex chemometric methods, hyperspectral models often contain some degree of repeated, redundant or irrelevant information. Instead, selecting optimal wavebands and removing the rest minimises collinearity issues.

The best way to overcome the shortcomings of hyperspectral imaging is to reduce the typical *ca.* 250 wavelengths recorded by the hyperspectral system to far fewer irregularly spaced wavebands (*ca.* 2–20). Multispectral systems are generally developed for a single specific inspection application, for example the current industrial use of 4 wavebands to separate Arabica and Robusta coffee beans (Calvini et al., 2017). The process of developing a multispectral system usually begins with optimal waveband selection derived from hyperspectral image data. Once the waveband selection is made, the multispectral system will be built. A staring instrument is the less expensive set-up option, utilising either a LCTF or AOTF. These staring systems could be used in a facility which does not require testing to take place on- or in-line. Alternatively, one can inexpensively assemble a simple multiband camera system using commercially available filters that best match the selected key wavebands that are sequentially changed in front of the camera, and will not be significantly different from conventional cameras in speed and cost (*ca.* $5 000 US) (Kamruzzaman et al., 2016). Applications requiring on- or in-line assessment will require a push-broom set-up to facilitate the movement of samples on a conveyor belt, which can cost more due to the need of a more complex spectrograph (*ca.* $15 000), but will cost significantly less than a typical hyperspectral push-broom system (*ca.* $400 000).

Stellenbosch University https://scholar.sun.ac.za

STRATEGIES FOR OPTIMAL WAVEBAND SELECTION

In typical hyperspectral imaging studies, a calibration model includes all acquired wavebands. A full spectrum contains a large amount of redundant information that can negatively influence the prediction ability of the model. To remove non-informative wavebands and calculate simpler and more accurate models, the wavebands and combinations thereof responsible for the properties under investigation must be identified. In addition, wavebands affected by other sources of variation must be excluded (Pu et al., 2015a).

Simple spectrum-based methods

The simplest methods involve visual inspection of the spectra to manually select wavelengths. These methods are based on selecting wavebands according to the maximum or minimum intensity difference (Pu et al., 2015a). This is often achieved through the comparison of band ratios (Liu, Sun & Zeng, 2014), and simple calculations can be applied to amplify differences, such as log ratios (Wang, Li, Tollner, Gitaitis & Rains, 2012) or spectrum derivatives. However, the selected wavebands might not be the most significant ones, and more sophisticated techniques may offer improved results.

Multivariate modelling techniques

One may choose to select optimal wavelengths based on statistics calculated in popular multivariate analysis techniques, such as principal component analysis (PCA) (Wang et al., 2012), partial least squares (PLS) (Cheng, Sun, Pu & Wei, 2018), multiple linear regression (MLR), back propagation neural networks (BPNN) or artificial neural networks (ANN).

Two of the most popular chemometric methods are PCA (Cowe & McNicol, 1985; Esbensen & Geladi, 1989) and PLS (Wold, 1982), which are based on the calculation of orthogonal components that explain the variation in the set of independent variables (pixels or objects), X. These components are referred to as principal components (PC) in PCA and latent variables (LV) in PLS. The calculation of PCs and LVs entail decomposing the dataset into matrices of scores and loadings. Studies may select wavebands based on the loadings value of a waveband, or, often in the case of PLS, the waveband's weighting. This weighting is calculated to indicate the importance of a waveband in achieving separation within a PC or LV, and is used to calculate loadings value. The most sophisticated approach to this method is the use of variable importance in projection (VIP) scores. The calculation of VIP scores considers the weighting of a waveband and the amount of explained y-variance within each LV. A waveband with a VIP score greater than 1 is considered important, while a waveband with a VIP score less than 1 is probably a good candidate for removal.

Optimisation algorithms

Novel multivariate approaches incorporating specially developed optimisation algorithms have also been explored. These include successive projections algorithm (SPA) (Dong & Guo, 2015; Ma, Pu & Sun, 2018), covariance selection (CovSel), competitive adaptive reweighted sampling (CARS) (Feng et al., 2017;

Stellenbosch University https://scholar.sun.ac.za

Kamruzzaman et al., 2016), genetic algorithm (GA) (Feng & Sun, 2013b; Li et al., 2018), stepwise regression (SWR) (Feng & Sun, 2013a), first-derivative and mean centring iteration algorithm (FMCIA) (Su & Sun, 2016) and variable importance in projection (VIP) algorithm (Rahman et al., 2018). These algorithms generally work by conducting numerous iterations, identifying test sets of wavebands, and calculating and comparing chemometric models based on this set. The regression method most commonly used in literature appears to be PLS regression, as this is a relatively simple linear technique and easy to interpret. While MLR would be even simpler and is easily implemented in industrial settings, it cannot be performed when the number of samples is fewer than the number of the input variables (wavebands), as can often be the case in hyperspectral imaging datasets (Xie, Li, Shao & He, 2014). Thus, MLR models are often only established once an optimal waveband selection has been made (Cheng et al., 2016; Li et al., 2018; Qiu, Zhu, Fan, Yao & Lewis, 2018; Su & Sun, 2016; Wu et al., 2012a; Wu, Sun & He, 2012b; Wu & Sun, 2013b; Xie et al., 2014).

Successive projections algorithm

Successive projections algorithm (SPA) is a forward selection method specifically designed to remove collinearity between spectral variables by means of successive projections on interlinked sub-spaces (Caneca et al., 2006; Roger et al., 2011). SPA calculations utilise the matrix of the calibration samples and their spectral response for each waveband. Starting from the initial variable waveband (**x**0), SPA determines which of the remaining wavebands has the largest projection on the subspace orthogonal to **x**0. This waveband (**x**1) is the variable that contains the most information that has not already been explained by **x**0. In the next iteration, SPA takes **x**1 as the new reference waveband and repeats the same steps until a predetermined optional number of wavebands (*N*) is chosen. The process is repeated until each waveband is used as the initial variable waveband (**x**0), and thus one subset of optimal wavebands is generated for each of the wavebands in the dataset. A chemometric model (e.g. MLR or PLS regression) is calculated based on each of these optimal subsets. The root mean square error of cross validation (RMSECV) of each model is compared to find the model with lowest error, thus determining the best performing optimal waveband subset. By selecting the wavebands which explain the most information not already explained by the previous waveband, SPA favours the minimisation of collinearity between the wavebands.

Covariance Selection

Inspired by SPA, covariance selection (CovSel) was developed to work in a similar way, but to also account for the covariance between the X- and **Y**-data. SPA aims to minimise collinearity in the dataset. However, as SPA is based only on the X-data, the resulting selections are based solely on the spectral data and not the class information (**Y**-data) (Vigneau & Thomas, 2012). In the case of closely-related classes, the class information should be considered to identify wavebands highlighting the differences between two classes. As CovSel accounts for the covariance between the X- and **Y**-data, the difference between the two techniques is comparable with the differences between PCA and PLS. In each iteration, the waveband presenting the highest covariance is identified and all the other wavebands and the y-responses are orthogonalized to it (Biancolillo et al., 2019).

Stellenbosch University https://scholar.sun.ac.za

Competitive adaptive reweighted sampling

Competitive adaptive reweighted sampling (CARS) aims to eliminate wavebands with low weighting in the chemometric model (Qiu et al., 2018). As in SPA, the final selection is based on the combination of wavebands which produces the lowest RMSECV. Selection takes place in four successive steps, including Monte Carlo model sampling, enforced reduction by exponentially decreasing function (EDF), competitive reduction by adaptive reweighted sampling (ARS), and RMSECV calculation for each subset (Li, Liang, Xu & Cao 2009). Monte Carlo is a sampling method used to learn about a system by simulating it with random sampling. The approach is powerful, flexible and very direct, and is used to ensure high adaptability regardless of variation in training samples. A group of samples is randomly selected using a fixed ratio (usually 80–90% of the calibration set). Using the subset of samples, a model (e.g. MLR or PLS regression) is calculated and a two-step procedure is applied for optimal waveband selection. The first step is EDF based enforced wavelength selection. This step removes wavebands containing little to no relevant information, based on low weighting in the chemometric model (e.g. low regression coefficient in MLR). The wavebands retained in each iteration is calculated based on an exponential equation, where most wavebands are eliminated very quickly in the first sampling runs (*ca.* 90% of the removals occur in the initial 30 iterations). This forced selection then tapers off and the selection is refined by gently removing wavebands (*ca.* 10% in the last 70 iterations). ARS follows to further eliminate wavebands in a competitive way, and is based on Darwin's 'survival of the fittest' principle. The wavelengths with high weighting become dominant during sampling and are selected with higher frequency, while low weighting wavebands are much less competitive and are phased out over the series of iterations. Cross-validation of the model is continually applied to identify the subset with the lowest RMSECV.

Genetic Algorithm

Genetic algorithm (GA) is a flexible and widely utilised guided random search technique, based on the principle of natural selection mechanisms (Araujo et al., 2001). This approach explores possible optimal waveband sets in an efficient manner, where the initial 'population' of wavelengths is evolved to a new population based on the concept of genetic operators like reproduction, crossover and mutation (Khurana, Rathi & Akshatha, 2011). GA operates in an iterative manner, evolving the successive populations until a termination criterion is reached (e.g. lack of improvement, maximum number of generations or maximum time) (Cheng et al., 2016). The iterations involve the use of a modelling technique, often PLS regression, whereby the wavebands are added to and removed from the model during successive iterations (Cheng et al., 2017; Leardi, 2000). Due to the stochastic nature of the technique, results from a single run of GA may not be reproducible. Consequently, many studies repeatedly execute GA runs to select several sets of candidate wavebands (Feng & Sun, 2013b). One may assume that the wavebands which continually appear in GA runs are likely important variables, and are often ultimately selected as the optimal waveband set.

Stellenbosch University https://scholar.sun.ac.za

Stepwise regression

Stepwise regression (SWR) is a useful technique when handling datasets with a large number of spectral variables (Liu et al., 2014). A simple MLR model is calculated with the aim of establishing an optimal regression equation containing only the wavebands with significant effects on the prediction ability (Qiu et al., 2018). Iterations are performed in which one variable is considered for addition or removal from the set based on the result of an F-test or t-test to determine significance. The process can be approached in three ways to optimise the wavelength selection. Forward selection (forward addition) can be used where variables are added to an initially empty model only if they are found to be significant. Backward selection (backward elimination) begins with all variables in the model and these are removed if found to not be significant. The third approach is bidirectional selection, which is a combination of both.

APPLICATIONS

The applications of optimal waveband based spectral imaging in food product evaluation are numerous and may be broadly divided as applications in meat and meat products, fish and shellfish, cereals and legumes, fruits and vegetables, and tea. Information on all reviewed studies is given in Table 1, including the spectral range, modelling and waveband selection technique, the number of optimal wavebands, the resulting accuracy or error, and change in error in comparison to the full waveband range.

Meat and meat products

Meat is widely considered the most valuable food product in terms of high nutritional and economic value (Pu et al., 2015a). In the hypercompetitive modern meat industry, the main issue is high perishability, which results in deterioration of both quality and safety.

Pork is one of the most widely consumed meats worldwide (Cheng et al., 2018), with studies conducted on fresh, frozen and processed pork meat products. Barbin et al. (2013) utilised NIR hyperspectral imaging to non-destructively determine the total viable count (TVC) and psychrotrophic plate count (PPC) in chilled pork during storage. Samples were stored at 0 and 4 °C for 21 days, and both hyperspectral image acquisition (910 – 1700 nm; 237 wavebands) and conventional microbiological testing were conducted every 48 h to calibrate a PLS regression model for predicting TVC and PPC. The resulting regression coefficients (RCs) were used to select 11 optimal wavebands for TVC prediction and 10 for PPC prediction. The authors related the wavebands of 970 nm (O-H stretching overtone), and 1151 nm and 1211 nm (C-H stretching overtone) to the changes in water absorption due to microbial activity. The standard error of prediction (SEP) of the TVC model was 0.70 log CFU using all wavebands, 1.0 log CFU using optimal wavebands and 1.2 log CFU using an red green blue (RGB) camera, while the SEP values for PPC were 0.83, 1.5 and 1.8 log CFU, respectively. The results demonstrated that

Stellenbosch University https://scholar.sun.ac.za

Table 1 List of applications of optimal waveband based spectral imaging in food product evaluation

Sample	Parameter	Waveband range (nm) / number	Selection method	Modelling method	Wavebands	RMSEP (% change*)	Classification accuracy	Reference
Pork	TVC	910 – 1700 / 237	RCs	PLSR	11	1.0 log CFU** (↑43%)	-	Barbin et al. (2013)
Pork	PPC	910 – 1700 / 237	RCs	PLSR	10	1.5 log CFU** (↑81%)	-	Barbin et al. (2013)
Pork	Grade	910 – 1700 / 237	2nd derivative	PCA	6	-	96%	Barbin et al. (2012)
Pork	Fat content	400 – 1000 / 381	SPA	SVM	8	0.89 g/kg (↓13%)	-	Ma et al. (2018)
Pork	Freeze damage	1000 – 2200 / 189	SPA	PLSR	6	1.49 & 0.015 (↑20 & 7%)	-	Cheng et al. (2018)
Pork	Chemical spoilage	400 – 1000 / 381	GA	ANN	8	2.4 g/kg (↓14%)	-	Cheng et al. (2017)
Mutton	Chemical spoilage	400 – 1000 / 848	CARS-SWR	SVM	12	3.3 g/kg (↓10%)	-	Qiu et al. (2018)
Lamb	Tenderness	910 – 1700 / 237	SPA	PLSR	6	5.8 N (↑2%)	89%	Kamruzzaman et al. (2013)
Red meat	Species of origin	910 – 1700 / 237	2nd derivative	PLS-DA	6	-	93 & 99%	Kamruzzaman et al. (2012)
Red meat	WHC	400 – 1000 / 121	CARS	LS-SVM	8	0.56 % (↑12%)	-	Kamruzzaman et al. (2016)
Chicken	TVC	910 – 1700 / 237	SWR	PLSR	7	0.50 log CFU (↓12%)	-	Feng & Sun (2013a)
Chicken	*Enterobacteriaceae*	930 – 1450 / 156	RCs	PLSR	3	0.45 log CFU (↓4%)	-	Feng et al. (2013)
Chicken	*Pseudomonas*	910 – 1700 / 237	GA	PLSR	14	0.64 log CFU (↓20%)	-	Feng & Sun (2013b)
Chicken	Contaminants	400 – 800 / 567	SPA	MLR	12	-	100%	Wu et al. (2017)
Chicken	Grade	400 – 1000 / 381	SPA + texture	RBF-SVM	9 + features	-	93%	Xiong et al. (2015)
Fish	Freeze damage	400 – 1000 / 381	GA-SPA	MLR	5	1.1%	-	Cheng et al. (2016)
Fish	TVC	400 – 1000 / 381	SPA	LS-SVM	7	0.53 log CFU (↑6%)	-	Cheng & Sun (2015)
Prawns	Drying (MC)	416 – 1030 / 482	SPA	LS-SVM	12	1.5% (↑9%)	-	Wu et al. (2012a)
Salmon	WHC	400 – 1000 / 121	CARS	PLSR	9–13	0.3–1.1% (↓ 9–15%)	-	Wu & Sun (2013a)
Salmon	Colour (L*a* b*)	964 – 1631 / 200	SPA	PLSR	7	1.4–2.4 (0%)	-	Wu et al. (2012b)
Salmon	Packaging methods	400 – 1100 / 64	RCs	KNN	5	-	88%	Sone et al. (2012)
Salmon	TVC	400 – 1000 / 121	CARS	LS-SVM	8	0.27 log CFU (↓7%)	-	Wu & Sun (2013b)
Salmon	LAB	900 – 1700 / 239	CARS	LS-SVM	8	0.53 log CFU (↑2%)	-	He et al. (2014)
Salmon	*Enterobacteriaceae*	900 – 1700 / 239	SPA	PLSR	8	0.47 log CFU (↓11%)	-	He & Sun (2015)
Maize	Foreign material	400 – 950 / 57	GA	PLS-DA	5	0.26	-	Wallays et al. (2009)
Maize	Variety	400 – 1000 / 380	SPA + texture	LS-SVM	6 + features	-	89%	Wang et al. (2016)
Maize	GMO detection	874 – 1734 / 200	CARS	PLS-DA	54	-	99%	Feng et al. (2017)

Stellenbosch University https://scholar.sun.ac.za

Maize	Texture	400 – 1000 / 380	SPA	PLSR	7	0.2 N (↑75%)	-	Wang et al. (2015b)
Rice	Variety	400 – 1000 / 380	RCs + texture	BPNN	7 + features	-	94%	Wang et al. (2015a)
Spelt	Authentication	957 – 1625 / 200	FMCIA	PLSR	8	0.04–0.06% (↑105–115%)	-	Su & Sun (2016)
Black beans	Variety	501 – 1000 / 386	SPA + texture	PLS-DA	11 + features	-	98%	Sun et al. (2016)
Apples	SSC	928 – 1661 / 222	SPA	LS-SVM	17	0.54 °Brix (↓2%)	-	Dong & Gao (2015)
Apples	MC	928 – 1661 / 222	SPA	LS-SVM	23	0.45% (↓12%)	-	Dong & Gao (2015)
Apples	pH	928 – 1661 / 222	SPA	LS-SVM	8	0.057 (↓8%)	-	Dong & Gao (2015)
Apples	Firmness	928 – 1661 / 222	SPA	LS-SVM	11	0.31 kg/cm^2 (↓12%)	-	Dong & Gao (2015)
Apples	*Penicillium*	400 – 1000 / 750	SPA	PLS-DA	4	-	98%	Zhang et al. (2015a)
Apples	*Penicillium*	400 – 1000 / 750	PCA	ICA	2	-	97%	Zhang et al. (2015a)
Pears	SSC	400 – 1000 / 774	CARS-SPA	PLSR	25	0.48 °Brix (↓6%)	-	Fan et al. (2015)
Pears	SSC	400 – 1000 / 998	SPA	PLSR	51	0.032 °Brix (↓78%)	-	Li et al. (2016)
Pears	Firmness	400 – 1000 / 774	CARS-SPA	PLSR	22	0.72 N (↓3%)	-	Fan et al. (2015)
Pears	Firmness	400 – 1000 / 998	SPA	PLSR	58	0.063 N (↓74%)	-	Li et al. (2016)
Pears	Edible wax types	400 – 1026 / ?	SPA	LDA	11	-	96%	Li et al. (2017)
Cherries	SSC	972 – 1649 / 200	GA	MLR	54	1.2 °Brix (↓9%)	96%	Li et al. (2018)
Cherries	pH	972 – 1649 / 200	GA	MLR	24	0.057 (↓5%)	96%	Li et al. (2018)
Litchi	Anthocyanin content	350 – 1050 / 431	SPA + SWR	RBF-NN	9 + 11	0.61% (↑20%)	-	Yang et al. (2015)
Strawberries	Damaged	380 – 1010 / 440	SPA	SVM	8	-	93%	Liu et al. (2018)
Garlic	SSC	1000 – 1700 / 275	SPA	LS-SVM	10	1.0%** (↓9%)	-	Rahman et al. (2018)
Garlic	Allicin content	1000 – 1700 / 275	VIP	LS-SVM	18	0.19 mg/g* (↑19%)	-	Rahman et al. (2018)
Onions	*Burkholderia cerpacia*	950 – 1650 / 350	PCA	LDA	2	-	80%	Wang et al. (2012)
Tea	Colour (L*)	400 – 1030 / 496	CARS	MLR	48	1.16 (↓4%)	-	Xie et al. (2014)
Tea	Colour (a*)	400 – 1030 / 496	SPA	LS-SVM	6	1.15 (↓11%)	-	Xie et al. (2014)
Tea	Colour (b*)	400 – 1030 / 496	CARS	LS-SVM	26	1.76 (↓11%)	-	Xie et al. (2014)

* Percentage change of RMSEP from full spectra to optimal waveband set (↑ = increased error; ↓ = decreased error)

** Standard error of prediction (SEP)

Note: In applications where various data analysis approaches were utilised, only best resulting method has been given

Stellenbosch University https://scholar.sun.ac.za

optimised multispectral imaging in the NIR region may be superior to regular RGB computer vision. The same researchers also studied quality parameters of pork for grading and classification (Barbin et al., 2012). One class associated with high quality, 'red firm non-exudative' (RFN), and two low classes associated with undesirable quality, 'dark firm dry' (DFD) and 'pale soft exudative' (PSE), were selected. The classes were characterised using PCA based on 6 optimal wavebands selected using 2nd derivative spectra. These wavebands included 960 nm (water related O-H stretching overtone), 1074 nm (protein related N-H stretching overtone), 1124 nm (not discussed), 1147 nm (not discussed), 1207 nm (fat related stretching overtone of C-H), and 1341 nm (C-H combination band). A classification accuracy of 96% was achieved. Considering the simple data analysis approach used, this result shows promise for pork meat grading using NIR multispectral imaging.

Fat content in pork muscles has been predicted (Ma et al., 2018). The performances of traditional pre-processing techniques (Savitzky-Golay, standard normal variate (SNV) and multiplicative scatter correction (MSC) transformations) and novel techniques (first derivatives and correlation optimised warping (COW)) were compared in both support vector machines (SVM) and PLS regression models. From the full range (400 – 1000 nm; 381 wavebands), SPA was used to select 8 optimal wavebands. Notably, 435 and 438 nm are known to be related to fat content (Velásquez, Cruz-Tirado, Siche & Quevedo, 2017). From the numerous models calculated, the study found improvement after spectral pre-treatment by first derivative, COW or the combination of both. SVM with the combined pre-treatment performed best, resulting in root mean square errors of prediction (RMSEP) of 1.02 and 0.89 g/kg for the full (all wavebands) and SPA models, respectively, compared to PLS regression with 1.55 g/kg and 2.04 g/kg, respectively. The results demonstrated that removing 98% of the wavebands resulted in a 13% decrease in error.

Cheng et al. (2018) studied the effects of freezing on pork microstructure, specifically the changes in the myofibrillar proteins, where protein-water interactions are replaced with protein-protein interactions upon freezing, thus altering functional properties of the meat. Freezing rate affects the extent of these changes and thus the quality of the meat, but cannot currently be tested for in the frozen state. Hyperspectral images (1000 – 2200 nm; 189 wavebands) were acquired of frozen samples after undergoing freezing at various rates. Two markers for myofibrillar deformation, surface hydrophobicity and Ca^{2+}-ATPase activity, were measured using approved spectrophotometric reference methods to calibrate a PLS regression model. Two methods for optimising the model were compared, namely spectral angle mapping (SAM) algorithm and SPA. As the spectral angle obtained from the full waveband range can be less sensitive, the full spectrum was divided into 7 sections, and thus 7 spectral angles were calculated. Using SPA, 6 optimal wavebands were identified. The performance of the PLS regression models based on these two methods was extremely similar, with SPA achieving an RMSEP of 1.49 and 0.015 for the surface hydrophobicity and Ca^{2+}-ATPase markers, respectively, and 1.55 and 0.015 for SAM. In a previous study (Cheng, Sun, Pu & Wei, 2017), chemical spoilage in processed pork products was evaluated by quantitative artificial neural network (ANN) models using a full Vis-NIR range (400 – 1000 nm; 381 wavebands), a SPA based model (9 wavebands) and GA-PLS based model (8 wavebands). During spoilage, volatile organic compounds accumulate which may be measured as the total volatile basic nitrogen (TVB-N). The measurement of TVB-N in two categories of processed meats, namely salted and

Stellenbosch University https://scholar.sun.ac.za

cooked, was considered in this study. For industry applicability, it was decided to investigate a single model/multispectral system for both. An RMSEP of 2.84 mg/100 g was obtained for the full ANN model, 2.70 mg/100g for the SPA-ANN model, and 2.43 mg/100 g for the GA-PLS-ANN model, indicating that a model based on only 2% of the wavebands may lead to a 14% decrease in error.

Chemical spoilage in mutton was studied to compare the performance of several variable selection techniques, namely GA, CARS, RC, SPA and SWR (Qiu et al., 2018). GA and CARS were utilised in a primary step, as these methods reduce dimensionality efficiently, but the number of selected wavebands is often still too large. RCs, SPA and SWR were used in a secondary step to make a final selection. The primary step was performed using PLS regression as the modelling technique, and the full 848 wavebands was reduced to 215 by GA and 81 by CARS. By comparing the R^2 and RMSE values of the full, GA and CARS models, the CARS model performed best, despite using fewer variables, and was selected for further optimisation. RCs, SPA and SWR were each applied to multiple linear regression (MLR) based on the 81 wavebands selected by the primary CARS step, which further reduced the number of variables to 12, 14 and 12, respectively. The wavebands selected by SWR were correlated to previous literature, and the authors highlighted that the wavebands 527, 571, 605, 637, and 649 nm were related to deoxymyoglobin, oxymyoglobin, sulfmyoglobin, and metmyoglobin (Liu & Chen, 2001). Wavebands 753 and 969 nm were associated to water (O-H overtones), and 770 nm was relevant to C-H and N-H vibration overtones. Based on R^2 and RMSE values, CARS-SWR was chosen as the best combination. The 12 optimal wavebands were used to develop a non-linear SVM model, improving on the MLR results. An R^2 of prediction of 0.85 and RMSEP of 3.33 g/kg was ultimately achieved for predicting total volatile basic nitrogen (TVB-N) using CARS-SWR-SVM, in comparison with 0.81 and 3.68 g/kg, respectively, for the original full PLS regression model. Thus, error was reduced by 10% by using only 1.4% of the original spectral variables.

A study to authenticate species of origin was conducted, where intact muscles and minced meat from pork, beef and lamb were separated (Kamruzzaman, Barbin, ElMasry, Sun & Allen, 2012). Second derivative analysis was performed on NIR hyperspectral images (910 – 1700 nm; 237 wavebands) and 6 wavebands were selected to develop a PLS-DA model, namely 957, 1071, 1121, 1144, 1368 and 1394 nm. The chemical groups related to these specific wavebands was not discussed, but are almost identical to the 6 wavebands identified in the pork classification study discussed earlier (Barbin et al., 2012). The classification accuracy for an independent validation set of intact muscles and minced meat were 93 and 99%, respectively. The prediction of lamb tenderness was next investigated, using SPA as the wavelength selection technique (Kamruzzaman, Barbin, ElMasry, Sun & Allen, 2013). Both instrumental and sensory tenderness were considered, while comparing the use of the same imaging system's full range and 11 optimal wavebands selected using SPA. Wavebands associated with important chemical components included 934, 1144 and 1215 nm, related to C–H bonds in fat, and 964 and 1455 nm due to O–H bonds in water. For instrumental tenderness, the full PLS regression model gave an RMSECV of 5.71 N, which was comparable to the RMSECV of 5.84 N for SPA-PLS regression. Both models were used to sort samples into categories of 'tender' or 'tough', where the full model outperformed the optimised model with overall classification accuracies of 95 and 89%, respectively. Most

Stellenbosch University https://scholar.sun.ac.za

recently, the water holding capacity (WHC) of pork, beef and lamb was investigated (Kamruzzaman et al., 2016). WHC is an important quality property which has an influence on the appearance before cooking, as well as the sensory properties of the cooked product. As the envisioned multispectral system would be used for classifying all 3 species, waveband selection would be optimised across all classes. Two modelling techniques were explored, including one linear technique, PLS regression, and one non-linear technique, least square support vector machines (LS-SVM). In addition, full models (400 – 1000 nm; 121 wavebands), RC optimised models (8 wavebands) and CARS optimised models (8 wavebands) were compared. The authors did not elaborate on the chemical groups associated with the chosen wavebands. LS-SVM performed best with RMSEPs of 0.50, 0.56 and 0.63% for the full, RC and CARS models, respectively, compared to PLS regression with 0.63, 0.74 and 0.72%, respectively. The authors conclude by suggesting the use of band pass filters for the recommended wavebands (545, 610, 705, 765, 805, 900, 940 and 970 nm) within a multispectral camera to provide routine WHC prediction in red meat with a similar cost and speed of a regular RGB camera.

Several studies have been conducted on the detection and quantification of microbial loads on chicken fillets. Total viable count (TVC) has been predicted in chicken samples using full PLS regression models, as well as SWR-PLS regression (Feng & Sun, 2013a). Samples were stored at 4 °C for 9 days, and both hyperspectral image acquisition (910 – 1700 nm; 237 wavebands) and conventional microbiological testing were conducted every 24 h for the first 7 days and every 12 h for the remaining days. Three full models were calculated using different spectral profiles, namely reflectance (R), absorbance (A) and Kubelka-Munk (KM) function. KM function is a relatively simple mathematical transformation of the reflectance values (R) that accounts for scattering effects as given in Eq. 2.1:

$$KM = \frac{(1-R)^2}{2R} \tag{2.1}$$

The full A-PLS regression model performed best, with a cross-validated R^2 of 0.86 and RMSECV of 0.57 log CFU. Next, SWR was employed to select 5 wavebands based on the original reflectance data, 11 based on absorbance, and 7 based on KM parameters. The KM-SWR-PLS regression model performed best with a cross-validated R^2 of 0.88 and RMSECV of 0.50 log CFU, indicating that the robustness of the model was maintained while removing 97% of the wavebands from the dataset. Similarly, *Enterobacteriaceae* was detected on chicken samples (Feng et al., 2013). Samples were stored at 4 °C for 9 days, with hyperspectral image acquisition and conventional microbiological testing conducted every 24 h. Full PLS regression (930 – 1450 nm; 156 wavebands) resulted in a prediction R^2 of 0.85 and RMSEP of 0.47 log CFU. Two waveband selection methods were explored, firstly 2nd derivatives, where 4 wavebands were identified (948, 960, 1134 and 1144 nm) resulting in an R^2 of 0.87 and RMSEP of 0.54 log CFU; and secondly RCs, with 3 wavebands (930, 1121 and 1345 nm) resulting in 0.87 and 0.45 log CFU, respectively. A third optimised model was calculated using the wavebands identified by both methods (i.e. all 7 wavebands) but the results of 0.87 R^2 and 0.45 log CFU RMSEP showed no improvement from the RC-PLS regression result, and it was demonstrated that only 3 wavebands were required to achieve the best results in this application. *Pseudomonas* on chicken fillets was investigated using GA for optimal waveband selection (Feng & Sun, 2013b). GA is a random search technique, thus the

Stellenbosch University https://scholar.sun.ac.za

authors conducted 5 initial runs. As a window of 3 wavebands was used as one of the algorithm parameters, the variables identified in GA were a range of 3 wavebands, not a single waveband. Waveband ranges appearing in 3 of the 5 runs (GA-PLS-3), 4 of the 5 runs (GA-PLS-4) and all 5 (GA-PLS-5) were used as optimal waveband sets, as well as all the waveband ranges included in the first 3 models (GA-PLS-Any), and a last set which was chosen in undetailed 'trials' (GA-PLS-BT). Various pre-processing techniques and combinations were explored for the best calibration of a full PLS regression model and SNV only was best with a prediction R^2 of 0.65 and RMSEP of 0.80 log CFU. Of the optimal waveband range sets, GA-PLS-4 (14 waveband ranges) performed best with a R^2 of 0.77 and RMSEP of 0.64 log CFU. Prediction maps were successfully generated using the best full and GA-PLS regression models, showing promise for real-time prediction of microbes directly on meat using multispectral imaging.

Recently, Wu et al. (2017) detected four classes of contaminants on chicken carcasses, namely blood and three types of faeces. A sample group of 20 carcasses were artificially contaminated on a total of 120 regions and hyperspectral images were acquired (400 – 800 nm; 567 bands). SPA was applied to select 12 optimal wavebands, namely 505, 537, 561, 562, 564, 575, 604, 627, 656, 665, 670 and 689 nm. MLR, PLS regression and SVM models were developed. The MLR-SPA approach performed best, detecting all contaminated regions (true positives) with a low incidence of false positives. While the number of wavebands was reduced to 2% of the original set, the authors did not link these key wavebands to any chemical components in the chicken or contaminants possibly driving the prediction.

High price free range and cheaper broiler chicken fillets were separated based on a full spectrum model, 9 optimal wavebands (417, 516, 550, 578, 639, 669, 717, 925 and 973 nm), 30 textural features, and a fusion of optimal spectral and textural features (Xiong, Sun, Pu, Zhu & Luo, 2015). PLS-DA and radial basis function (RBF) SVM were compared, with RBF-SVM performing best. The full spectrum RBF-SVM model achieved 90% classification accuracy of the prediction set, SPA-RBF-SVM achieved 87%, texture RBF-SVM achieved 70%, and the combined SPA-texture-RBF-SVM performed best with 93%. These results suggest that classification capabilities may be enhanced by incorporating textural features into spectral imaging prediction models.

Fish and shellfish

In comparison to terrestrial animals, fish is highly perishable, whereby biochemical, physiochemical and microbial changes occur extremely quickly (Cheng et al., 2016). Freezing is the most commonly used preservation technique, and thus several studies have focused on freeze-thawing issues. Frozen fish undergoes changes in nutritive value, texture, and other functional properties, and can thus be regarded as an inferior product. As water loss can be a major determining factor for these changes, Cheng et al. (2016) predicted the drip loss from fish fillets over time after freeze-thawing. Fillets were frozen for 24 h at -20 °C, and subsequently moved to 4 °C for 1, 2, 4 and 6 days. The drip loss of the samples was measured and hyperspectral images were acquired (400 – 1000 nm; 381 wavebands). Optimal wavebands were selected using GA (8 wavebands), SPA (7 wavebands) and their combined algorithm (5 wavebands). Although the method used to combine the two

Stellenbosch University https://scholar.sun.ac.za

algorithms was not explained, the authors suggest that GA may have been used as a preliminary step to reduce the number of wavebands, and a secondary step of SPA was used to refine the selection further. The wavebands identified in the GA-SPA selection were 432 nm (related to textural properties), 500 and 588 nm (related to pigments, such as astaxanthin or heme pigments), 660 nm (related to leakage of water-soluble protein), and 980 nm (not discussed). SVM models were calibrated using the three sets of optimal wavebands, while an additional MLR model was calculated for the combined algorithm set only. The GA-SPA-MLR model performed best with a prediction R^2 of 0.93 and the lowest RMSEP of 1.12% drip loss. Prediction maps were generated using the GA-SPA-MLR model to show drip loss distributed throughout each fillet, with one of three dummy variables (fresh, semi-fresh and inedible) assigned to the overall object.

Drying is an alternative preservation technique to freezing, where water availability is reduced to the point at which microbial life can no longer be supported within the product. Moisture content is thus an important processing control point that should be monitored to ensure optimal quality, taste, shelf-life and price. The moisture content of prawns dried for different times was measured (Wu et al., 2012a). A hot wind oven was used to dry fresh prawns for 0, 30, 70, 110, 150, and 200 minutes, after which hyperspectral images were acquired (416 – 1030 nm; 482 wavebands). Methods of image segmentation were explored to generate two image masks. The background was removed first using manual brushing, and the resulting mask was compared to automated background removal using a weighted threshold based on the wavebands 655 nm (red), 551 nm (green), and 449 nm (blue). Full PLS regression and LS-SVM models were calculated based on both the manual and automated masks. The prediction R^2 and RMSEP values demonstrated that the automatic mask was comparable or improved from the manual mask, and the automatic mask was chosen for the remainder of the study. SPA was employed to reduce the number of wavebands to 12, namely 428, 445, 544, 569, 629, 672, 697, 760, 827, 917, 958, and 999 nm. The visible wavebands (428 – 760 nm) were related to the colour changes occurring during drying, while the NIR wavebands were related to chemical components including 827 nm (N-H in protein), 917 nm (C-H in fat), 958 nm (major moisture band due to O-H) and 999 nm (O-H in water). PLS regression, LS-SVM and MLR models were calculated, where R^2 values were 0.96, 0.98 and 0.97, respectively, and RMSEPs were 2.6, 1.5 and 2.3% moisture, respectively. While the SPA-LS-SVM model performed best overall, it was noted that the simple SPA-MLR technique performed acceptably for this application and would be easier to implement for industry application. Pixel-wise visualisation of the moisture distribution was thus achieved using the SPA-MLR model.

The WHC of fish has a large effect on texture, and cannot currently be measured directly or non-destructively. WHC of fresh salmon fillets has been determined using two spectral imaging systems of different ranges, namely instrument 1 (400 – 1000 nm; 121 wavebands) and instrument 2 (897 – 1753 nm; 256 wavebands) (Wu & Sun 2013a). Four measures of WHC were recorded, including total liquid lost (water and fat), water lost, fat lost and water retained. Full PLS regression and LS-SVM models were calculated for all four measures using data from each instrument, and it was concluded that the Vis-NIR range used by instrument 1 was best suited for WHC determination. This was potentially due to water absorption occurring to an undesirably high extent for the NIR region of instrument 2, while instrument 1 captured a more balanced range

Stellenbosch University https://scholar.sun.ac.za

of both colour and one prominent water band at 980 nm. Optimal wavebands were selected using CARS, where four sets of wavebands, ranging 9 to 13 wavebands each, were chosen for each WHC parameter. CARS-PLS regression was found to be the best approach, and all parameters were successfully predicted with R^2 values ranging 0.65 to 0.93. Furthermore, a drop in RMSEP was observed for all parameters when CARS was employed, indicating improved prediction capability using optimal wavebands.

As salmon is a high value product, appearance is important to ensure consumer acceptance for purchase. Colour plays a prominent role in this regard, and has thus been evaluated (Wu et al., 2012b). NIR hyperspectral images (964 – 1631 nm; 200 wavebands) and reference colourimeter L*a*b* colour measurements were collected. The aim of the study was to explore full PLS regression models for L*, a* and b* separately, followed by the selection of an optimal waveband set for each of the three colour parameters, and finally selecting the single set of wavebands for complete L*a*b* prediction. The three sets of optimal wavebands selected for individual L*, a* and b* prediction contained 4, 6 and 10 wavebands each, respectively. In comparison with the three full PLS regression models for the individual parameters, the three SPA-PLS regression models performed with approximately equal prediction capability, where prediction R^2 for the three parameters ranged 0.75 to 0.87 and RMSEP values ranged 1.54 to 2.19. Thirteen optimal wavebands were selected in total, as some wavebands appeared in more than one of the three sets. A second round of optimal waveband selection was performed to reduce this number further. One by one, a variable was removed to observe if the prediction result of each parameter differed significantly. If prediction worsened, the waveband was retained. The final set of 7 optimal wavebands maintained prediction capability throughout the parameters, namely 964, 1024, 1081, 1105, 1161, 1295, and 1362 nm, but the authors did not assign these important bands to chemical components in the sample. For industry implementation, an MLR model was considered for its favourable simplicity. It was found that the MLR model of best fit for L* and a* utilised only 3 of the 7 wavebands each, with 2 common and two unique wavebands each. Thus, if a multispectral system for predicting L* and a* only was a sufficiently accurate measure of colour, it could be designed using only four band-pass filters. As the study aimed to predict all three parameters, the MLR prediction of b* was still required, and the current envisaged system would thus use 7 filters.

Modified atmosphere packaging (MAP) has been developed to prolong the freshness of food products, including fresh fish and fish products (Davis, 1998). This is a packaging method in which the proportions of gases contained in the package of a food product differ from the proportions of dry air, namely 78% nitrogen, 21% oxygen, 1% argon, 0.04% carbon dioxide (CO_2). In MAP, CO_2 is often used to replace air, as it is bacteriostatic, reduces oxidation of the polyunsaturated fatty acids and can affect colour changes seen during storage. The effect of three packaging methods on salmon was compared, specifically the use of air, 60% CO_2 and 40% nitrogen MAP, and vacuum packing (Sone, Olsen, Sivertsen, Eilertsen & Heia, 2012). Packaged samples were kept at 4 °C for 16 days, and hyperspectral image acquisition (400 – 1100 nm; 64 wavebands) was conducted every 48 h. As the study aimed to differentiate the effects of packaging types, only measurements from day 4 onwards were used. As the aim of the study was to determine packaging type and not duration of storage, the three classes modelled included all days from each of the three packaging types. Three two-way

Stellenbosch University https://scholar.sun.ac.za

PLS regression models were calculated (i.e. air vs. MAP, air vs. vacuum and MAP vs. vacuum), and RCs were used to select five optimal wavebands (606, 636, 665, 705 and 764 nm). K-nearest neighbours (KNN) models were calculated for the full and optimal waveband sets, and classification accuracy improved from 79% (SNV pre-treatment only) to 88% using feature wavebands. Furthermore, it was found that the wavebands 606 and 636 nm were strongly associated to haem pigment changes and could be used alone to achieve 69% correct classification.

The microbial contamination of salmon has been studied numerous times. Wu & Sun (2013b) determined TVC using two spectral imaging systems, namely instrument 1 (400 – 1000 nm; 121 wavebands) and instrument 2 (950 – 1600 nm; 94 wavebands). Full PLS regression and LS-SVM models were calculated for both ranges. Instrument 1 gave the best prediction capability, with RMSEPs of 0.46 log CFU for PLS regression and 0.29 log CFU for LS-SVM compared to 0.51 and 0.34, respectively, for instrument 2. The authors again sited lower water absorption for the superior detection in the VNIR region, as in their earlier study on salmon WHC (Wu & Sun 2013a). Due to its better performance, only instrument 1 was used for CARS optimisation. A set of 8 optimal wavebands was selected, namely 495, 535, 550, 585, 625, 660, 785 and 915 nm. The resulting RMSEPs of PLS regression and LS-SVM improved to 0.28 and 0.27 log CFU, respectively. Lactic acid bacteria (LAB) has also been determined in salmon (He, Sun & Wu, 2014). Fresh samples were stored at 4 °C for 12 days, and both hyperspectral image acquisition (900 – 1700 nm; 239 wavebands) and conventional microbiological testing were conducted every 48 h to calibrate a full LS-SVM model for predicting LAB. A prediction R^2 of 0.93 and a RMSEP of 0.52 log CFU were achieved. CARS was conducted to select 8 optimal wavebands, 924, 931, 964, 1068, 1262, 1373, 1628 and 1668 nm. Both LS-SVM and MLR models were calculated based on this set. The CARS-LS-SVM model performed best, and despite removing 97% of the wavebands, achieved the same R^2 of 0.93 as the full model and a similar RMSEP of 0.53 log CFU. The detection of *Enterobacteriaceae* was conducted using the same instrument as the previous study (He & Sun, 2015). Samples were stored at 4 °C for 0, 3, 6, 8, 10 and 13 days before imaging and conventional microbiological testing. A full PLS regression model, RC-PLS regression model (11 wavebands) and SPA-PLS regression model (8 wavebands) were calculated. Both prediction R^2 and RMSEP were improved in the two optimised models, with very similar performance (both R^2 = 0.95; RC-PLS RMSEP = 0.48 log CFU; and SPA-PLS RMSEP = 0.47 log CFU), while the SPA-PLS regression model was found to be most robust with the smaller difference between RMSEC and RMSEP. The SPA-PLS regression model was transferred to each pixel of the images to visualise the regions and spread of *Enterobacteriaceae*.

The microbial spoilage of fresh fish fillets was predicted by Cheng & Sun (2015). Samples were kept at 4 °C for 0, 5 and 10 days before being tested for TVC and imaged in the range 400 – 1000 nm (381 wavebands). SPA was conducted to select 7 optimal wavebands, 410, 488, 553, 665, 750, 825 and 960 nm. The authors gave little explanation as to the importance of these wavebands. PLS regression and LS-SVM were compared for both full and SPA optimised models. LS-SVM performed best in both the full and SPA models, although results for all four models were extremely close. The SPA-LS-SVM resulted in a prediction R^2 of 0.92

Stellenbosch University https://scholar.sun.ac.za

and RMSEP of 0.53 log CFU, resulting in an increase in error of only 6% despite removing 98% of the spectral factors.

Cereals and legumes

Cereal products are a major source of staple foods, providing around 85% of the food energy consumed on earth (Murphy, 2011). NIR hyperspectral imaging has been widely applied in cereal science research, and more recently in practical industry applications (Sendin et al., 2018b). Foreign material was separated from various cereal commodities in an older study (Wallays, Missotten, Baerdemaeker & Saeys, 2009). Wheat, barley and maize were each separated from matter other than grain (MOG), although only results for the wheat separations were detailed. Hyperspectral images were captured in the range 400 to 950 nm, and the original spectral resolution of 0.6 nm was adjusted to 9.6 nm by averaging every 15 wavebands, resizing the original 900 wavebands to a set of 57. Five replications of GA were calculated on the 57 averaged bands, and the 5 wavebands appearing in all replications were selected as the optimal waveband set. As a window of two wavebands was used, each variable selected is a range of two wavebands, with the five wavebands ranges chosen including 465–475, 522–532, 676–705, 849–858 and 906–945 nm. While the number of selected variables is given as 5, closer inspection reveals that the waveband range 676–705 nm is larger than the others, and likely consists of two adjacent GA identified variables (676–685 nm and 695–705 nm). As pixel-wise PLS-DA classification was performed, dummy variables were assigned as 0 for kernels and 1 for MOG and an RMSECV of 0.26 was achieved, however no classification accuracy was given.

The variety of a cereal commodity can be an important parameter for determining the price, use, nutrition, and quality of a consignment. However, manual inspection cannot be used for distinguishing all varieties, and thus spectral imaging is a possible non-destructive technique for variety determination. Varieties of maize can be broadly classified as either waxy (high amylopectin content) or sweet (high sugar content) varieties. Waxy and sweet maize kernels were separated using a system operating in the range 400 – 1000 nm (380 wavebands) (Wang, Sun, Pu & Zhu, 2016). Optimal wavebands were selected using SPA (438, 487, 511, 516, 700, and 897 nm), while textural features were extracted by gray-level run-length matrix analysis. A series of five LS-SVM models were calculated, based on the raw full spectrum (91% classification accuracy), detrending pre-processed full spectrum (92%), six optimal wavebands only (87%), five textural features only (85%), and a fusion of optimal wavebands and textural features (89%). Despite removing 98% of the spectral information, the optimal waveband model only suffered a 5% decrease in classification accuracy, and was slightly improved by incorporating five textural features. As these predictions were made on a pixel-wise basis, the incorrect classifications were spread out among the kernels, with the published figures showing kernels with most pixels correctly classified. Considering this high pixel-wise classification accuracy, it could be suggested that these small regions of misclassification could have been averaged out by the implementation of an object-wise classification approach. Furthermore, as a single kernel can only be from one variety, a whole kernel (object) should be considered the smallest unit of measurement (Sendin, Manley & Williams, 2018a). Varieties of rice have also been discriminated using the same system (400 – 1000 nm; 380 wavebands) (Wang et al.,

Stellenbosch University https://scholar.sun.ac.za

2015a). A full PCA model was calculated, which performed comparatively well with an average classification accuracy for the three varieties of 89%. Seven optimal wavebands were selected using RCs based on PLS-DA, including 419, 452, 593, 613, 743, 784 and 966 nm. Three back propagation neural networks (BPNN) models were calculated, based on the optimal wavebands (90% classification accuracy), textural features (88%) and a fusion of both (94%). These models demonstrated superior classification capability than PCA due to the self-learning and self-adjustment nature of nonlinear models, like BPNN, when applied to closely related classes. In order to fairly comment on the results of the full waveband range versus the optimised set, it would have been suggested that a full BPNN model be calculated, as BPNN is expected to outperform PCA regardless of the adjustments to the spectral data.

Three varieties of black beans were differentiated in the spectral range 501 to 1000 nm (386 wavebands) (Sun, Jiang, Mao, Wu & Li, 2016). The use of spectral data, texture features and the fusion of both was investigated. Thirteen optimal wavebands were selected using SPA (504, 507, 512, 516, 522, 529, 692, 733, 766, 815, 933, 998, and 1000 nm), and image feature extraction was performed using gray level co-occurrence matrices. Three classification modeling techniques were explored, namely PLS-DA, SVM and KNN. Generally, PLS-DA performed best, with an average classification accuracy of 93% for spectral data only, 87% for texture features only and 98% for the fusion. Throughout the modeling techniques, the fusion model had better classification capability than the spectral model, further demonstrating the commonly overlooked importance of incorporating image texture features with spectral data.

Genetically modified (GM) maize kernels have been separated from non-GM kernels (Feng et al., 2017). Two sample groups were used, non-GM maize kernels and GM maize kernels with *cry1Ab/cry2Aj-G10evo* genes added. These genes impart insecticidal and herbicidal tolerant traits, but could pose environmental risks related to gene flow if not correctly monitored. PLS-DA and SVM models were based on the full spectra (874 – 1734 nm; 200 wavelengths) and CARS selected optimal wavebands (54 wavebands). Of the wavebands selected, the authors highlighted three regions, firstly 1250–1350 nm due to the combination of the first overtone of Amide B and the fundamental vibration of Amide III. The other two regions, 1410 – 1480 nm and 1520–1600 nm, were related to N–H stretching vibrations. These spectral differences were attributed to the conformational and compositional changes caused by the included gene. Classification accuracy of the prediction set was very high for all four models, with 99% accuracy for both the full PLS-DA and CARS-PLS-DA models, and 97 and 98% for the full SVM and CARS-SVM, respectively. While pixel-wise predictions were initially made, image segmentation was performed to generate object-wise classification maps from the CARS-PLS-DA predictions, allowing clear visualisation of the class predictions for industry application.

Fresh maize kernels were studied for changes in texture over the course of a week in cold storage (4 °C), where the parameters hardness, springiness and resilience were measured (Wang, Pu, Sun, Liu, Wang & Xiong, 2015b). Instron universal testing machine measurements were recorded on days 0, 3 and 7, as well as hyperspectral image acquisition (400 – 1000 nm; 380 wavebands). SPA was performed to identify optimal waveband sets for each paramenter, selecting 7 wavebands for hardness (400, 416, 450, 501, 517, 530, 980 nm), 7 for springiness (400, 403, 420, 525, 552, 749, 835 nm), and 6 for resilience (436, 482, 532, 700, 735, 939 nm).

Stellenbosch University https://scholar.sun.ac.za

PLS regression models were calculated based on raw full spectra, orthogonal signal correction (OSC) pre-treated spectra, and a set of optimal wavebands, as selected using SPA. Separate models were developed for each of the three texture parameters, where hardness was predicted best throughout the study, followed by springiness and lastly resilience. The prediction capability for each parameter improved with the use of OSC, where the prediction R^2 of the hardness parameter improved from 0.73 to 0.90 and RMSEP dropped from 0.33 to 0.05 N. The prediction of all parameters by the SPA-PLS regression models did not perform as well as the OSC pre-treated full PLS regression models, with a hardness prediction R^2 of 0.83 and RMSEP of 0.2 N. However, with only 7, 7 and 6 wavebands required for prediction of hardness, springiness and resilience, respectively, the SPA-PLS regression models were successfully used for the visualisation stage of the study in favour of the simplicity offered to on-line implementation.

Organic spelt flour (OSF) was differentiated from non-organic spelt flour (SF), as well as from organic wheat flour (OWF) and rye flour (RF) (Su & Sun, 2016). Historically, spelt was the predominant cereal crop produced in Europe, but has been largely replaced with wheat. Although less commercially viable, spelt has better flavor and nutritional value, and thus worth about twice the price of wheat. Spelt is also resistant to various pathogens, and is well suited to organic farming practices. Concerns regarding adulteration of organic spelt flour with various replacement flours is a concern, and both rapid qualitative (PLS-DA) and quantitative (PLS regression and MLR) detection by hyperspectral imaging was investigated. Full PLS-DA models (957 – 1625 nm; 200 wavebands) were calculated for the separation of pure OSF, SF, OWF and RF samples, as well as exploring various pre-treatments. Classification results were excellent, with cross-validated R^2 values ranging 0.93 to 0.998, and mean-centering (MC) was chosen as pre-treatment. Eight optimal wavebands were chosen using first-derivative and mean-centering iteration algorithm (FMCIA), namely 1145, 1192, 1222, 1349, 1359, 1396, 1541 and 1567 nm. The authors did not offer any explanation for the role of these wavebands in discriminating between the flour types. The MC-FMCIA-PLS-DA approach achieved a mean R^2 value of 0.96. For quantification, OSF was adulterated with each of the other three flours individually in 25 levels ranging 3 to 75%. Full PLS regression models performed well with prediction R^2 values ranging 0.98 to 0.995 and RMSEPs of 0.016 to 0.043%. Both PLS regression and MLR models were calculated based on the eight FMCIA wavebands, where the two methods performed with almost equal prediction capability throughout. Although performing slightly poorer in comparison with the full PLS regression models, results may be considered good (R^2 = 0.92 – 0.97; RMSEP = 0.038 – 0.061%) while utilising only 4% of the wavebands. The pixel-wise visualisation of both the FMCIA PLS-DA and PLS regression models clearly revealed differences between samples, despite little observable difference in the digital photographs.

Fruit and vegetables

The monitoring of fruit and vegetable quality has always been crucial for the industry, where the premium quality produce can be sold for fresh consumption at a high price and that of lower quality can be removed and allocated for processing or other uses (Elmasry et al., 2012). The current methods for internal quality measurement are mostly destructive and time-consuming, and only a small number of fruits are tested. A non-

Stellenbosch University https://scholar.sun.ac.za

invasive and rapid sorting method that could be used to screen every fruit, such as spectral imaging, would be of great use to the industry. Several internal characteristics provide a good indication of a fruit's quality, including soluble solids content (SSC), moisture content (MC), acidity (usually pH value) and firmness. All four of the aforementioned quality parameters were evaluated in apples (Dong & Guo, 2015). Stored in perforated polyethylene bags at room temperature, both hyperspectral image acquisition (928 – 1661 nm; 222 wavebands) and conventional testing were conducted every week for 13 weeks. This thorough study explored several chemometric approaches, namely two variable selection methods, SPA and uninformative variable elimination algorithm (UVE), and three quantitative modelling techniques, PLS regression, LS-SVM and BPNN. The number of variables chosen using SPA for SSC, MC, pH and firmness were 17, 23, 8 and 11, respectively, and 135, 122, 108 and 71, respectively, using UVE. By reviewing the prediction R^2 and RMSEP values for the full spectrum, SPA and UVE sets using the three modelling techniques for each parameter (36 models in total), it is apparent that the prediction capability was not greatly affected by the reduction of waveband numbers. The SPA-LS-SVM models performed best in almost every instance when compared to the other waveband selection and modelling technique combinations. Furthermore, the number of wavebands selected using SPA was far less than UVE, and thus an on-line system based on this research could be built more easily and cheaply with the SPA waveband sets.

The SSC and firmness of pears has been investigated while comparing optimal waveband selection methods (Fan, Huang, Guo, Zhang & Zhao 2015). Samples were stored for two days and imaged (400 – 1000 nm; 774 wavebands) at room temperatures prior to acquiring reference measurements for the calibration of PLS regression models. The performance of different pre-processing treatments was compared using the full spectrum. However, no significant improvement was observed, and it was decided to use untreated spectra. The waveband selection approaches included SPA only, CARS only, and a combined approach whereby CARS was used to eliminate the majority of wavebands and SPA was performed in a second step to refine the selection. The combined CARS-SPA approach performed best for the prediction of SSC and firmness, with the fewest wavebands required (25 for SSC; 22 for firmness). Prediction R^2 values increased in comparison to the full models, while the RMSEP dropped by 6% for SSC (0.51 to 0.48 °Brix) and 3% for firmness (0.75 to 0.72 N), with removing *ca.* 97% of the spectral information. In a similar study, Li et al. (2016) predicted pear SSC, firmness and variety in the same range 400 – 1000 nm (998 wavebands). As SSC and firmness required quantification, PLS regression was used, and models based on both the full spectrum and a set of SPA selected wavebands were calculated for each. Using 51 wavebands for SSC and 58 for firmness, prediction R^2 values for both parameters were greatly improved from 0.78 to 0.98 for SSC and 0.93 to 0.995 for firmness. Furthermore, RMSEPs were dramatically reduced by 78% for SSC (0.15 to 0.032 °Brix) and 74% for firmness (0.24 to 0.063 N). While the study achieved great results, the waveband sets were about twice the size of the wavebands sets identified by Fan et al. (2015). This allows one to compare the dual approach of CARS-SPA with regular SPA in its ability to reduce the spectral dimension of a dataset. The classification of the three pear varieties was only performed using a full Fischer LDA model achieving an average classification accuracy of 96%.

Stellenbosch University https://scholar.sun.ac.za

The maturity of cherries was quantified based on SSC and pH predictions (Li et al., 2018). Hyperspectral images were acquired in the range 972 to 1649 nm (200 wavebands), and GA and SPA were employed to reduce the number of spectral variables. The authors only provide limited results of GA selection, where 54 bands were selected for SSC and 24 for pH. The specific wavebands selected were not disclosed, nor any results of SPA. The authors did briefly discuss general areas highlighted by GA, including the importance of 972–1100 nm for pH determination due to association with O-H and N-H in acidic compounds, and 1160 nm (C=O in sugars), 1170 nm (C-H in sugars) and 1194 (C-H in sugars) for SSC determination. The prediction capability of principal component regression (PCR) and PLSR were compared for modelling the full spectrum, while MLR was investigated for the optimal waveband sets as it is easily implemented in an industrial setting. The full PCR and PLSR models performed with no significant difference. The prediction R^2 and RMSEP values for SSC of 0.84 and 1.3 °Brix, respectively, using PCR, and 0.83 and 1.3 °Brix, respectively, using PLSR. The R^2 and RMSEP results for pH were 0.80 and 0.60 using both methods. The results for GA selection was slightly better than for SPA, with similar R^2 values to the full models for both SSC (0.86) and pH (0.82), and decreased slightly in error to 1.2 °Brix (9%) and 0.057 (5%). In addition, all cherry samples were visually graded as maturity stage 1, 2 or 3. Although very little description on the development of the model was provided, such as spectral variables used or size of calibration and prediction sets, an LDA model was calculated to classify the cherries according to maturation with a classification accuracy of 96.4%.

The flavour and odour of garlic is largely dependent on SSC and allicin content, which has been determined by Rahman et al. (2018). Two instruments, namely instrument 1 (400 – 1000 nm; 128 wavebands) and instrument 2 (1000 – 1700 nm; 275 wavebands) were explored. Full PLSR and LS-SVM models revealed that both ranges had good prediction capability for SSC (prediction R^2 values ranging 0.82 to 0.87), but allicin content was only modelled acceptably in the 1000 to 1700 nm range, with prediction R^2 values of 0.86 and 0.87, compared to the range 400 to 1000 nm with 0.56 and 0.65. To select optimal wavebands, RCs, SPA and VIP were evaluated. For predicting SSC in the range 400 to 1000 nm, sugar content was related to 838, 888, 913 and 979 nm, and cellulose to 758, 816, 860, 905, 920 and 979 nm. Highlighted wavebands in the range 1000 to 1700 nm for SSC prediction were 1050 to 1175 nm (combination C–H second overtone and O–H overtone) and 1400 nm (O–H first overtone). Allicin was only further investigated in the range 1000 to 1700 nm, where the second overtone of –CH=CH–, CH_2=CH_2 and C–H bonds (1100 – 1200 nm) played an important role. The results for SSC were explored first, where the comparison of PLSR and LS-SVM models using all three waveband selection methods revealed superior performance by LS-SVM. Thus, LS-SVM was selected as the only modelling technique for the prediction of the second parameter, allicin content. Overall, instrument 2, which operated in the short-wave infrared (SWIR) region, performed best for both parameters, and the best models were SPA-LS-SVM for SSC (10 wavebands), with a prediction R^2 of 0.90 and SEP of 1.01% for SSC, and VIP-LS-SVM for allicin content (18 wavebands), with 0.83 and 0.19 mg/g.

Colour of fresh produce is an important quality factor in determining consumer acceptability. The redness of litchi fruit is an indication of maturity, but can quickly degrade to a less attractive brown colour during storage, and thus the red pigment anthocyanin has been quantified (Yang, Sun, Pu, Wang & Zhu 2015).

Stellenbosch University https://scholar.sun.ac.za

Samples were stored at 27 °C and 85% relative humidity, and images were acquired daily from days 0 to 5 in the spectral range 350 to 1050 nm (431 wavebands). SPA and SWR were implemented for waveband selection, resulting in 8 wavebands identified by SPA (368, 458, 614, 678, 903, 988, 1004, 1020 and 1042 nm), and 11 by SWR (423, 453, 587, 630, 676, 707, 762, 805, 867, 911 and 977 nm). A full RBF-SVM model was calculated, as well as RBF-SVM models based on waveband sets selected by SPA and SWR. The RBF-SVM-SPA and RBF-SVM-SWR models were then fused in a single RBF neural network (RBF-NN) model. The full RBF-SWM model performed best with a prediction R^2 of 0.91 and RMSEP of 0.51%, with the SPA waveband set (R^2 = 0.71; RMSEP = 0.84%) resulting in the superior prediction over SWR (R^2 = 0.67; RMSEP = 0.93%). The fusion RBF-NN model achieved better results than both waveband selection methods alone (R^2 = 0.87; RMSEP = 0.61%). This study demonstrated the advantage of model fusion, where integrating SPA and SWR overcame the shortcomings of the individual algorithms, thus improving the prediction capability of the models.

Edible films are applied to a variety of fruits to delay spoilage by controlling the transfer of moisture, oxygen, aromas and solutes. However, to reduce costs, producers may use unsafe industrial wax instead of edible wax. Li et al. (2017) differentiated the type of wax applied to pears, where edible wax, industrial wax and no wax were used as classes. SPA was utilised to select a set of 11 optimal wavebands (402, 454, 543, 689, 718, 747, 976, 1016, 1020, 1022 and 1025 nm.). The industrial wax was mainly composed of C_{16}–C_{20} N-alkanes, and absorbance by C–H was highlighted in the region 720 to 780 nm. Absorbance by O–H in the region 1000 to 1130 nm also played an important role. The SPA waveband set was used to calibrate MLR and LDA models. While both models performed well, each model made misclassifications of one class only (either industrial or edible wax). The MLR model did not identify all industrial wax samples (4% error), while LDA misclassified edible wax samples (8% error). Considering the implication of mistaking industrial wax samples (unsafe) as edible, the authors selected the LDA model as the better model for implementation, with an overall classification accuracy of 96%.

While physiochemical quality parameters are a large focus for predicting fresh produce quality, microbial spoilage can be a hugely detrimental issue. Contaminated fruits and vegetables should be identified as soon as possible, as individual infections can quickly spread to the whole batch and cause great economic losses. The detection of various fungal and bacterial contaminations has been the focus of many studies. Two similar studies have been conducted on the detection of apple decay caused by *Penicillium* fungus (Zhang et al., 2015a; Zhang et al., 2015b). For both studies, 120 apples (20 calibration; 100 validation) were acquired, where 20 were assumed to be healthy and 100 were internally inoculated with *Penicillium* and stored at room temperature for 3 to 4 days. Images were captured in the spectral range of 400 to 1000 nm (*ca.* 750 wavebands), with the rotten sections of inoculated samples facing toward the camera. The two studies explored different approaches to data analysis to best classify rottenness in apples in an industrial setting (simplest models). Zhang et al. (2015a) explored the use of SPA, where a range of 1 to 28 variables was selected and evaluated using a simple MLR model and resulting RMSEP. The two classes were assigned dummy variables of 0 (sound) and 1 (rotten), and the lowest RMSEP value (0.078) was found at 4 wavebands, which were subsequently chosen as the optimal waveband set. The ability of minimum noise fraction (MNF) transformation to improve the

Stellenbosch University https://scholar.sun.ac.za

classification capability was also investigated, and found to be effective. The MNF algorithm aids in identifying the rotten regions, to select the best region of interest (ROI) for spectral data extraction. A SPA-PLS-DA-MNF model was calibrated using the optimal wavebands (563, 611, 816, and 966 nm) to classify sound and rotten apples, which resulted in an overall classification accuracy of 98% for 100 samples, including 20 sound (20 correct) and 80 rotten apples (78 correct). Zhang et al. (2015b) investigated a second data analysis approach involving PCA and independent component analysis (ICA). PCA and ICA are both techniques used to calculate vectors to make sense of a dataset. PCA aims to best explain the variability within the dataset to reduce the dimensionality, while ICA identifies sub-elements in order to separate data (e.g. sound and rotten regions of an apple in the image) (Villa, Chanussot, Jutten, Benediktsson & Moussaoui, 2009). PCA was calculated on the full data, and score images were used to visually identify which PC accounted for variation between sound and rotten regions of the apples. Rottenness was most closely linked to PC3, and thus optimal wavebands were selected based on their loadings for PC3. While 6 were identified, only 2 wavebands (810 and 970 nm) were selected due to their dramatic peaks, which are located relatively closely to two of the wavebands selected using SPA (816 and 966 nm) in the previous study. However, the authors unfortunately did not discuss the importance of these wavebands regarding related chemical components in either study. ICA was calculated based on the 2 optimal wavebands, and score images were explored to reveal IC2 as the best basis for separating rotten and sound regions. A simple algorithm based on the weighting coefficients of the two wavebands in IC2, accompanied by thresholding and morphological filtering, was used to accurately segment rotten regions. An overall classification accuracy of 97% was achieved, based on the same validation set as the previous study, which included 20 sound (20 correct) and 80 rotten apples (77 correct). These studies were a good illustration of the wide variety of chemometric techniques currently available in hyperspectral imaging research, and demonstrated the potential for the development of accurate simplified models based on as few as two optimal wavebands.

Damaged strawberries, including mechanically bruised and *Rhizopus* inoculated (rotten) samples were separated from sound strawberries in the Vis-NIR range 380 to 1010 nm (440 wavebands) (Liu et al., 2018). MNF was utilised to detect the damaged ROIs, and a preliminary model based only on MNF transformed data achieved 84% classification accuracy for distinguishing heathy and damaged strawberries. Optimal wavebands were identified using SPA, namely 560, 604, 650, 675, 720, 771, 890, and 995 nm. The authors broadly attributed wavebands 560 to 720 nm to quality parameters: SSC, firmness index (FI) and total anthocyanin content (TAC). The wavebands 771 and 890 nm related to red colour, as well as C-H bonds in alkanes and C–O in esters. Absorption at 995 nm was attributed to free water content. One linear and two non-linear modelling techniques were calculated, namely PLS-DA, SVM and BPNN, respectively, based on the 8 identified optimal wavebands. Among these three models, SVM achieved the highest overall classification accuracy (93%), followed closely by BPNN (91%), and lastly PLS-DA (85%). PLS-DA is often used for fruit classification, where the basis of the PLS is a linear correlation between the spectral data and the constituent concentrations. However, low accuracy can be an issue in applications where samples exhibit non-linearity (i.e. absorbance not directly proportional to concentration), and this is likely the reason that the non-linear techniques performed

Stellenbosch University https://scholar.sun.ac.za

best in this study.

Sour skin is a bacterial disease in onions caused by *Burkholderia cepacia*, which can spread quickly during storage, posing both quality and safety issues. In a study by Wang et al. (2012), onions were inoculated and incubated at 30 °C and 80% relative humidity until infection was visibly apparent (4 to 5 days). Samples were imaged (950 – 1650 nm; 350 wavebands) immediately after inoculation (no disease development) and on the day infection was visible. Optimal waveband selection was conducted using PCA, where the maximum and minimum loading values of PC2 were selected (1070 and 1400 nm). Log ratio images using the two wavebands were calculated. This improved classification capability by magnifying the spectral difference between the two classes, allowing the sound and infected regions to be clearly discriminated, and visibly minimising image noise by reducing redundancy in the feature space. Pixel-wise image segmentation was conducted based on the log ratio images threshold of 0.45, which was selected based on the best classification accuracy (80%) from a series of LDA models. Image texture features were also extracted from the log ratio images, and an SVM model based on three parameters of the grey values (maximum, contrast, and homogeneity) was found to have superior classification capability (87%). While this study's methods for waveband selection, data treatment and modelling were simple, it was not as effective as other sophisticated data analysis techniques (e.g. SPA, MNF or SVM), and was outperformed by a model based on image texture alone.

Tea

The colour change in tea leaves during the drying process have been studied by Xie et al. (2014). Fresh tea leaves of three different cultivars were imaged before drying (400 – 1030 nm; 496 wavebands), and at 4 intervals during a drying period of 10 minutes at 80 °C. The image acquisition was complemented with reference L*a*b* colour measurements. A large number of models were calculated in this study (*ca.* 21), beginning with a series of full PLS regression models for pre-treatment optimisation. It was found that using the raw spectra gave the best prediction results (RMSEP = 1.20 – 1.98). Full PCR and LS-SVM models were also calculated using the raw data, with similar RMSEP results. The calculation of MLR, PLS regression and PCR models followed, based on waveband sets selected using CARS (L*: 48; a*: 34; b*: 26) and SPA (L*: 7; a*: 6; b*: 11). The aim of these models was to determine the three colour parameters in samples, and individual models were calculated for each parameter. L* was predicted best by CARS-MLR (RMSEP = 1.16), a* by SPA-LS-SVM (RMSEP = 1.15), and b* by CARS-LS-SVM (RMSEP = 1.76). While evaluating these results, it must be considered that the SPA models contained fewer wavebands than the CARS models, and often performed with almost equal prediction capability. A full LS-SVM was also calculated to classify samples according to the five different drying periods, which achieved an overall classification accuracy of 86%. This study demonstrated potential for tea colour prediction using optimal waveband spectral imaging. However, if this method were to be implemented practically, it is suggested that a single suitable waveband set for the prediction of all three parameters be selected. Furthermore, when selecting the 'best' method, the accuracy of models should be weighed against simplicity, as all models performed with very good prediction capability.

Stellenbosch University https://scholar.sun.ac.za

CONCLUSION

Hyperspectral imaging is an analytical technique that acquires a wealth of chemical and physical information by integrating spectroscopy and imaging in a single platform. While the technique has been widely utilised throughout food science research, it is not often implemented for routine analysis in industry. The current hyperspectral imaging instruments utilise high-cost cameras, which capture voluminous amounts of data that prevent acquisition times appropriate for on-line application. Furthermore, continuous NIR spectra, as are gathered by hyperspectral instruments, are associated with multicollinearity issues that may incorporate noise due to the complex interactions between the numerous X-H bonds present in food samples, and the congruent wavebands. These issues can be minimised by developing a multispectral imaging method for a specific application, where a few optimal wavelengths are carefully selected to extract the most useful information from the original hyperspectral data. In theory, a multispectral system can be designed using only these optimal wavebands. Waveband selection methods have been successfully applied to greatly improve spectral imaging prediction capability in food quality, safety and fraud applications. Many applications reviewed investigated methods such as GA, SPA, RCs and SWR, where it was often found that the principles of the different algorithms lead to varying results. It is important to realise that there is no universally ideal waveband selection technique, and one must consider the problem at hand, size of the dataset, ease of implementation and required prediction capability. It is likely that with the rapid image acquisition speed, low camera cost and high accuracy offered by simplified multispectral imaging systems, the on-line evaluation of foods using this technology will become more widely implemented in the near future.

REFERENCES

Abdi, H. (2010). Partial least squares regression and projection on latent structure regression (PLS Regression). *Wiley Interdisciplinary Reviews: Computational Statistics,* **2**, 97-106.

Araújo, M. C. U., Saldanha, T. C. B., Galvao, R. K. H., Yoneyama, T., Chame, H. C., & Visani, V. (2001). The successive projections algorithm for variable selection in spectroscopic multicomponent analysis. *Chemometrics and Intelligent Laboratory Systems,* **57**, 65-73.

Barbin, D. F., ElMasry, G., Sun, D. W., Allen, P., & Morsy, N. (2013). Non-destructive assessment of microbial contamination in porcine meat using NIR hyperspectral imaging. *Innovative Food Science & Emerging Technologies,* **17**, 180-191.

Burger, J., & Geladi, P. (2006). Hyperspectral NIR imaging for calibration and prediction: a comparison between image and spectrometer data for studying organic and biological samples. *Analyst,* **131**, 1152-1160.

Stellenbosch University https://scholar.sun.ac.za

Calvini, R., Amigo, J. M., & Ulrici, A. (2017). Transferring results from NIR-hyperspectral to NIR-multispectral imaging systems: A filter-based simulation applied to the classification of Arabica and Robusta green coffee. *Analytica Chimica Acta,* **967**, 33-41.

Caneca, A.R., Pimentel, M.F., Galvão, R.K.H., da Matta, C.E., de Carvalho, F.R., Raimundo Jr, I.M., Pasquini, C. and Rohwedder, J.J. (2006). Assessment of infrared spectroscopy and multivariate techniques for monitoring the service condition of diesel-engine lubricating oils. *Talanta*, **70**, 344-352.

Cheng, J.-H., & Sun, D. W. (2015). Rapid and non-invasive detection of fish microbial spoilage by visible and near infrared hyperspectral imaging and multivariate analysis. *LWT-Food Science and Technology,* **62**, 1060-1068.

Cheng, J.-H., Sun, D. W., & Pu, H. (2016). Combining the genetic algorithm and successive projection algorithm for the selection of feature wavelengths to evaluate exudative characteristics in frozen–thawed fish muscle. *Food Chemistry,* **197**, 855-863.

Cheng, J.H., Nicolai, B., & Sun, D. W. (2017). Hyperspectral imaging with multivariate analysis for technological parameters prediction and classification of muscle foods: A review. *Meat Science,* **123**, 182-191.

Cheng, W., Sun, D. W., Pu, H., & Wei, Q. (2017). Chemical spoilage extent traceability of two kinds of processed pork meats using one multispectral system developed by hyperspectral imaging combined with effective variable selection methods. *Food Chemistry,* **221**, 1989-1996.

Cheng, W., Sun, D. W., Pu, H., & Wei, Q. (2018). Characterization of myofibrils cold structural deformation degrees of frozen pork using hyperspectral imaging coupled with spectral angle mapping algorithm. *Food Chemistry,* **239**, 1001-1008.

Cowe, I. A., & McNicol, J. W. (1985). The use of principal components in the analysis of near-infrared spectra. *Applied Spectroscopy,* **39**, 257-266.

Dale, L. M., Thewis, A., Boudry, C., Rotar, I., Dardenne, P., Baeten, V., & Pierna, J. A. F. (2013). Hyperspectral imaging applications in agriculture and agro-food product quality and safety control: A review. *Applied Spectroscopy Reviews,* **48**, 142-159.

Davis, H. K. (1998). Fish and shellfish. In B. A. Blakistone (Ed.), *Principles and Applications of Modified Atmosphere Packaging of Foods* (2 ed., pp. 194-238). Washington, D.C., USA: Springer.

Dong, J., & Guo, W. (2015). Nondestructive determination of apple internal qualities using near-infrared hyperspectral reflectance imaging. *Food Analytical Methods,* **8**, 2635-2646.

Elmasry, G., Kamruzzaman, M., Sun, D. W., & Allen, P. (2012). Principles and applications of hyperspectral imaging in quality evaluation of agro-food products: a review. *Critical Reviews in Food Science and Nutrition,* **52**, 999-1023.

Esbensen, K., & Geladi, P. (1989). Strategy of multivariate image analysis (MIA). *Chemometrics and Intelligent Laboratory Systems,* **7**, 67-86.

Stellenbosch University https://scholar.sun.ac.za

Fan, S., Huang, W., Guo, Z., Zhang, B., & Zhao, C. (2015). Prediction of soluble solids content and firmness of pears using hyperspectral reflectance imaging. *Food Analytical Methods*, **8**, 1936-1946.

Feng, X., Zhao, Y., Zhang, C., Cheng, P., & He, Y. (2017). Discrimination of transgenic maize kernel using NIR hyperspectral imaging and multivariate data analysis. *Sensors,* **17**, 1894.

Feng, Y. Z., & Sun, D. W. (2013a). Determination of total viable count (TVC) in chicken breast fillets by near-infrared hyperspectral imaging and spectroscopic transforms. *Talanta,* **105**, 244-249.

Feng, Y. Z., & Sun, D. W. (2013b). Near-infrared hyperspectral imaging in tandem with partial least squares regression and genetic algorithm for non-destructive determination and visualization of Pseudomonas loads in chicken fillets. *Talanta,* **109**, 74-83.

Feng, Y. Z., ElMasry, G., Sun, D. W., Scannell, A. G., Walsh, D., & Morcy, N. (2013). Near-infrared hyperspectral imaging and partial least squares regression for rapid and reagentless determination of Enterobacteriaceae on chicken fillets. *Food Chemistry,* **138**, 1829-1836.

He, H. J., & Sun, D. W. (2015). Selection of informative spectral wavelength for evaluating and visualising Enterobacteriaceae contamination of salmon flesh. *Food Analytical Methods,* **8**, 2427-2436.

He, H. J., Sun, D. W., & Wu, D. (2014). Rapid and real-time prediction of lactic acid bacteria (LAB) in farmed salmon flesh using near-infrared (NIR) hyperspectral imaging combined with chemometric analysis. *Food Research International,* **62**, 476-483.

Kamruzzaman, M., Barbin, D., ElMasry, G., Sun, D. W., & Allen, P. (2012). Potential of hyperspectral imaging and pattern recognition for categorization and authentication of red meat. *Innovative Food Science & Emerging Technologies,* **16**, 316-325.

Kamruzzaman, M., ElMasry, G., Sun, D. W., & Allen, P. (2013). Non-destructive assessment of instrumental and sensory tenderness of lamb meat using NIR hyperspectral imaging. *Food Chemistry*, **141**, 389-396.

Kamruzzaman, M., Makino, Y., & Oshita, S. (2016). Hyperspectral imaging for real-time monitoring of water holding capacity in red meat. *LWT-Food Science and Technology,* **66**, 685-691.

Khurana, N., Rathi, A., & Akshatha, P. (2011). Genetic algorithm: a search of complex spaces. *International Journal of Computer Applications,* **25**, 13-17.

Leardi, R. (2000). Application of genetic algorithm–PLS for feature selection in spectral data sets. *Journal of Chemometrics*, **14**, 643-655.

Li, B., Hou, B., Zhang, D., Zhou, Y., Zhao, M., Hong, R., & Huang, Y. (2016). Pears characteristics (soluble solids content and firmness prediction, varieties) testing methods based on visible-near infrared hyperspectral imaging. *Optik-International Journal for Light and Electron Optics,* **127**, 2624-2630.

Stellenbosch University https://scholar.sun.ac.za

Li, B., Zhou, Y., Zhao, M., Hou, B., Zhang, D., Wang, Q., & Huang, Y. (2017). Visible and Near-Infrared Hyper-Spectral Imaging for the Identification of the Type of Wax on Pears. *Journal of Food Processing and Preservation*, **41**, e12749.

Li, H., Liang, Y., Xu, Q., & Cao, D. (2009). Key wavelengths screening using competitive adaptive reweighted sampling method for multivariate calibration. *Analytica Chimica Acta*, **648**, 77-84.

Li, X., Wei, Y,, Xu, J,, Feng, X., Wu, F., Zhou, R., Jin, J., Xu, K., Yu, X. & He, Y. (2018). SSC and pH for sweet assessment and maturity classification of harvested cherry fruit based on NIR hyperspectral imaging technology. *Postharvest Biology and Technology,* **143**, 112-118.

Liu, D., Sun, D.-W., & Zeng, X.-A. (2014). Recent advances in wavelength selection techniques for hyperspectral image processing in the food industry. *Food and Bioprocess Technology*, **7**, 307-323.

Liu, Q., Sun, K., Peng, J., Xing, M., Pan, L., & Tu, K. (2018). Identification of Bruise and Fungi Contamination in Strawberries Using Hyperspectral Imaging Technology and Multivariate Analysis. *Food Analytical Methods,* **11**, 1518-1527.

Liu, Y., & Chen, Y. R. (2001). Analysis of visible reflectance spectra of stored, cooked and diseased chicken meats. *Meat Science,* **58**, 395-401.

Lorente, D., Aleixos, N., Gómez-Sanchis, J., Cubero, S., García-Navarrete, O. L., & Blasco, J. (2012). Recent advances and applications of hyperspectral imaging for fruit and vegetable quality assessment. *Food and Bioprocess Technology,* **5**, 1121-1142.

Ma, J., Pu, H., & Sun, D. W. (2018). Predicting intramuscular fat content variations in boiled pork muscles by hyperspectral imaging using a novel spectral pre-processing technique. *LWT-Food Science and Technology,* **94**, 119-128.

Manley, M. (2014). Near-infrared spectroscopy and hyperspectral imaging: non-destructive analysis of biological materials. *Chemical Society Reviews,* **43**, 8200-8214.

Murphy, D. (2011). Plants and their Exploitation by People. In: *Plants, Biotechnology and Agriculture* (pp. 1-20). Oxfordshire, U.K.: CABI.

Ozaki, Y., McClure, W. F., & Christy, A. A. (2006). *Near-Infrared Spectroscopy in Food Science and Technology*. Hoboken, USA: John Wiley & Sons.

Pasquini, C. (2003). Near infrared spectroscopy: fundamentals, practical aspects and analytical applications. *Journal of the Brazilian Chemical Society,* **14**, 198-219.

Pu, H., Kamruzzaman, M., & Sun, D. W. (2015a). Selection of feature wavelengths for developing multispectral imaging systems for quality, safety and authenticity of muscle foods – a review. *Trends in Food Science & Technology,* **45**, 86-104.

Stellenbosch University https://scholar.sun.ac.za

Pu, Y. Y., Feng, Y. Z., & Sun, D. W. (2015b). Recent progress of hyperspectral imaging on quality and safety inspection of fruits and vegetables: a review. *Comprehensive Reviews in Food Science and Food Safety,* **14**, 176-188.

Qiu, Y., Zhu, R., Fan, Z., Yao, X., & Lewis, E. (2018). Comparison of models and visualization of total volatile basic nitrogen content in mutton using hyperspectral imaging and variable selection methods. *Spectroscopy Letters*, 1-10.

Rahman, A., Faqeerzada, M. A., & Cho, B. K. (2018). Hyperspectral imaging for predicting the allicin and soluble solid content of garlic with variable selection algorithms and chemometric models. *Journal of the Science of Food and Agriculture*, **98**, 4715-4725.

Sendin, K., Manley, M., & Williams, P. J. (2018a). Classification of white maize defects with multispectral imaging. *Food Chemistry,* **243**, 311-318.

Sendin, K., Williams, P. J., & Manley, M. (2018b). Near infrared hyperspectral imaging in quality and safety evaluation of cereals. *Critical Reviews in Food Science and Nutrition,* **58**, 575-590.

Sone, I., Olsen, R. L., Sivertsen, A. H., Eilertsen, G., & Heia, K. (2012). Classification of fresh Atlantic salmon (Salmo salar L.) fillets stored under different atmospheres by hyperspectral imaging. *Journal of Food Engineering,* **109**, 482-489.

Su, W.-H., & Sun, D. W. (2016). Facilitated wavelength selection and model development for rapid determination of the purity of organic spelt (Triticum spelta L.) flour using spectral imaging. *Talanta,* **155**, 347-357.

Sun, J., Jiang, S., Mao, H., Wu, X., & Li, Q. (2016). Classification of black beans using visible and near infrared hyperspectral imaging. *International Journal of Food Properties,* **19**, 1687-1695.

Velásquez, L., Cruz-Tirado, J., Siche, R., & Quevedo, R. (2017). An application based on the decision tree to classify the marbling of beef by hyperspectral imaging. *Meat Science,* **133**, 43-50.

Villa, A., Chanussot, J., Jutten, C., Benediktsson, J. A., & Moussaoui, S. (2009). *On the use of ICA for hyperspectral image analysis.* Paper presented at the Geoscience and Remote Sensing Symposium, 2009 IEEE International, IGARSS 2009.

Wallays, C., Missotten, B., De Baerdemaeker, J., & Saeys, W. (2009). Hyperspectral waveband selection for on-line measurement of grain cleanness. *Biosystems Engineering,* **104**, 1-7.

Wang, L., Liu, D., Pu, H., Sun, D. W., Gao, W., & Xiong, Z. (2015a). Use of hyperspectral imaging to discriminate the variety and quality of rice. *Food Analytical Methods,* **8**, 515-523.

Wang, L., Pu, H., Sun, D. W., Liu, D., Wang, Q., & Xiong, Z. (2015b). Application of hyperspectral imaging for prediction of textural properties of maize seeds with different storage periods. *Food Analytical Methods,* **8**, 1535-1545.

Stellenbosch University https://scholar.sun.ac.za

Wang, L., Sun, D. W., Pu, H., & Zhu, Z. (2016). Application of hyperspectral imaging to discriminate the variety of maize seeds. *Food Analytical Methods*, **9**, 225-234.

Wang, W., Li, C., Tollner, E. W., Gitaitis, R. D., & Rains, G. C. (2012). Shortwave infrared hyperspectral imaging for detecting sour skin (*Burkholderia cepacia*)-infected onions. *Journal of Food Engineering*, **109**, 38-48.

Wold, H. (1982). Soft modeling: the basic design and some extensions. In K. G. Joreskog & H. Wold (Eds.), *Systems Under Indirect Observation* (pp. 1-54). Amsterdam, The Netherlands: North-Holland.

Wu, D., & Sun, D. W. (2013a). Application of visible and near infrared hyperspectral imaging for non-invasively measuring distribution of water-holding capacity in salmon flesh. *Talanta*, **116**, 266-

Wu, D., & Sun, D. W. (2013b). Potential of time series-hyperspectral imaging (TS-HSI) for non-invasive determination of microbial spoilage of salmon flesh. *Talanta,* **111**, 39-

Wu, D., Shi, H., Wang, S., He, Y., Bao, Y., & Liu, K. (2012a). Rapid prediction of moisture content of dehydrated prawns using online hyperspectral imaging system. *Analytica Chimica Acta,* **726**, 57-66.

Wu, D., Sun, D. W., & He, Y. (2012b). Application of long-wave near infrared hyperspectral imaging for measurement of color distribution in salmon fillet. *Innovative Food Science & Emerging Technologies,* **16**, 361-372.

Wu, W., Chen, G., Kang, R., Xia, J., Huang, Y., & Chen, K. (2017). Successive Projections Algorithm–Multivariable Linear Regression Classifier for the Detection of Contaminants on Chicken Carcasses in Hyperspectral Images. *Journal of Applied Spectroscopy*, **84**, 535-541.

Xie, C., Li, X., Shao, Y., & He, Y. (2014). Color measurement of tea leaves at different drying periods using hyperspectral imaging technique. *PloS one*, **9**, e113422.

Xiong, Z., Sun, D. W., Pu, H., Zhu, Z., & Luo, M. (2015). Combination of spectra and texture data of hyperspectral imaging for differentiating between free-range and broiler chicken meats. *LWT-Food Science and Technology*, **60**, 649-655.

Yang, Y.-C., Sun, D. W., Pu, H., Wang, N.-N., & Zhu, Z. (2015). Rapid detection of anthocyanin content in lychee pericarp during storage using hyperspectral imaging coupled with model fusion. *Postharvest Biology and Technology,* **103**, 55-65.

Zhang, B., Fan, S., Li, J., Huang, W., Zhao, C., Qian, M., & Zheng, L. (2015a). Detection of early rottenness on apples by using hyperspectral imaging combined with spectral analysis and image processing. *Food Analytical Methods,* **8**, 2075-2086.

Zhang, B., Li, J., Zheng, L., Huang, W., Fan, S., Zhao, C., & Meng, Q. (2015b). Development of a hyperspectral imaging system for the early detection of apple rottenness caused by Penicillium. *Journal of Food Process Engineering,* **38**, 499-509.

Stellenbosch University https://scholar.sun.ac.za

CHAPTER 2: REVIEW OF LITERATURE

Part II: The South African maize industry and its relationship with Fusarium

ABSTRACT

White maize is a major staple food source in South Africa, resulting in countrywide intensive commercial production of the crop. Despite the array modern techniques and resources at a farmer's disposal, ear rots caused by various *Fusarium* species are still widely prevalent. The vast majority of the annual crop is consumed locally, with maize passing through a market value chain of producer, silo owner, trader, miller and end user. As maize is traded within this chain, a fair market price is determined based on the maize consignment's grade. Grading is a visual inspection method based on the assumption that the appearance of grain is related to chemical composition, functionality and optimum end use. This tedious method simply requires a grader to sort a 150 g sample into categories of sound maize and various undesirable materials (e.g. water damaged kernels), and weigh the amounts of each category to assign a grade of WM1 (best), WM2 and WM3. While fungal damaged kernels are included as a category in this visual inspection method, literature has established that various *Fusarium* species can produce harmful mycotoxins called fumonisins without any visual symptoms of the disease. Fumonisin analysis by analytical methods has very recently been added to South African legislation. However, the Southern African Grain Laboratory has included fumonisins in their annual maize crop quality survey regularly for years and regularly report high levels of contamination. With these added requiremtents, there is a need for an automated system which offers more rapid and accurate evaluation of grade, as well as detection of fungal infection and fumonisin risk when visual symptoms are not present. NIR hyperspectral imaging has been successfully used in simpler studies for sorting maize defects and detecting asymptomatic *Fusarium* infected maize, and could be a possible solution.

Stellenbosch University https://scholar.sun.ac.za

INTRODUCTION

Maize (*Zea mays L.*) is the main grain produced and consumed as a staple food in South Africa (Meyer et al., 2019). Both white and yellow maize are grown widely in South Africa, with the production divided roughly as 60% white and 40% yellow maize. About half of the annual crop is consumed directly by humans as a staple food source, and the majority of this is in the form of a traditional white maize porridge. Animal feed constitutes a further 40% (mostly yellow maize), and the remaining 10% is used for seed and industrial uses. This utilisation of maize differs from most developed countries, where maize is grown almost exclusively as a means for producing secondary products, such as meat, eggs and dairy. In contrast, the local demand for maize as a directly consumed staple food is so high that the vast majority of the large annual maize crop is consumed within South Africa. The surplus is exported when available, most commonly to other African nations.

The South African maize industry is well developed, with 98% of maize produced by intensive commercial farming, and the remaining 2% by subsistence farming. Maize production is spread throughout South Africa, with most provinces contributing to the annual yield. The primary maize growing regions are located in the Free State (40%), North-West (22%) and Mpumalanga highveld (21%) (total 83%) (DAFF 2012). Further small contributions come from the Northern Cape (5%), Gauteng (5%), KwaZulu-Natal midlands (4%) and Limpopo (2%). Very little maize is grown in the Western Cape/Karoo (<1%) or Eastern Cape (1%). As the growing regions are spread out geographically, there is a relatively wide window for planting and harvesting. Generally, maize is planted between October (East) and December (West), and harvested between April (East) and June (West).

The average production of maize in South Africa was 12.8 million tons between 2013 and 2016, followed by large fluctuations in production in recent years. A severe drought caused by the El Niño event had disastrous effects on the 2016 harvest, where only 7.8 million tons were produced. Consequently, 4 million tons of maize were imported into South Africa, which was highly unusual, and affected the price and supply of both human staple food and animal feed. The years following the drought have shown a strong recovery, with 2017 and 2018 returning to bumper yields of 17.8 and 13.5 million tons, respectively, and 12 to 13 million tons forecast for 2019.

MAIZE MARKET VALUE CHAIN

Maize moves through a market value chain from farm to table. This chain can be broadly divided into five tears, namely producers of maize (i.e. farmers); silo owners, who store maize for their own account and on behalf of others; traders, who market and sell maize; millers, who convert maize into usable form; and the end user.

During farming, a huge variety of factors can influence the quality and, in turn, the market value of a maize crop. Managing with these factors is arguably the biggest challenge to a farmer. The farmer's primary goal is to produce large amounts of healthy maize kernels which are intact and free from damage by biotic (insects, rodents and fungi) and abiotic factors (water, sun and frost). While the effects of climatic uncertainty are largely out of human control, crop losses caused by physical damage or disease can often be avoided to some extent. Appropriate farming practices can be implemented, such as planting an appropriate maize hybrid.

Stellenbosch University https://scholar.sun.ac.za

A well-chosen maize hybrid can improve a farmer's productivity and help ensure high yield. Hybrids differ in their resistance and susceptibility to many factors, such as temperature, water availability, nutrient levels, pests and disease-causing microbes. Invariably, a single hybrid cannot be the perfect solution, and a farmer must consider which factors are most important in the given farming environment. In fact, it has been suggested that commercial South African maize often has high mycotoxin contamination levels as a result of fungal diseases because commercial farmers still consider yield, not disease resistance, the number one criterion when choosing a hybrid (Beukes et al., 2017). Crop rotation, plant population control, correct harvesting and storage practices are further practices aiding in disease and pest control. Farmers are also advised to adhere to Good Agricultural Practice. This collective set of international codes proposed by the United Nation's Food and Agricultural Organisation (FAO) are intended for on-farm and post-production processes to ensure a safe food supply (Magan & Aldred, 2004). These codes outline all aspects of production, such as food quality, food safety, environmental sustainability and economics. Adherence to these codes of good practice does not only impact on food safety locally, but also influences international trade (Beukes et al., 2017). These codes can play a vital role in planning an integrated pre- and post-harvest pest and disease management strategy.

Following harvest, maize is generally stored for a variable time period before being processed. The farmer has the four storage options: avoid storage completely by delivering the crop straight to a miller; make use of silo bags, a non-traditional storage method; erect his own silos; or make use of commercial silos off-farm. The latter option is the most popular, with about 94% of silos being operated commercially. The popularity of commercial maize storage is largely due to silo owners providing facilities to handle the crops, store maize safely, and supply it to buyers on a continuous basis throughout the year.

Moving a farmer's maize crop to domestic or international market requires a trader. Furthermore, during shortages such as the 2016 drought, traders will source maize externally. The basic function of a trader is to take positions (forward buying and selling), assume risk, establish value and provide the real cash market for maize and other grain.

Once acquired for processing, the grain must be broken down into a consumable form. Maize will often go through a milling process, namely dry or wet milling. Dry milling is used to produce maize meal, the most common staple food consumed in South Africa. Specific dry milling products include the various grades of maize meal, unsifted, sifted, coarse, super and special maize meal, as well as samp, maize grits and maize rice. Wet milling is an alternative milling process, most importantly used to produce pure starch. This process involves steeping the maize for about 36 hours, which softens the kernel and allows separation of the husk, starch, protein and germ. After milling, the maize is ready for consumption by the end consumer.

GRADING

Grading is a process implemented to facilitate fair commercialisation of maize, and may be conducted at any point between farmer, silo owner, trader and miller. The intrinsic value of a maize consignment is estimated, which determines a fair price for marketing between buyers and sellers. The grading process also provides valuable information to the buyer related to quality for further storage and processing.

Stellenbosch University https://scholar.sun.ac.za

South African maize is currently graded using visual inspection methods only. The basis of the method is the assumption that the appearance of grain is related to chemical composition, functionality and optimum end use (Serna-Saldivar, 2010). A grader measures a working sample between 150 g (minimum) and 200 g from the bulk maize consignment. The sample is spread out on a table top and the grader visually inspects each kernel for broken kernels, damaged kernels and foreign matter. Broken and damaged maize will have different water absorbing properties, leading to less uniform cooking characteristics and final product consistency, while pest and fungal damage can affect the palatability, sanitation and shelf life of the resulting products. Furthermore, mycotoxins originating from fungal contamination could cause sickness or death if consumed (Yoshizawa et al., 1994; Sydenham et al., 1990). The sound maize and various types of undesirable materials are separated into piles and weighed at the end of the inspection process. The grade of the maize consignment is assigned solely on the weight of these undesirable materials within the sample, based on South African grading regulations stipulated in the Agricultural Product Standards Act (Act No. 119 of 1990). There are three white maize classes, WM1 (best), WM2 and WM3.

The types of undesirable materials detailed in the South African legislation fall under four broad categories, namely defective maize, other colour maize, pinked maize and foreign matter. Within these main categories are sub-categories. Defective maize kernels has a large number of sub-categories, but the most commonly occurring in South Africa include heat damage, water damage, screenings/broken kernels, frost damage, immature kernels, sprouted kernels, pest damage and fungal damage. Some of these defects not only affect the quality characteristics of the maize, but also pose potential safety risks (e.g. mycotoxin contamination of fungal damaged kernels), and content is limited to a maximum of 7% for WM1. The other colour maize category includes only yellow maize, as only white and yellow maize are grown commercially in South Africa. Yellow maize can cause overall discolouration in white maize products, and thus levels are limited to 3% for WM1. The pinked maize category includes only pink discoloured white maize. This a defect is a superficial light pink discolouration on the exterior of white maize kernels, and some hybrids are more prone than others. It poses no safety threat and does not cause severe colour changes, and is thus leniently restricted (20% for WM1). Lastly, foreign matter is divided into two main categories. Foreign materials that pose a safety risk, such as glass, stone, coal, dung or metal, must be completely absent in all grades. These materials are removed during a preliminary dockage sorting step and are very unlikely to be found in the grading room. Less dangerous foreign materials, for example other cereal commodities (wheat, soy, sunflower seeds and sorghum) or maize plant materials, are allowed within the given limits (0.3% for WM1).

An analytical technique considered for the automation maize grading must be capable of accurately evaluating these four categories of undesirable materials. These materials are diverse and, if spectral imaging is to be considered, must be separated from sound maize and one another based on spectral differences. Two preliminary studies have demonstrated the capability of spectral imaging in separating sound maize from the abovementioned sub-categories individually, using both NIR hyperspectral imaging (Sendin et al., 2019) and VNIR multispectral imaging (Sendin et al., 2018). Two-way PLS-DA analyses of sound maize vs. one undesirable material (e.g. heat damage or *Fusarium* fungal damage) demonstrated the technique's ability to

Stellenbosch University https://scholar.sun.ac.za

distinguish a healthy maize kernel and an undesirable one, with classification accuracies of 98 – 100% achieved by NIR hyperspectral imaging and 83 – 100% for VNIR multispectral imaging. However, these studies did not compare the undesirable material classes to one another, nor were multiple classes compared simultaneously. During current maize grading, a human grader is expected to detect an undesirable material of any class among the healthy kernel at any given time (i.e. not only looking for heat damaged kernels during inspection), and must correctly determine the class of the undesirable kernel to apply the correct legal limits, which vary per category. Thus, these studies were a far cry from the capabilities of a human grader. While spectral imaging's ability to perform two-way classification was demonstrated, an automated system must be able to distinguish all classes simultaneously (multiple class classification).

FUSARIUM INFECTION, SYMTOMS AND MYCOTOXINS

Maize is widely prone to ear rots caused by various *Fusarium* species, not only resulting in reduced yield and poor quality, but also safety concerns (Stumpf et al., 2013). Most *Fusarium* species produce one or more toxic secondary metabolites, commonly known as mycotoxins (Beukes et al., 2017). The two distinct maize ear rot diseases caused by *Fusarium* species in South Africa are Fusarium ear rot (pink ear rot), caused primarily by *F. verticillioides*, and Gibberella ear rot (red ear rot), caused by the *Fusarium graminearum* species complex (Munkvold, 2003). Fusarium ear rot is most prevalent in the warmer dry areas, while Gibberella predominates in intermediate climate areas (Beukes et al., 2017). Both diseases are associated with the production of harmful mycotoxins, with fumonisins and deoxynivalenol (DON) being of highest concern for *F. verticillioides* and *Fusarium graminearum* species complex, respectively. Since 2004, the only mycotoxin legally regulated in South Africa was aflatoxin B_1. For decades, the risk of *Fusarium* related mycotoxins has been simply assessed according to the amount of *Fusarium* damaged kernels were present in a sample according to the abovementioned white maize grading regulations (Act No. 119 of 1990). The South African authorities have recently recognised this shortfall, and published an amendment in 2016 regarding white maize due for further processing. Limits for safe human consumption were set at 4 ppm for fumonisins and 2 ppm for DON. However, the maize industry has been resistant to these changes in the short time since the legislative change. Due to the high cost and inconvenience of mycotoxin testing, such as using liquid chromatography with mass spectrometry (LC-MS), testing is often conducted as minimally as possible. The manual visual inspection method for grading is frequently still used as the main measure of *Fusarium* risk.

Fusarium and Gibberella ear rot infections can exhibit as both symptomatic (rotting) and asymptomatic (healthy appearing) kernels when the fungus is present within the kernel. In fact, the majority of infected maize kernels show no visible signs of fungal growth or rotting, but mycotoxins will be produced within the kernel under appropriate conditions. The ability of *Fusarium* to grow within a maize kernel and produce mycotoxins without presenting any visible symptoms is due to a property known as intercellular endophytism or latent infection (Kuldau & Yates, 2000). This may include a brief asymptomatic phase followed by symptomatic infection, or completely asymptomatic infection. The dual nature of *Fusarium* sp. as both a pathogen and a symptomless endophyte indicates a complex relationship with maize, although many aspects are still largely

Stellenbosch University https://scholar.sun.ac.za

unknown. It is thought to be related to specialised or mutualistic interactions between the plant and the endophyte, as the maize and *Fusarium* can maintain a very balanced association under favourable conditions. However, this balance is no longer maintained under extreme drought or other undesirable conditions, resulting in degrees of pathological responses, including fumonisin production. It was long thought that fumonisins were synthesised by *F. verticillioides* only in late plant development, or during the saprophytic stage (i.e. rotting) (Bacon et al., 2008). However, it has been demonstrated that synthesis can occur in earlier development and that accumulation of fumonisins by the symptomless endophytic state is favoured by drought (Bacon et al., 2001). Thus, the fumonisins are produced in the biotrophic/endophytic, pathogenic and saprophytic states.

A study conducted in Brazil during the 2008/09 and 2009/10 growing seasons investigated the links between *Fusarium* infection, visible ear rot symptoms and mycotoxin levels across 23 regions (Stumpf et al., 2013). Across the study's 29 bulk samples, the mean number of visibly symptomatic kernels was 7%, despite a mean *F. verticillioides* infection rate of 58%. Thus, the vast majority of the infected kernels were asymptomatic. In fact, some samples with 100% infected kernels did not contain a single symptomatic kernel. The *Fusarium graminearum* species complex infection rate was relatively low (0 – 6%). The kernels were tested for mycotoxins, revealing levels of 0.57 to 20.38 ppm for asymptomatic kernels and 68.98 to 336.38 ppm for symptomatic kernels. This study highlights the ability of *Fusarium* species to colonise the plant systemically and invade grains without causing symptoms, and clearly demonstrates the lack of correlation between visible symptoms and both *Fusarium* infection and mycotoxin levels.

While a similar academic study on asymptomatic infections has not been conducted on commercial South African maize, it is widely accepted that *Fusarium* species are ubiquitous throughout the growing regions and infections are commonly occurring. The Southern African Grain Laboratory (SAGL) publishes an annual maize crop quality survey with the financial support of The Maize Trust. When climatic and other conditions are favourable for fungal infection and development, high levels of mycotoxin contamination have been reported, despite the general high quality of South African commercial maize (SAGL, 2013). Researchers associated with the SAGL have recently published a peer-reviewed article on the prevalence of mycotoxins in commercial South African maize samples (Meyer et al., 2019). The study investigated a LC-MS/MS method to monitor the levels of 13 mycotoxins, including fumonisins. A comprehensive group of 1400 maize samples spanning four consecutive harvest seasons (2013/14 – 2016/17) and all commercial maize production areas were used. Levels of fumonisins and DON above 4 ppm and 2 ppm, respectively, were reported for all four seasons in numerous regions. Over the four season period, 43.6 to 61.5% of the white maize samples contained fumonisins. The highest level recorded was 6.9 ppm in white maize and 11.3 ppm in yellow maize. Similarly, 25.6 to 73.9% of the samples contained DON over the study period. Unsafe levels up to 16.0 ppm DON were found in white maize samples from numerous growing regions. This study confirmed the importance of mycotoxin analysis in the maize market value chain and emphasised that grain handlers should know the mycotoxin status of their stocks.

Based on evidence from the Stumpf et al. (2013) study, the visual inspection method that the industry currently relies on to identify *Fusarium* species contamination does not prevent mycotoxins from entering the

Stellenbosch University https://scholar.sun.ac.za

food chain. Furthermore, the SAGL reports and Meyer et al. (2019) study confirm that fumonisins and DON are present in commercial South African maize. Instead of relying on human vision to identify fungal infection based on visible symptoms, an analytical technique could be used. Fungal infection, whether visible or not, must always be present for mycotoxin production to take place, and thus should give a reliable indication of mycotoxin risk. Providing maize and maize product producers with a tool to flag consignments with increased mycotoxin risks could facilitate smoother implementation of the 2016 legislative changes for fumonisin and DON testing.

Hyperspectral imaging studies of fungal maize pathogens have investigated the ability of the technique to detect fungal infection. Williams et al. (2012) detected *F. verticillioides* infection of artificially inoculated maize kernels prior to the appearance of visual symptoms using NIR hyperspectral imaging. The technique can detect the infection without visible mould growth as it detects the changes in chemical composition due to kernel constituents being depleted during fungal proliferation, and not the fungal growth itself. However, as *Fusarium* infection is often not due to inoculum placed on the surface of a harvested maize kernel, this study does not truly represent naturally occurring asymptomatic maize kernels.

Fusarium ear rot

Fusarium ear rot is primarily caused by *F. verticillioides*, but *F. subglutinans* and *F. proliferatum* are also important (Munkvold, 2003a). In addition to ear rot, these organisms can also cause root and stalk rot. *F. verticillioides* is considered ubiquitous in most maize growing regions globally and can be found in plant residues in almost every maize field at harvest (Ncube et al., 2011; Oren et al., 2003). The symptoms of Fusarium ear rot can vary widely in appearance from asymptomatic infection to severe rotting of all plant parts (Munkvold et al., 1997). It has been found that diseased and asymptomatic plants occur in the same field planted with a genetically uniform maize hybrid (Oren et al. 2003). Visual symptoms depend on the maize genotype, environment and the extent of the disease severity, but generally present as a white-pink cottony mould. Individual infected kernels or groups thereof are usually scattered randomly on the entire ear and, in severe cases, the entire ear may be whitish on and between kernels. When inspecting harvested kernels, infected kernels can also be identified by white streaking that appear as ‘starbursts’ on the surface (Munkvold & Desjardins, 1997). Climatic conditions play a major role in the severity of Fusarium ear rot symptoms, as well as in mycotoxin production (Stumpf et al., 2013). Symptoms are often most severe in hot and dry conditions, such as those prevailing primarily in the North-Western parts of the South African maize-producing areas, particularly when these conditions occur after flowering.

F. verticillioides has both a saprophytic stage and pathogenic stage, meaning that it survives within the soil on remnants of plant material over winter (saprophyte) and invades new plants during the growing season (pathogen) (Pereyra & Lori 2013). Due to this effective lifecycle, the fungus is pervasive and has little competition from other fungi and bacteria. Infection of maize can happen at any stage of plant development by air, soil or insects. The most commonly reported method of infection is via airborne spores (Oren et al., 2003). Munkvold et al. (1997) established that while other pathways exist, local infection via silks is the main pathway

Stellenbosch University https://scholar.sun.ac.za

of infection. After invasion of the silks, the fungus moves from the tip of the ear downward. Alternatively, spores may infect weak points on plant tissues, such as stress cracks in the pericarp and through the pedicel, and wounds caused by hail, insects or birds. Soil infections occur by inoculation from contaminated debris (e.g. maize stubble from previous season) in the soil. After planting, a healthy seed can become infected during germination, where seed infection levels of up to 100% have been recorded in contaminated fields. The fungus develops inside the young plant, moving from the roots to the stalk, cob and finally kernels (Oren et al., 2003). Lastly, the feeding activities of lepidopterous insects spread spores to silks, kernels, stems and feeding channels (Munkvold et al., 1997). The most prevalent species in South Africa are *Chilo partellus* and *Busseola fusca*, that feed on infected tissue, move to new plants or plant parts and spread the fungal spores. As the fungus is capable of asymptomatic infection, only a small percentage of the infected kernels become symptomatic following infection (Munkvold et al., 1997).

F. verticillioides produce mycotoxins called fumonisins, known to cause oesophageal cancer in humans and a variety of conditions in animals, including leukoencephalomalacia in horses and pulmonary oedema in pigs (Beukes et al., 2017; Marasas, 1995). The major fumonisin of concern is fumonisin B1 (FB_1), which often occurs naturally with FB_2 and FB_3. Fumonisin synthesis is largely affected by factors such as the condition and maturity of the maize tissue, temperature and water activity. Maize production regions with warm (20 – 30 °C) and humid conditions during the grain filling stage tend to experience higher fumonisin levels than temperate regions (Janse van Rensburg, 2013; Munkvold, 2003a). It has also been indicated that while low temperatures and water stress reduce the development of visible *F. verticillioides* symptoms, water stress can increase FUM1 gene expression, the first step in fumonisin synthesis (Jurado et al., 2008). It is also evident that high plant populations exhibit a significant increase in fumonisin risk in maize grain. To avoid post-harvest fumonisin production, moisture levels must be below 16%, and stored grain should be aerated regularly to further lower moisture content and temperature.

Controlling *F. verticillioides* infection is extremely challenging, and farmers can implement a variety of prevention strategies with varying efficacy. Due to common occurrence of *F. verticillioides*, the use of sanitation practices has not been very successful in disease reduction, and no fungicides have been registered for the control of ear rots in South Africa (Beukes et al., 2017). Furthermore, as ears are covered by tight husks, contact between the fungicide and the ear rot pathogens is restricted. The use of appropriate maize hybrids is the most economical and environmentally safe Fusarium ear rot preventative measure (Beukes et al., 2017; Munkvold et al., 1997). Due to the spread by insect activity and via insect damaged tissues, genetically modified hybrids that contain the insecticidal proteins for the control of maize stalk borer have been used. Bt-transformed maize contains genes from *Bacillus thuringiensis* encoding for the insecticidal δ-endotoxin CryIA(b), and have significantly less Fusarium ear rot symptoms compared to non-Bt isohybrids. Hybrids adapted to local climatic conditions and hybrids with tight husks have also been found to have lower incidence of the disease. A farmer can also adjust his practices to reduce plant stress and susceptibility, such as avoiding high density plant populations, maintaining adequate levels of nitrogen and other essential growth nutrients, crop rotation of maize with non-graminaceous crops, and subsoiling in compacted soils (Munkvold, 2003; Stumpf et al., 2013).

Stellenbosch University https://scholar.sun.ac.za

Furthermore, *Fusarium* species produce mycotoxins as a way to overcome stressful conditions, and thus minimising plant stress can reduce mycotoxin production after infection has taken place (Munkvold, 2003b; Picot et al., 2010).

Graminearum ear rot

Another prevalent *Fusarium* species related disease is Graminearum ear rot, also referred to as Gibberella ear rot. The disease can also affect crown, root and stalk tissues. Prior to 2000, it was thought that *F. graminearum* (*Gibberella zeae*) was a single species found worldwide, but it was later found to be 16 fungal species belonging to the *Fusarium graminearum* species complex (Van der Lee et al., 2015). The complex has host, climatic and regional preferences, and only five species have been found on South African maize thus far (*F. boothii*, *F. asiaticum*, *F. austroamericanum*, *F. meridionale* and *F. graminearum sensu stricto)*. The primary pathogen causing ear rot in South Africa is *F. boothii* (Beukes et al., 2018),

Similarly to *F. verticillioides*, *F. graminearum* species complex can overwinter as saprophytes on a variety of organic matter and infect the next season's crop. The primary mode of infection is via acrospores dispersed by wind or rain (Dragich and Nelson, 2014). Spores most commonly infect maize silks and grow down into the point of the ear (Logrieco et al., 2013). The fungus is known to establish itself inside the plant before killing tissue and developing visible symptoms. Disease initially appears as a white mycelium growth turns pink/red with disease progression, spreading from the silk, to the tip and down towards the base (Mesterhazy et al., 2012). Symptoms are favoured by wet, moderate weather within three weeks of silking. Specifically, ideal conditions are temperatures of 25°C to 28°C with a high humidity, commonly occurring under irrigation conditions (Doohan et al., 2003). South African regions affected by sporadic and localised outbreaks are generally KwaZulu-Natal and Mpumalanga, and irrigation fields in the Limpopo and North West Province.

A major concern of *F. graminearum* species complex is toxicity due to three important mycotoxins, deoxynivalenol (DON), nivalenol (NIV) and zearalenone (ZEA) (Logrieco et al., 2013). While general opinion used to be that mycotoxins are only found in infected tissue, it has recently been shown that DON can be transported from infected stalk tissue to the grain in wheat plants (Beccari et al., 2018). Simply put, this study suggests that a kernel with no disease symptoms could contain mycotoxins produced elsewhere in the same plant. These mycotoxins are known to cause a wide variety of human health issues (anaemia, skin lesions, vomiting, diarrhoea and liver damage). DON, also known as vomitoxin because of its strong emetic effects, causes feed refusal, vomiting, decreased weight gain and less effective feed utilisation in pigs (Beukes et al., 2017). Cows are much more resistant, while chickens are not affected, however all species may refuse feed due to the unpalatability. Maize with more than 5% infected kernels should not be used for feed, especially pigs, but may be diluted to appropriate levels with first grade maize. NIV is considered more toxigenic, and causes feed refusal, lower feed conversion efficacy and decreased liver weights in chickens (Beukes, et al., 2017). ZEA is considered the least toxigenic of the three, but has been linked to breast cancer in humans and reproductive issues in livestock and poultry.

Stellenbosch University https://scholar.sun.ac.za

Unlike *F. verticillioides*, no resistance by a South African maize hybrid has been clearly shown, and *F. graminearum* species complex susceptibility varies widely among the available hybrids. As the major source of inoculum is the previous year's plant debris, stubble removal is important to prevent saprophytic survival and reduce disease incidence in the following crop season (Beukes et al., 2017). Crop rotation with non-graminaceous crops can be effective, however *F. graminearum* species complex may survive on residues from other crops, grasses and weeds (Champeil et al., 2004). Non-hosts include legumes, cotton and sunflower. Good farming practices, including appropriate population density, adequate essential growth nutrient levels and subsoiling, reduce disease incidence.

CONCLUSION

Maize is the most widely grown crop in South Africa. Due to its large-scale production, the vast majority of maize is produced in a formalised commercial system. The maize market value chain directs maize from the primary producers through storage, trading, milling and end user consumption. The value of grain is dependent on both the quality of the particular consignment, as well as the general supply and demand at that time. While farmers have little control over the general market, they can endeavour to ensure the quality of their maize crop. Primary production is complex and is reliant on a wide variety of biotic and abiotic factors. Farmers have strategies at their disposal to limit the effects of these factors, which can infer high labour and material costs. Fair marketing of maize is ensured by grading maize, which assigns a grade based on the quality and safety of a maize consignment. However, the current visual inspection methods are problematic. Most alarmingly, academic studies and the SAGL's annual maize quality report suggest that maize containing high levels of mycotoxins are entering the food chain, as visual inspection is not sufficient to detect mycotoxin contamination. An automated analytical technique for maize grading could ensure more accurate and rapid maize grading. This technique must be able to detect sound maize and multiple categories of undesirable materials simultaneously. The potential of detecting asymptomatic fungal infection would also be valuable for the South African maize industry. NIR hyperspectral imaging could satisfy both of these requirements and shows promise for the development of a spectral imaging maize grading system.

REFERENCES

Bacon, C. W., Glenn, A. & Yates, I. E. (2008). Fusarium verticillioides: managing the endophytic association with maize for reduced fumonisins accumulation. *Toxin Reviews,* **27,** 411-446.

Bacon, C. W., Yates, I. E., Hinton, D. M. & Meredith, F. (2001). Biological control of Fusarium moniliforme in maize. *Environmental Health Perspectives,* **109,** 325-332.

Beccari, G., Prodi, A., Pisi, A., Nipoti, P., Onofri, A., Nicholson, P., Pfohl, K., Karlovsky, P., Gardiner, D.M. & Covarelli, L. (2018). Development of three fusarium crown rot causal agents and systemic translocation of deoxynivalenol following stem base infection of soft wheat. *Plant Pathology*, **67**, 1055-1065.

Stellenbosch University https://scholar.sun.ac.za

Beukes, I., Rose, L. J., van Coller, G. J., & Viljoen, A. (2018). Disease development and mycotoxin production by the Fusarium graminearum species complex associated with South African maize and wheat. *European Journal of Plant Pathology*, **150**, 893-910.

Champeil, A., Doré, T., & Fourbet, J.-F. (2004). Fusarium head blight: epidemiological origin of the effects of cultural practices on head blight attacks and the production of mycotoxins by Fusarium in wheat grains. *Plant Science,* **166**, 1389-1415.

Doohan, F., Brennan, J., & Cooke, B. (2003). Influence of climatic factors on Fusarium species pathogenic to cereals. *Epidemiology of Mycotoxin Producing Fungi,* **109**, 755-768.

Dragich, M., & Nelson, S. (2014). Gibberella and Fusarium Ear Rots of Maize in Hawaii. *Plant Dieases,* **102**, 1-8.

Eriksen, G. S., & Alexander, J. (1998). Fusarium Toxins in Cereals: A Risk Assessment Biology of Fusarium Fungi. Copenhagen, Denmark: Nordic Council of Ministers.

Janse van Rensburg, B. (2013). How to manage Fusarium ear rot and fumonisin production. Grain SA. Retrieved from https://www.grainsa.co.za/how-to-manage-fusarium-ear-rot-and-fumonisin-production

Jurado, M., Marín, P., Magan, N., & González-Jaén, M. T. (2008). Relationship between solute and matric potential stress, temperature, growth, and FUM1 gene expression in two Fusarium verticillioides strains from Spain. *Applied Environmental Microbiology*, **74**, 2032-2036.

Kuldau, G. A. & Yates, I. E. (2000). Microbial endophytes. In: *Evidence for Fusarium Endophytes in Cultivated and Wild Plants* (edited by Bacon, C. W. & White, J.). Pp. 85-120. New York City, USA: CRC press.

Logrieco, A., Mullè, G., Moretti, A., & Bottalico, A. (2013). Toxigenic Fusarium speciesand mycotoxins associated with maize ear rot in Europe. In A. Logrieco, J. A. Bailey, L. Corazza, & B. M. Cooke (Eds.), Mycotoxins in Plant Disease (pp. 597-609). Dordrecht, Netherlands: Springer.

Magan, N., & Aldred, D. (2004). The use of HACCP in the control of mycotoxins: the case of cereals. In N. Magan & M. Olsen (Eds.), Mycotoxins in food: detection and control (pp. 139-189). Cambride, UK: Woodhead Publishing.

Marasas, W. F. O. (1995). Fumonisins: their implications for human and animal health. *Natural Toxins*, **3**, 193-198.

Meyer, H., Skhosana, Z. D., Motlanthe, M., Louw, W. & Rohwer, E. (2019). Long Term Monitoring (2014–2018) of Multi-Mycotoxins in South African Commercial Maize and Wheat with a Locally Developed and Validated LC-MS/MS Method. *Toxins,* **11,** 271.

Munkvold, G. P. (2003a). Epidemiology of Fusarium diseases and their mycotoxins in maize ears. *European Journal of Plant Pathology,* **109**, 705-713.

Stellenbosch University https://scholar.sun.ac.za

Munkvold, G. P. (2003). Cultural and genetic approaches to managing mycotoxins in maize. *Annual Review of Phytopathology,* **41**, 99-116.

Munkvold, G. P., & Desjardins, A. E. (1997). Fumonisins in maize: can we reduce their occurrence? *Plant Disease,* **81**, 556-565.

Munkvold, G. P., Hellmich, R. L., & Showers, W. (1997). Reduced Fusarium ear rot and symptomless infection in kernels of maize genetically engineered for European corn borer resistance. *Phytopathology*, **87**, 1071-1077.

Ncube, E., Flett, B. C., Waalwijk, C., & Viljoen, A. (2011). Fusarium spp. and levels of fumonisins in maize produced by subsistence farmers in South Africa. *South African Journal of Science*, **107**, 1-7.

Oren, L., Ezrati, S., Cohen, D., & Sharon, A. (2003). Early events in the Fusarium verticillioides-maize interaction characterized by using a green fluorescent protein-expressing transgenic isolate. *Applied Environmental Microbiology*, **69**, 1695-1701.

Pereyra, S., & Lori, G. A. (2013). Epidemiology. In T. M. A. Magliano & S. N. Chulze (Eds.), *Fusarium head blight in Latin America* (pp. 143-156). Dordrecht, Netherlands: Springer.

Picot, A., Barreau, C., Pinson-Gadais, L., Caron, D., Lannou, C., & Richard-Forget, F. (2010). Factors of the Fusarium verticillioides-maize environment modulating fumonisin production. *Critical Reviews in Microbiology,* **36**, 221-231.

Sendin, K., Manley, M., Baeten, V., Pierna, J. A. F. & Williams, P. J. (2019). Near Infrared Hyperspectral Imaging for White Maize Classification According to Grading Regulations. *Food Analytical Methods,* **12,** 1612-1624.

Sendin, K., Manley, M., & Williams, P. J. (2018). Classification of white maize defects with multispectral imaging. *Food Chemistry*, **243**, 311-318.

South African Grain Laboratory. South African maize crop quality report 2012/2013 [document on the Internet]. c2013 [cited 17 March 2019]. Available from: http://www.sagl.co.za/Portals/0/Maize%20Crop%202012%202013/Maize%20Crop%20Quality%20Report%202012%202013.pdf

Stumpf, R., Santos, J. d., Gomes, L. B., Silva, C., Tessmann, D. J., Ferreira, F., Machinski Junior, M. & Del Ponte, E. M. (2013). Fusarium species and fumonisins associated with maize kernels produced in Rio Grande do Sul State for the 2008/09 and 2009/10 growing seasons. *Brazilian Journal of Microbiology,* **44,** 89-95.

Van der Lee, T., Zhang, H., van Diepeningen, A., & Waalwijk, C. (2015). Biogeography of Fusarium graminearum species complex and chemotypes: a review. *Food Additives & Contaminants: Part A*, **32**, 453-460.

Stellenbosch University https://scholar.sun.ac.za

Williams, P. J., Geladi, P., Britz, T. J., & Manley, M. (2012). Investigation of fungal development in maize kernels using NIR hyperspectral imaging and multivariate data analysis. *Journal of Cereal Science,* **55**, 272-278.

Stellenbosch University https://scholar.sun.ac.za

CHAPTER 3:

HEIRARCHICAL CLASSIFICATION PATHWAY FOR WHITE MAIZE, DEFECTS AND FOREIGN MATERIALS

ABSTRACT

Near infrared hyperspectral imaging was investigated as an alternative to manual inspection for simultaneously separating sound white maize kernels from 16 classes of common undesirable material types. South African maize grading legislation determines grade according to levels of each main category of undesirable material in a sample. Some main categories (e.g. defective maize) have sub-categories (e.g. heat damage and water damage) which human graders can visually distinguish. The hierarchical assembly of 24 partial least squares discriminant analysis (PLS-DA) classification models was used to separate the large number of classes. A group of 12 classes of maize was first separated from a group of 5 classes of foreign materials, and these were classified further. The closely related maize classes were most challenging. The most distinguishable class was separated from the rest first, working towards the most difficult to separate class. The foreign materials were easily classified and were first divided into cellulose-rich (plant material and sunflower seeds) and starchy (sorghum, soy and wheat) groups. A two- and three-way PLS-DA model was used to separate the individual classes in the two groups, respectively. The main category classification accuracy ranged 75 to 100% (93% average). While many of the defects (sub-categories) were misclassified for other classes in the same main category, this was often due to the onset of multiple defects in a single kernel. These errors were not of much concern, nor do they affect the grade according to current legislation. Variable in projection (VIP) scores were calculated and important wavebands were found to be 969 (associated with water), 1149 (fat), 1334 (fat), 1405 (starch), 1563 (protein), 1672 (fat), 1901 (starch), 2032 (protein), 2245 (protein), 2305 (fat or protein) and 2473 nm (starch). While this study demonstrated the capability of hyperspectral imaging to perform the complicated task of separating numerous maize grading classes, the classification accuracies should be further improved. Optimal waveband selection is recommended to remove redundant spectral information and improve model performance.

Stellenbosch University https://scholar.sun.ac.za

INTRODUCTION

Maize grading is conducted throughout the market value chain as maize is traded between the farmer, storage provider and miller. Grading ensures a fair market price per consignment and is based on the basic condition of the maize. A grader manually sorts a 150 g (minimum) sample of the consignment into piles of grading main categories, including healthy (sound) white maize kernels, defective kernels, yellow maize kernels, pinked kernels and foreign materials (Department of Agriculture, 2009). Some of the main categories consist of sub-categories. For example, the defective maize main category include nine sub-categories such as broken kernels or water damaged kernels. The grader does not have to separate the maize beyond the main categories but is trained to be able to distinguish all sub-categories when required (e.g. identifying specific types of fungal damage during mycotoxin audits). The manual inspection step is laborious and challenging, as these working samples contain *ca.* 1000 maize kernels. To increase throughput and decrease the error associated with this process, the industry is seeking an appropriate analytical method to replace manual inspection.

A previous study (Sendin et al., 2019) demonstrated the potential of using hyperspectral imaging for sorting maize grading classes. In this proof of concept study, sound maize was differentiated from one grading defect class at a time based on NIR hyperspectral images. This resulted in 13 two-way PLS-DA models, one for each type of undesirable material. The overall classification accuracy achieved across the 804 kernels/objects in the study was 99.4%. However, this study did not offer a single system for evaluating all the classes simultaneously. While achieving separations of two classes is relatively easy, separating multiple classes is much more challenging. The previous study did not yet offer an alternative to the maize industry, as a human grader can evaluate all classes simultaneously. However, the promising results have encouraged further work to bring the goal of automated maize grading to fruition.

Hierarchical or decision pathway modelling is a potential solution for multi-class classification (Myles & Brown, 2004). Many studies with two, three or even four classes utilise a single globally optimised model to discriminate all classes. This approach is easily and widely accessible to perform, but one critical assumption must be satisfied. All classes must be fully separable using the chosen set of spectral features. This assumption is often not fulfilled, especially when dealing with heterogenous samples and closely related classes, as was observed in the PLS-DA scores plots in Sendin et al. (2019). Instead of calibrating a multi-class classification (e.g. 13-way PLS-DA model for the abovementioned study), hierarchical modelling decomposes the problem into simpler binary classification steps (two- or three-way PLS-DA models) that are reassembled into a single hierarchical structure. To minimise the effects of error propagation through the successive steps of the decision pathway, the pathway must be carefully selected. A prudent approach is to handle the most easily classified groups first and work towards the most challenging (Arnalds et al., 2004). This ensures fewer errors in the earlier steps that would be magnified if carried down the pathway.

Hierarchical approaches have been successfully applied to a wide variety of datasets and problems, although its application can be considered infrequent. A hierarchical pathway was developed for detection of bovine spongiform encephalopathy (BSE) in cattle blood samples using infrared spectroscopic data, where classification was divided into eight binary subproblems (Menze et al., 2007). However, there were only two

Stellenbosch University https://scholar.sun.ac.za

classes and the eight steps were used to accurately classify the presence of the disease based on various parameters, achieving a sensitivity and specificity of 92 and 95%, respectively. A hierarchical tree was also developed for predicting the source of neuronal activity causing a functional magnetic resonance imaging (fMRI) signal on a brain scan (Salimi-Khorshidi et al., 2014). Hierarchical modeling has also been applied to food and agricultural products. The content of five main fatty acids and six main triacylglycerols in olive oils was predicted using PLS regression and six regions of origin using PLS-DA, based on NIR and MIR spectroscopic data (Dupuy et al., 2010). The model was deemed sufficiently accurate for quality control use. Five types of meat have also been separated in binary steps using a hierarchical decision pathway based on NIR spectra (Arnalds et al., 2004). The classes were separated by either LDA or SIMCA models for white or red meat (Level 1), poultry or pork for samples classified as white meat (Level 2) and beef or lamb for red meat (Level 2) and finally, chicken or turkey for poultry (Level 3). A 98% classification accuracy was achieved. This structure is most similar to the challenge of maize grading, where the main categories would be classified first, and each main category would be separated further according to its specific sub-categories. In other words, the result of the previous step guides the analysis in following step and determines which branch of the decision tree is taken. It must be noted, however, meat samples of different species are not as closely related as classes of white maize (single species). To date, little hierarchical pathway research has been published regarding multi-class problems in NIR hyperspectral imaging, nor the classification of cereals.

The aim of this study was to simultaneously separate sound white maize kernels from common undesirable material types as stipulated in the South African maize grading legislation. This was achieved through hierarchical assembly of classification models for the separation of 17 classes.

MATERIALS AND METHODS

Samples

White maize kernels and undesirable materials were obtained from the Southern African Grain Laboratory (SAGL, Pretoria, South Africa) and Pioneer Foods (Paarl, South Africa) in August, 2018. The sample sets were combined, as some defects did not occur in high enough numbers to justify using two sample sets. Both sets were silo samples, meaning that they are of mixed origin, cultivar and harvest date. All samples were graded visually by expert graders according to South African white maize grading regulations (Department of Agriculture, 2009). As seen in Table 3.1, this act stipulates five main categories, namely sound (healthy) white maize, defective white maize, pinked white maize, other colour (yellow) maize, and foreign materials. The legislation also stipulates sub-categories for defective kernels and foreign materials. Of the nineteen defects stipulated in the grading regulation, twelve were evaluated during this study since these were prevalent during the 2018 season. This included broken maize kernels (screenings), *Fusarium* fungal damage, *Diplodia* fungal damage, heat damage, water damage, frost damage, pest damage (rodent and insect), sprouted kernels and immature kernels. Foreign materials included five other common commodities, including soy, sorghum, sunflower seeds and wheat, as well as miscellaneous plant materials. See Fig. 3.1 for a digital image of all classes used in the study.

Stellenbosch University https://scholar.sun.ac.za

Table 3.1 White maize grading main categories and sub-categories, with their shorthand names used in this article and the maximum allowed levels for the best white maize grade (WM1).

Main category	Sub-categories	Shorthand	Max. level (WM1)
Sound white maize	-	Sound	N/A
Defective white maize	Broken kernels (screenings)	Screenings	
	Fusarium fungal damage	*Fusarium*	
	Diplodia fungal damage	*Diplodia*	
	Heat damage	Heat	
	Water damage	Water	7%
	Frost damage	Frost	
	Pest damage (rodent and insect)	Pest	
	Sprouted kernels	Sprouted	
	Immature kernels	Immature	
Pinked white maize	-	Pinked	20%
Yellow maize	-	Yellow	3%
Foreign materials	Soy	Soy	
	Sorghum	Sorghum	
	Sunflower seeds	Sunflower	0.3%
	Wheat	Wheat	
	Plant material	Plant	

Figure 3.1 Digital image of all sample classes: (a) sound; (b) *Fusarium*; (c) *Diplodia*; (d) heat; (e) water; (f) frost; (g) pest (rodent); (h) pest (insect); (i) sprouted; (j) immature; (k) pinked; (l) screenings; (m) yellow; (n) sorghum; (o) soy; (p) wheat; (q) sunflower; and (r) plant material.

Calibration and validation sample sets were selected at random for each of the 17 classes, where each set included 60 kernels/objects (60 for calibration and 60 for validation). There were three exceptions, namely (1) pest damage, which included separate sets of 60 kernels for rodent damage and insect damage (total of 120 for calibration and 120 for validation); (2) sprouted kernels, where 30 kernels were used in each set due to limited availability; and (3) immature kernels, where 54 kernels were used in each set due to limited availability. Overall, 1044 samples were used for calibration and 1044 for validation, giving a total of 2088 samples.

Stellenbosch University https://scholar.sun.ac.za

NIR hyperspectral system

Hyperspectral images were acquired using a short-wave infrared (SWIR) camera (Hyspex SWIR-384 Norsk Elektro Optikk, Norway) in reflectance mode. The camera has a mercury–cadmium–telluride (HgCdTe) detector and operated in the range 953 to 2517 nm, with 5.45 nm between each of the 288 spectral bands. Images were 384 pixels wide, and varied in length of *ca.* 700 pixels. The frame period was 3800 µs and the integration time was 3600 µs, chosen based on visually assessing the saturation images of the samples during test scans. Samples were illuminated with a halogen light source, which was switched on 10 minutes before imaging to avoid light source temperature drift and ensure spatial lighting uniformity. A 50% grey Zenith Allucore diffuse reflectance standard (SphereOptics GmbH, Germany) was used for image correction and calibration, and was scanned every 30 minutes during the imaging session.

Image acquisition

A unique calibration image and validation image were captured for each of the 17 classes individually. As pest damage comprised of rodent and insect damage, two image sets were taken for pest damage, giving a total of 18 calibration and validation image sets (36 images). 60 kernels/objects of a single class were arranged in a grid of 6 x 10. In applicable classes, the top three rows were placed with the maize germ facing up towards the camera, and the bottom three rows with germ facing down.

Hyperspectral image analysis

Image correction and cleaning

Radiometric calibration from irradiance to radiance to pseudo-absorbance was done in the Hyspex HySpex Ground software v4.1 (HySpex, Norsk Elektro Optikk, Norway). The grey reference image acquired most recently preceding the acquisition of each image was used.

Cleaning was conducted using the highly interactive Evince v.2.7.0 (UmBio AB, Umeå, Sweden) spectral image analysis software package. PCA was applied to the mean-centred absorbance mosaic images. Score plots and score images were used interactively to identify unwanted pixels, e.g. outliers, sample stage background, dead pixels, shading errors and edge effects (Esbensen and Geladi, 1989). A notable issue in several images was either specular reflection or overexposure occurring in some small regions. All unwanted pixels were removed.

Particle analysis

The cleaned images analysed further in PLS_Toolbox [Solo] (Eigenvector Research Inc., Wenatchee, WA) software package and subjected to particle (object) analysis. Objects were identified as isolated contiguous regions of pixels with similar intensity values. Each pixel was assigned either 0 or 1 to indicate non-object pixels (deleted background) and potential object pixels (maize kernels), creating a binary image or image mask. The properties of each object were calculated, such as mean spectrum, area, perimeter, centroid coordinates, circularity, aspect ratio, roundness and solidity. Only mean spectrum was kept as a variable. An image of *ca.*

Stellenbosch University https://scholar.sun.ac.za

200 000 pixel spectra was reduced to *ca.* 60 mean spectra while retaining spatial information. A table of the 60 mean spectra of each calibration image was created to further reduce the data size from *ca.* 100 MB to 100 KB. As the objects were numbered when calculated (i.e. 1 – 60), the information from the table could be related back to the image mask at a later stage.

The mean spectrum table of all 18 calibration images were combined to give one table with 288 wavebands as columns and 1044 samples as rows. Classes for each sample in the table were assigned. This was repeated for the validation data.

Mean spectrum pre-treatment

The following pre-treatments were considered: (1) mean-centring; (2) standard normal variate (SNV); (3) Savitzky-Golay transformation (various smoothing, polynomial and derivative parameters); and (4) detrending. Preliminary two-way PLS-DA models of sound maize vs. each class were calculated to evaluate the pre-treatment combinations based on cross-validated classification results (venetian blinds cross-validation). Pre-treatments yielding consistently good classification results were chosen. The combination of mean-centring, SNV and Savitzky-Golay (3 smoothing points; 3rd order polynomial; 1st derivative) were chosen (Barnes et al., 1989; Savitzky and Golay, 1964). No noisy wavebands were observed in the mean spectra, and thus all 288 wavebands were kept as variables.

Hierarchical model development and calibration

A series of 25 PLS-DA models were calculated and assembled in a hierarchical model that consisted of various levels and sub-levels. The calibration mean spectrum table (mean spectra of all 18 calibration images) was used to calibrate all PLS-DA models in the hierarchical model.

Hierarchical pathway Level 1 classified each object as either a foreign material or a maize kernel. A two-way PLS-DA model of a maize grouped class vs. a foreign material grouped class was calculated. The maize grouped class consisted of the sound white maize, all defective white maize classes, pinked white maize and yellow maize classes, and the foreign material grouped class consisted of soy, sorghum, sunflower seeds, wheat and plant material. If classified as a maize kernel, the object proceeded to the hierarchical model branch for maize kernel classification (Level 2), and if classified as a foreign material, the object proceeded to the hierarchical model branch for foreign material classification (Level 3).

At the second level, the maize hierarchical model was used to classify the following 12 classes: sound maize, screenings, *Fusarium* damage, *Diplodia* damage, heat damage, water damage, frost damage, pest damage, sprouted kernels, immature kernels, pinked maize, and yellow maize. The hierarchical model structure was designed based on separating the most easily separated class from the rest, with following steps working towards the most difficult class. The order was determined by calculating two-way PLS-DA models of one class vs. a grouped class of all other maize classes and evaluating the cross-validated classification result, where the classes were ordered according to descending model performance.

At the third level, the foreign material hierarchical model first separated objects into two main

Stellenbosch University https://scholar.sun.ac.za

categories of surface chemical composition, namely cellulose-rich and starchy. Thus, the first two-way PLS-DA separated a grouped class of soy, sorghum and wheat (starchy) and a grouped class of sunflower seeds and plant material (cellulose-rich). Next, a three-way PLS-DA separated soy, sorghum and wheat, and a two-way PLS-DA model separated sunflower seeds and plant material.

A secondary classification step was added to the decision tree for most classes, including both maize and foreign materials. This accounted for easily confused classes within the grouped class. For example, heat damage and yellow maize are easily confused. When a classification result of 'heat damage' was generated, this object was classified by a second two-way PLS-DA of heat damage vs. yellow maize. The result of the secondary classification was used as the final result in all instances where implemented.

Hierarchical model validation

The hierarchical model was tested using the validation mean spectrum table. The mean spectrum of each sample in the table was classified by the hierarchical model, beginning at the Level 1 classification of maize or foreign materials, and moving on to the relevant subsequent branches and models until a final classification was made.

The final classification was evaluated in two ways. First, if the main category was correct and, where relevant, second if the sub-category was correct. A validation image was created by shading the particle analysis image masks according to the predicted class. An object was shaded according to prediction result, with sound maize as orange, defective maize as green, yellow maize as yellow, pinked maize as pink and foreign materials as blue. A darker shading represented a correct main and sub-category (correct class) and lighter shading for correct main category only (misclassified as another class in the same main category). Misclassifications were shaded red. For legislative purposes, only the main category is necessary, but a human grader (to which this study is comparing spectral imaging) is able to see the difference between sub-categories.

Important spectral features

Variable importance in projection (VIP) scores were calculated based on the main PLS-DA models in each level or sub-level, i.e. all models except the secondary classification step. VIP scores evaluate the importance of each waveband for separating the classes in a PLS-DA model, where the VIP score of waveband k was calculated according to Eq. 2 as follows:

$$VIP_k = \sum_{j=1}^{a}\left(w_{jk}^2\, SSR_j\right)\frac{L}{SST} \qquad (2)$$

Where:

k = waveband

a = number of LVs in PLS-DA model

w = PLS weight of waveband k

SSR = residual sum-of-squares

L = number of wavebands (288)

SST = total sum-of-squares

Stellenbosch University https://scholar.sun.ac.za

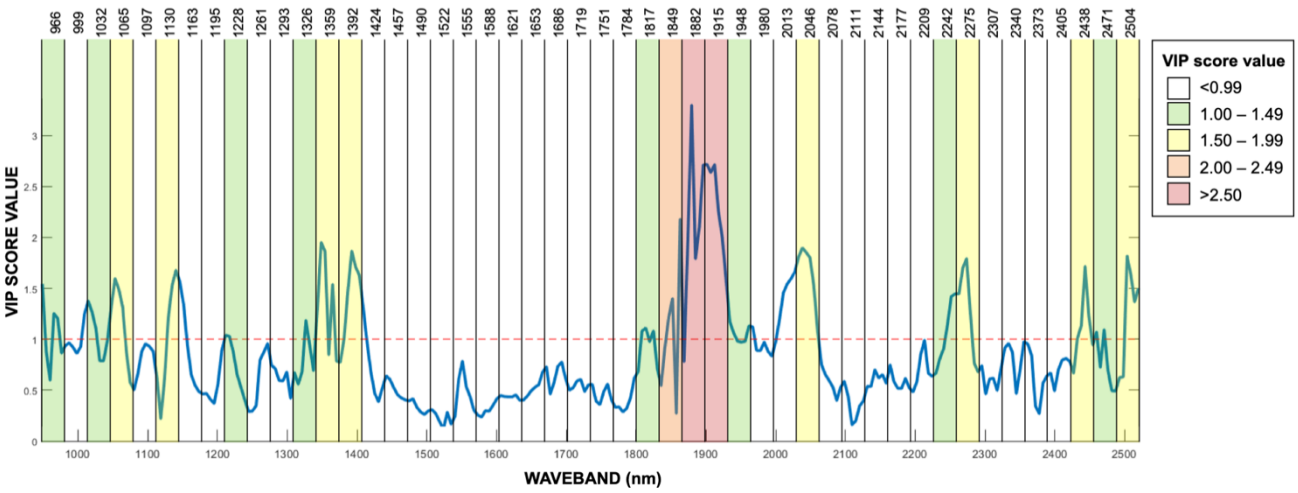

Figure 3.2 An example of the VIP scores line plot calculated from the PLS-DA classification model at Level 2e (water damage vs. group), with waveband windows shaded according to maximum VIP scores values.

The VIP scores are calculated based on the PLS-DA calibration dataset, and thus pre-processed spectra (mean-centring, SNV and Savitzky-Golay (3 smoothing points; 3rd order polynomial; 1st derivative)). A line chart was generated displaying waveband and VIP score value for each PLS-DA model (see Fig. 3.2). The maximum VIP score value for each peak was recorded. To overcome multicollinearity issues, as these peaks are broad and may have maxima at slightly different wavebands in different models, waveband windows or groupings were calculated. The 288 wavebands (953 – 2517 nm) were divided into 48 windows of 6 wavebands each with mean wavelengths as follows: 966, 999, 1032, 1065, 1097, 1130, 1163, 1195, 1228, 1261, 1293, 1326, 1359, 1392, 1424, 1457, 1490, 1522, 1555, 1588, 1621, 1653, 1686, 1719, 1751, 1784, 1817, 1849, 1882, 1915, 1948, 1980, 2013, 2046, 2078, 2111, 2144, 2177, 2209, 2242, 2275, 2307, 2340, 2373, 2405, 2438, 2471 and 2504 nm. If a maximum value appeared at any waveband in this window, it was recorded and shaded as follows: below 0.99 as unshaded, 1 to 1.49 as green, 1.5 to 1.99 as yellow, 2 to 2.49 as orange, and above 2.5 as red (Fig. 3.2). The common trends in peak VIP scores values across all the models were assessed and related to the raw spectrum and pre-treated spectrum, as used for modelling.

RESULTS AND DISCUSSION

Experimental design

The study aimed to emulate the current practices of industry grading as closely as possible. Based on legislative guidelines, the graders make logical decisions which cannot always be strictly defined. This is an important aspect of human decision-making that is difficult to replace using an automated analytical technique.

An important decision-making step occurred sorting the defective white maize samples used in the study. Many of the defects occur simultaneously, or one defect can make a kernel susceptible to another at a later stage. A kernel may become sprouted, water damaged and frost damaged during a bout of bad weather, rodent damage may leave a kernel vulnerable to insect or fungal infestation, and some ear diseases, including *Diplodia*, induce sprouting of kernels. Kernels presenting symptoms of multiple defects were encountered

Stellenbosch University https://scholar.sun.ac.za

regularly during the grading of samples for this study, where the grader determined the predominant defect. However, this is very subjective. Thus, if misclassifications occurred at the sub-category level, it was not considered a major shortfall. The legislation is based solely on levels of each main category (e.g. all defective kernels) and if a frost damaged kernel was misclassified as water damaged, this error would have no effect on the overall accuracy of the assigned grade.

Another consideration was dividing pest damage into rodent damage and insect damage in order to have sufficient samples of each damage type. While the legislation only considers 'pest damage', the two types are in fact not related at all, and this class would have been very heterogenous if combined. Decreased accuracy of the PLS-DA classification models was expected if the spectral signature was not consistent. Rodent damage is characterised by a single large bite, usually occurring at the germ (the oil-rich portion of the kernel). The mean spectrum of these samples is expected to exhibit proportionally higher absorption by starch and less absorption by fat. Insect damage is characterised by single or multiple boreholes anywhere on the kernel. However, it was often observed that a kernel exhibited both types of damage, and the class was assigned based on the most severe defect. During data analysis, it was found that the pest damage classes were very difficult to classify. Pest damage was chosen as the last class in the hierarchical model, thus it was not necessary to separate these two final classes (rodent and insect damage).

Hierarchical model development

The aims of this study presented two challenges, namely separating closely related samples and separating an unusually large number of classes compared to other similar hyperspectral imaging studies. This application was a good candidate for hierarchical modelling, where multiple classes are classified stepwise, working from most easily separated to most closely related. The structure of the hierarchical model is given in Table 3.2. An object starts at Level 1 and is classified as one of the two classes. According to this classification, it follows the relevant 'Proceed to' instructions to subsequent models until reaching a 'Final classification' instruction.

The first step was Level 1, where all maize classes and all foreign materials were separated based on only one PLS-DA latent variable (LV) ($Q^2 = 0.86$). If an object was classified as a maize kernel, it proceeded to classification in Level 2. If it was a foreign material, it proceeded to Level 3.

Level 2 was the most challenging section of the hierarchical model. Twelve closely related classes had to be separated sequentially, which included the main categories sound maize, yellow maize, pinked maize and defective maize (9 sub-categories). By calculating models of one class vs. grouped class of all remaining classes, the order was determined as follows: 2a – Screenings ($Q^2 = 0.74$); 2b – heat damage ($Q^2 = 0.55$); 2c – *Fusarium* fungal damage ($Q^2 = 0.68$); 2d – immature kernels ($Q^2 = 0.75$); 2e – water damage ($Q^2 = 0.50$); 2f – *Diplodia* fungal damage ($Q^2 = 0.61$); 2g – yellow maize ($Q^2 = 0.68$); 2h – sound white maize ($Q^2 = 0.81$); 2i – sprouted kernels ($Q^2 = 0.76$); 2j; frost damage ($Q^2 = 0.76$); 2k – pinked white maize and pest damage ($Q^2 = 0.75$).

The classification of foreign materials in Level 3 was less challenging, as this was separating different commodities, not classes of a single commodity. The previous findings of Sendin et al. (2019) revealed that the spectral signature of plant materials and sunflower seeds lacked absorbance by starch, leading to easy

Stellenbosch University https://scholar.sun.ac.za

differentiation of these two classes from the rest. Instead, these classes were characterised by a cellulose-rich surface chemistry. Thus, foreign materials were first separated as cellulose rich vs. starchy. A two-way PLS-DA model was calculated for plant material vs. sunflower seeds ($Q^2 = 0.89$). Only one LV was required, as the model error increased with the addition of LVs. Due to sufficient differences between wheat, soy and sorghum, a step-wise approach was not necessary, and a three-way PLS-DA was calculated ($Q^2 = 0.95$).

The secondary classification step was introduced to minimise misclassification between closely related classes. Due to the large number of classes used, a clear separation between each class was not expected. During hierarchical model development, the classification results of the one class vs. all remaining classes were examined. If a large number (*ca.* 5+) of the misclassifications were due to confusion with a specific class, a secondary step was included. If only one or two misclassifications were due to a specific class, the step was not included in order to avoid overfitting. Using similar classes screenings (broken kernels) and rodent damage (bitten kernels) as an illustration, the classification of screenings occurs early in the hierarchical model (Level 2a) when many classes remain. As rodent damage had not yet been classified (Level 2k), all rodent damage kernels should be classified in the group class and continue to subsequent classification steps. However, many were misclassified as screenings, and thus did not continue to the following steps. As a corrective measure, all objects classified as screenings were predicted by a second two-way PLS-DA model of screenings vs. rodent damage, where the result of this secondary step is taken as the final classification result. The secondary step classification models had higher Q^2 values and excellent cross-validated classification accuracies (often 98 – 100%), and single classes were well-defined and easily separated. The number of errors was greatly reduced by including this step.

To illustrate how a kernel ideally flows through the hierarchical model decision pathway from beginning to final classification, a heat damaged kernel is used as an example (see Table 3.2):

1. Level 1: Classified as the class ‘Group: sound, all defects, pinked & yellow’, where the instruction ‘Proceed to Level 2’ is given
2. Level 2a: Model of screenings vs. grouped class (heat, *Fusarium*, immature, water, *Diplodia*, yellow, sound, sprouted, frost, pinked & pest) classified the kernel as the grouped class, where the instruction ‘Proceed to Level 2b’ is given
3. Level 2b: Model of heat vs. grouped class (*Fusarium*, immature, water, *Diplodia*, yellow, sound, sprouted, frost, pinked & pest) classified the kernel as heat damaged, where the instruction ‘Proceed to 2nd classification’ is given
4. Second classification step: Model of heat damage vs. yellow maize classified the kernel as heat damage, giving a final classification of ‘heat damage’.

Stellenbosch University https://scholar.sun.ac.za

Table 3.2 Full spectrum hierarchical model structure, consisting of 3 main levels, 15 sub-levels and 25 PLS-DA classification models. Each object enters the decision pathway at Level 1 and follows the relevant instructions according to classification result by the PLS-DA model.

	CLASS ONE	CLASS TWO	CLASS THREE	2nd CLASSIFICATION	LVs; Q^2
LEVEL 1: MAIZE vs. FOREIGN MATERIALS					
1	Group: sound, all defects, pinked & yellow *Proceed to LEVEL 2*	Group: soy, sorghum, sunflower, wheat & plant *Proceed to LEVEL 3*	-	-	1: 7; 0.861
LEVEL 2: MAIZE CATEGORIES & SUBCATEGORIES					
2a	Screenings *Proceed to 2nd classification step*	Group: heat, *Fusarium*, immature, water, *Diplodia*, yellow, sound, sprouted, frost, pinked & pest *Proceed to 2b*	-	Screenings vs. pest (rodent) *Final classification = predicted class*	2a: 12; 0.744 2nd: 4; 0.810
2b	Heat *Proceed to 2nd classification step*	Group: *Fusarium*, immature, water, *Diplodia*, yellow, sound, sprouted, frost, pinked & pest *Proceed to 2c*	-	Heat vs. yellow *Final classification = predicted class*	2b: 16; 0.554 2nd: 7; 0.847
2c	*Fusarium* *Final classification* = 'Fusarium'	Group: immature, water, *Diplodia*, yellow, sound, sprouted, frost, pinked & pest *Proceed to 2d*	-	-	2c: 11; 0.678
2d	Immature *Proceed to 2nd classification*	Group: water, *Diplodia*, yellow, sound, sprouted, frost, pinked & pest *Proceed to 2e*	-	Immature vs. water *Final classification = predicted class*	2d: 10; 0.754 2nd: 8; 0.704
2e	Water *Proceed to 2nd classification*	Group: *Diplodia*, yellow, sound, sprouted, frost, pinked & pest *Proceed to 2f*	-	Water vs. yellow *Final classification = predicted class*	2e: 7; 0.501 2nd: 7; 0.938
2f	Diplodia *Final classification*= 'Diplodia'	Group: yellow, sound, sprouted, frost, pinked & pest *Proceed to 2g*	-	-	2f: 12; 0.612

Stellenbosch University https://scholar.sun.ac.za

2g	Yellow *Proceed to 2nd classification*	Group: sound, sprouted, frost , pinked & pest *Proceed to 2h*	-	Yellow vs. heat *Final classification = predicted class*	2g: 14; 0.678 2nd: 7; 0.847
2h	Sound *Final classification = 'Sound'*	Group: sprouted, frost, pinked & pest *Proceed to 2i*	-	-	2h: 14; 0.809
2i	Sprouted *Proceed to 2nd classification*	Group: frost, pinked & pest *Proceed to 2j*	-	Sprouted vs. water *Final classification = predicted class*	2i: 15; 0.757 2nd: 5; 0.867
2j	Frost *Proceed to 2nd classification*	Group: pinked & pest *Proceed to 2k*	-	Frost vs. water *Final classification = predicted class*	2j: 11; 0.758 2nd: 6; 0.835
2k	Pinked *Proceed to 2nd classification (1)*	Pest *Proceed to 2nd classification (2)*	-	(1)Pinked vs. sound (2) Pest vs. *Diplodia* *Final classification = predicted class*	2k: 4; 0.751 2nd (1): 11; 0.948 2nd (2): 16; 0.856
LEVEL 3: STARCHY vs. CELLULOSE-RICH FOREIGN MATERIALS					
3a	Soy, sorghum & wheat *Proceed to 3b*	Sunflower & plant *Proceed to 3c*	-	-	3a: 7; 0.968
3b	Soy *Final classification = 'Soy'*	Sorghum *Final classification = 'Sorghum'*	Wheat *Final classification = 'Wheat'*	-	3b: 6; 0.954
3c	Sunflower *Final classification = 'Sunflower'*	Plant *Proceed to 2nd classification*	-	Plant vs. screenings *Final classification = predicted class*	3c: 1; 0.893 2nd: 8; 0.913

Stellenbosch University https://scholar.sun.ac.za

Hierarchical model validation

The hierarchical model performed well, with high classification accuracy (75 – 100%) considering the challenging task of separating 17 classes. Both the sub-category and main category classification accuracy were recorded, describing if an object was classified as the correct class, or a class in the correct main category, respectively. The results were visualised as a classification image, as seen in Fig. 3.3.

The sub-category accuracy results were as follows: 88% for sound white maize, 60% for defective white maize, 83% for pinked white maize, 75% for yellow maize and 99% for foreign materials (Table 3.3). The sub- category accuracy of the defective white maize classes appears low (13 – 95%), but this should not

Figure 3.3 Classification image of the validation image dataset (1044 total) using the full spectrum hierarchical model. Dark shaded objects indicate correct main category and sub-category classification, light shaded objects indicate correct main category classification, and red shaded objects indicate misclassification (error).

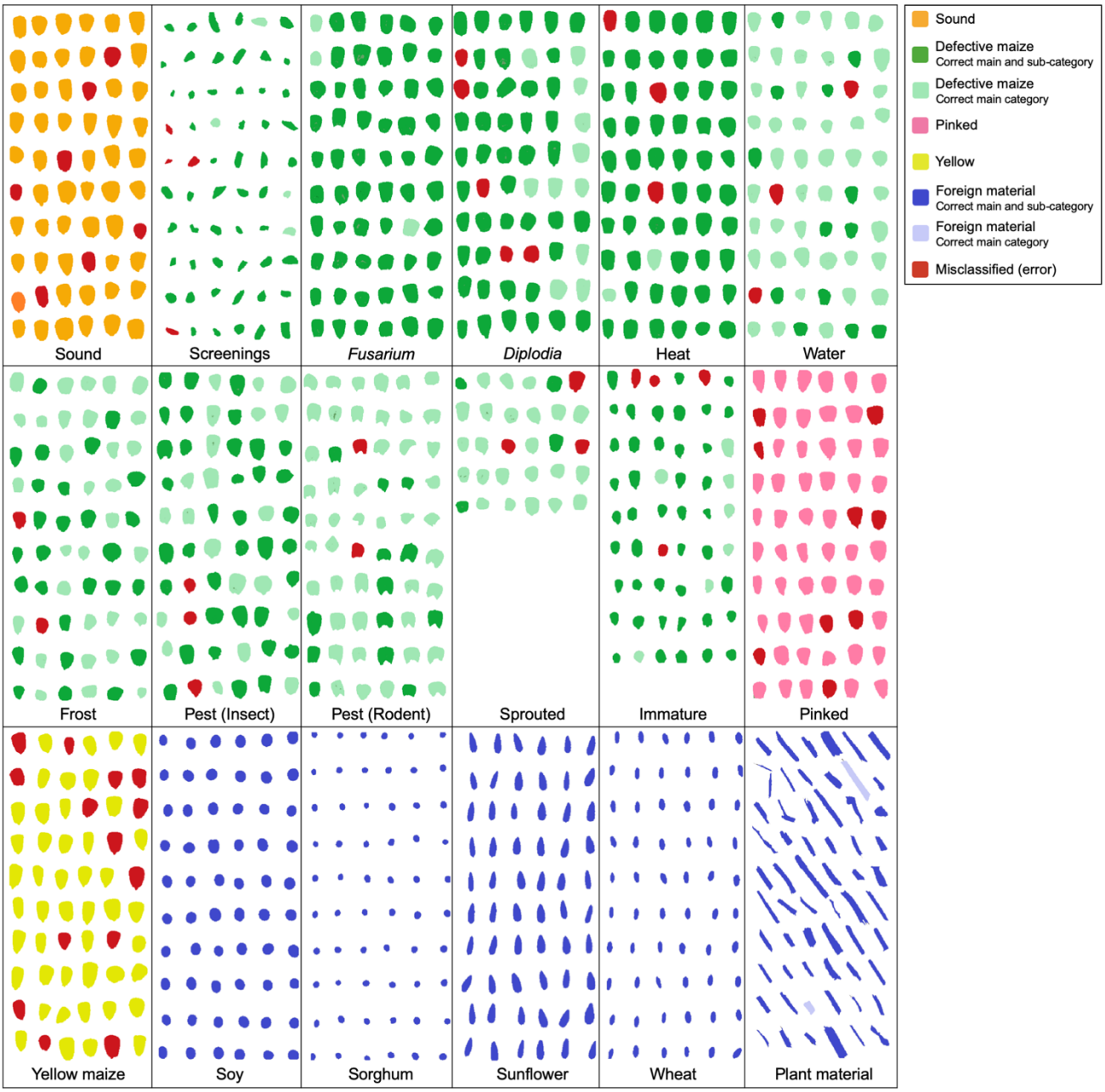

Stellenbosch University https://scholar.sun.ac.za

be of concern if they are misclassified among themselves and not as other main categories. As previously mentioned, these defects either occur simultaneously or cause vulnerability to other defects. For instance, the water damaged kernels (23% sub-category accuracy) were almost exclusively misclassified for frost damage and sprouting. Frost damage is often viewed as a severe form of water damage (see digital image in Fig. 3.1) and sprouting occurs as a result of prolonged exposure to water. Even an experienced grader struggles to determine the sub-category of kernels with differing severity of multiple defects. Thus, the class determined by the reference method (human grading) is not necessarily more accurate than the hyperspectral imaging method under investigation.

The main category accuracy is the most important parameter for grading based on the current legislation. An overall classification accuracy of 93.3% was achieved across the 1044 validation samples. The results were as follows: 88% for sound white maize, 93% for defecting white maize, 83% for pinked white maize, 75% for yellow maize and 100% for foreign materials (Table 3.3). There was a tremendous improvement in the accuracy of detecting defective maize kernels, demonstrating that classes were predominantly confused with sub-categories within the same main category.

The sound white maize class was the most important class to accurately classify, as a normal grading sample is expected to contain *ca.* 95% sound white maize. If a large number of errors occur in this class, an inaccurate grade is likely to be assigned. The results were fair, but 7 of the 60 kernels were misclassified. These misclassifications were of an array of defects, pinked and yellow maize, with no clear confusion with a specific class. Conversely, very few objects of other classes were misclassified as sound. In other words, the model was sensitive for the detection of undesirable materials but less specific for the detection of sound maize. This shows promise for ensuring a system that does not allow defective or unsafe materials to enter the food chain.

Although visually distinct, the separation of yellow maize was the most challenging. This was also observed in an earlier study by Sendin et al. (2019), where the two-way PLS-DA separation of white maize and yellow maize in a similar spectral region also achieved 75% correct classification. There is only one specific difference between white and yellow maize and it is determined by the presence of a single gene (Buckner et al., 1990). This gene controls the production of yellow beta-carotene pigment in the maize endosperm. The presence of two recessive alleles results in no pigment formation (white) and the presence of a single dominant allele causes pigment formation (yellow). While the two commodities are clearly different in the visible region, this distinct colour difference is due to beta carotene which has an absorbance maximum at 440 nm and does not interact strongly with NIR radiation (Sen Gupta & Ghosh, 2013). Thus, NIR spectroscopic techniques are not suited to detect this specific chemical constituent. Other differences in the chemical composition of maize samples, such as hardness, moisture content, oil content, can vary as greatly between cultivars of white maize as between white maize and yellow maize. The classification of yellow and white maize using NIR spectral imaging remains a challenge, and a possible solution is optimal waveband selection (Pu & Sun, 2015). The full NIR spectrum was used to calibrate the PLS-DA model separating yellow maize from the white maize classes. This full spectrum

Stellenbosch University https://scholar.sun.ac.za

Table 3.3 Validation results for the validation image (1044 samples in total). Sub-category classification indicates classification as the true class only, with main category classification as either the true class or a relevant sub-category, where applicable.

Main category	Sub-categories	Sub-category classification accuracy	Main category classification accuracy
Sound white maize	-	**88.3%**	**88.3%**
Defective white maize	Average	**60.0%**	**93.3%**
	Screenings	86.7%	93.3%
	Fusarium	95.0%	100%
	Diplodia	65.0%	90.0%
	Heat	91.7%	95.0%
	Water	23.3%	90.0%
	Frost	45.0%	96.7%
	Pest	40.0%	95.8%
	Sprouted	13.3%	86.7%
	Immature	79.6%	92.6%
Pinked white maize	-	**83.3%**	**83.3%**
Yellow maize	-	**75.0%**	**75.0%**
Foreign materials	Average	**99.3%**	**100%**
	Soy	100%	100%
	Sorghum	100%	100%
	Sunflower	100%	100%
	Wheat	100%	100%
	Plant	96.7%	100%
OVERALL		**75.5%**	**93.3%**

contains information related to chemical constituents that can vary within yellow maize and white maize samples (e.g. hardness), and thus would not lead to a robust classification model if included. If a handful of wavebands which correspond with unique properties of yellow maize are identified and the remainder are removed, a more reliable and accurate calibration could result (Feng et al., 2017; Wang et al., 2014).

A similar improvement is expected for pinked maize, as this class is also highly related to sound white maize. The light pink superficial discolouration of these maize kernels is due to the production of a red pigment, anthocyanin (Abdel-Aal, 2006). The discolouration is limited to the pericarp and does not affect meal colour after milling. Furthermore, it does not cause any other internal changes. Certain white hybrids are simply prone to pinking under specific climatic conditions, such as sunlight exposure, and the defect is very leniently legislated with a maximum allowed content of 20%. However, the subtlety of this defect resulted in a classification accuracy of only 83%. By conducting optimal waveband selection and removing wavebands not specifically linked to pinking, all variation that is not related to differences between the classes is removed and results are expected to improve.

Stellenbosch University https://scholar.sun.ac.za

Important spectral features

VIP scores reveal which wavebands are the biggest drivers of separation throughout all of the LVs calculated in a single PLS-DA model. This is an advantage over using loadings values, where it is difficult to assess the importance of a waveband when numerous components are calculated. The VIP scores of the following 15 models were calculated: Level 1; Level 2a – 2k; and Level 3a-c (Table 3.2). The secondary classification models were not considered in order to focus on the spectral variables driving separation of each class from the rest.

With 15 models and 288 wavebands, a large number of VIP scores were calculated and observing a clear pattern was challenging. This was largely due to the issue of multicollinearity associated with NIR spectral data. The interactions on which vibrational spectroscopy techniques are based are relatively low in intensity and occur among adjacent wavebands rather than at a single specific waveband. Thus, flattened broad bands appear instead of sharp peaks. When assessing the importance of a waveband across the 15 models, the peak VIP scores might occur at slightly different wavebands and the patterns may not be obvious. To simplify the dataset, avoid multicollinearity and offer a better overview, it was decided to divide the 288 wavebands into 48 windows or groupings of 6 wavebands each. If a peak VIP score occurred in any of the 6 wavebands in a group, it was assigned as the score for the group.

Higher VIP scores are considered more important. A score greater than 1 is considered as highly influential, between 0.8 and 1 as moderately influential, and less than 0.8 as less influential (Elmasry et al., 2008). Due to the large number of analyses, only wavebands with a score greater than 1 were investigated. The VIP scores results in Fig. 3.4 were shaded according to increasing value as follows: below 0.99 as unshaded, 1 to 1.49 as green, 1.5 to 1.99 as yellow, 2 to 2.49 as orange, and above 2.5 as red. This allowed easy visual assessment of important spectral regions, appearing as hot zones, and uninformative regions which remained blank.

Cereals, including maize, comprise of several major chemical constituents, namely starch, protein, fat/oil and water. When interpreting the NIR spectrum of cereal samples, prominent regions are expected to be associated with chemical bonds present in these constituents. The important spectral regions revealed by VIP scores analysis were related to the pre-processed mean spectrum of all 1044 samples, and found to be 969, 1149, 1334, 1405, 1563, 1672, 1901, 2032, 2245, 2305 and 2473 nm. Absorbance at 969 nm is associated with second overtone stretch vibration of O–H in water, while 1405 nm was due to first overtone O–H stretching from alcohol groups (R–OH) in starch (Weyer, 1985). A combination band (O–H stretch and 2 x C–O stretch) occurred at 1901 nm (Osborne & Fearn, 1986), which was the most prominent in the pre-processed spectrum and was assigned the highest VIP scores across the majority of models. The regions associated with C–H bonds were 1149 nm (second overtone, CH_3), 1334 (combination band, 2 x stretch and 1 x deformation, CH_3), 1672 nm (first overtone, cis alkanes and aromatics), 2305 nm (combination band, 1 x stretch and 1 x deformation, CH_2), and 2473 nm (combination band, C–H stretch and C–C stretch, starch) (Osborne & Fearn, 1986; Weyer, 1985). Constituents associated with C–H bonds were both starch and fat. Absorbance associated with protein occurred at 1563 nm (N–H first overtone stretch) and 2245 nm (combination band, N–H stretch and NH_3^+ deformation) (Osborne & Fearn, 1986). The band at 2032 nm was associated with C=O (second overtone) of

Stellenbosch University https://scholar.sun.ac.za

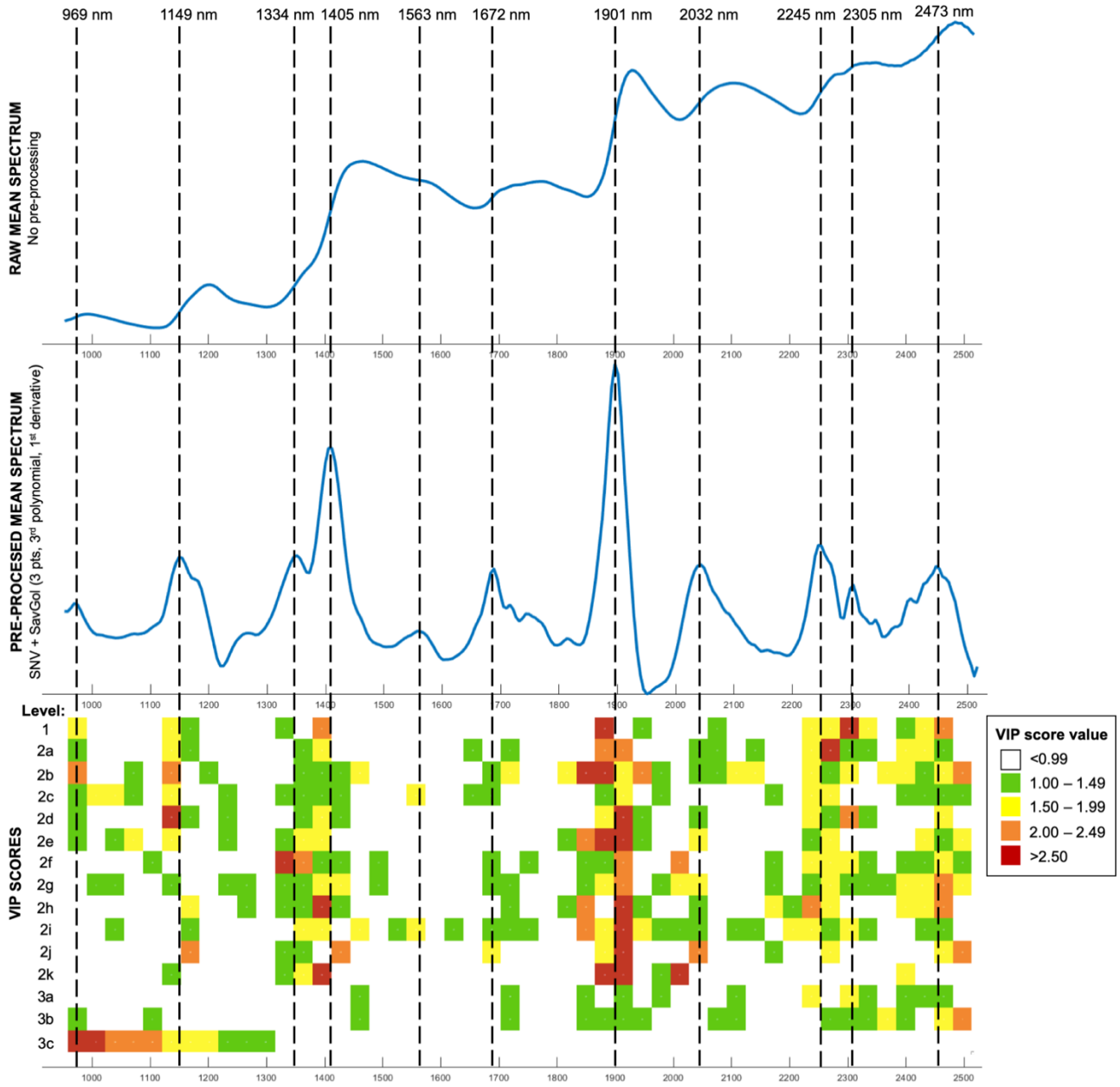

Figure 3.4 The raw mean spectrum of all 1044 calibration samples (top); the pre-processed mean spectrum with mean-centring, SNV and Savitzky-Golay (3 smoothing points; 3rd order polynomial; 1st derivative) transformations (middle); and the VIP scores for 48 waveband groups (6 wavebands per group) in the PLS-DA models in classification models at Level 1; Level 2a – 2k; and Level 3a-c.

amide ($CONH_2$) groups in amino acids (Osborne & Fearn, 1986). One set of VIP scores was vastly different to the rest, namely the classification of plant material and sunflower seeds at Level 3c. Findings by Sendin et al. (2019) demonstrated that the spectral signatures of sunflower seeds were characterised by strong absorption associated with cellulose, due to the impenetrable cellulose-rich husk surrounding the seed (Pérez-Vich et al. 1998). A broad peak in the region 1118 nm (the beginning of the spectrum) to *ca*. 1300 nm was observed in the previous study. The VIP scores in this study reflect a similar pattern, with only the wavebands spanning 953 to

Stellenbosch University https://scholar.sun.ac.za

1296 nm driving separation between sunflower seeds and plant materials. Furthermore, the previous study's sunflower seed spectra lacked the bands associated with starch that appeared in the spectra of other commodities such as maize, wheat, sorghum and soy. Little variance was attributed the other abovementioned VIP wavebands, which all had VIP scores below 1. In addition, the two classes were extremely different, and only one LV was required to achieve an accurate separation. The second LV contained little useful inter-class variation and was not selected due to a large amount of noise. As each LV is often characterised by variation at different wavebands, a model with numerous LVs has a large number of wavebands with moderately high VIP scores and a model with one LV has a small number of wavebands with extremely high VIP scores.

CONCLUSION

The South African maize industry currently relies on a laborious manual method to conduct white maize grading, an essential step in the maize market value chain. To improve and modernise this process, NIR hyperspectral imaging has been considered as an automated alternative. Advantages to manual inspection include human decision-making and the ability to evaluate multiple classes of objects simultaneously, and these were a challenge to emulate using a hyperspectral camera and computer software. A series of PLS-DA classification models were assembled in a hierarchical model structure consisting of three main levels. First to separate maize and foreign materials, second to further classify the maize kernels into the maize grading categories and sub-categories, and third to further classify the foreign materials sub-categories. The system easily separated maize from foreign materials (100% classification accuracy) and classified the foreign material sub-categories almost perfectly (99.3%). The maize categories were closely related and more difficult to accurately separate, including sound white maize (88%), defective white maize (93%), pinked white maize (83%) and yellow maize (75%). Some sub-categories of defective kernels were often confused with one another, but only the main category counts towards the assigned grade according to legislation, and thus should not cause concern. This was often due to some single kernels being affected by multiple defects. In these cases, a human grader chooses the more severe defect, which is subjective. An overall classification accuracy of 93.3% was achieved across the 1044 validation samples. This is an impressive result considering that each object was classified by a decision pathway consisting of 17 classes, 15 levels and sub-levels and 25 PLS-DA models with numerous points at which mistakes could be made. However, the grading legislation is strict and the classification accuracy of some classes, specifically sound white maize, yellow maize and pinked white maize, must be further improved in order for spectral imaging to be considered by the maize industry. Optimal waveband selection has demonstrated improvement of classification results in similar studies and is recommended for increased classification accuracy.

REFERENCES

Abdel-Aal, E.-S. M., Young, J. C. & Rabalski, I. (2006). Anthocyanin composition in black, blue, pink, purple, and red cereal grains. *Journal of Agricultural and Food Chemistry,* **54,** 4696-4704.

Stellenbosch University https://scholar.sun.ac.za

Barnes, R. J., Dhanoa, M. S. & Lister, S. J. (1989). Standard normal variate transformation and de-trending of near-infrared diffuse reflectance spectra. *Applied Spectroscopy,* **43,** 772-777.

Buckner, B., Kelson, T. L. & Robertson, D. S. (1990). Cloning of the y1 Locus of Maize, a Gene Involved in the Biosynthesis of Carotenoids. *The Plant Cell,* **2,** 867-876.

Department of Agriculture (2009). Regulations relating to the grading, packing and marking of maize intended for sale in the Republic of South Africa. In: *Agricultural Product Standards Act (Act No. 119 of 1990).*

Dupuy, N., Galtier, O., Ollivier, D., Vanloot, P. & Artaud, J. (2010). Comparison between NIR, MIR, concatenated NIR and MIR analysis and hierarchical PLS model. Application to virgin olive oil analysis. *Analytica Chimica Acta,* **666,** 23-31.

ElMasry, G., Wang, N., Vigneault, C., Qiao, J. & ElSayed, A. (2008). Early detection of apple bruises on different background colors using hyperspectral imaging. *LWT-Food Science and Technology,* **41,** 337-345.

Esbensen, K. & Geladi, P. (1989). Strategy of multivariate image analysis (MIA). *Chemometrics and Intelligent Laboratory Systems,* **7,** 67-86.

Feng, X., Zhao, Y., Zhang, C., Cheng, P. & He, Y. (2017). Discrimination of transgenic maize kernel using NIR hyperspectral imaging and multivariate data analysis. *Sensors,* **17,** 1894.

Menze, B. H., Petrich, W. & Hamprecht, F. A. (2007). Multivariate feature selection and hierarchical classification for infrared spectroscopy: serum-based detection of bovine spongiform encephalopathy. *Analytical and Bioanalytical Chemistry,* **387,** 1801-1807.

Myles, A. J. & Brown, S. D. (2004). Decision pathway modeling. *Journal of Chemometrics,* **18,** 286-293.

Osborne, B. G. & Fearn, T. (1986). Theory of near infrared spectroscopy. In: *Near infrared spectroscopy in food analysis*. Pp. 29-33. Harlow, UK: Longman Scientific & Technical.

Pérez-Vich, B., Velasco, L. & Fernández-Martínez, J. (1998). Determination of seed oil content and fatty acid composition in sunflower through the analysis of intact seeds, husked seeds, meal and oil by near-infrared reflectance spectroscopy. *Journal of the American Oil Chemists' Society,* **75,** 547-555.

Pu, H., Kamruzzaman, M. & Sun, D.-W. (2015). Selection of feature wavelengths for developing multispectral imaging systems for quality, safety and authenticity of muscle foods-a review. *Trends in Food Science & Technology,* **45,** 86-104.

Salimi-Khorshidi, G., Douaud, G., Beckmann, C. F., Glasser, M. F., Griffanti, L. & Smith, S. M. (2014). Automatic denoising of functional MRI data: combining independent component analysis and hierarchical fusion of classifiers. *Neuroimage,* **90,** 449-468.

Savitzky, A. & Golay, M. J. (1964). Smoothing and differentiation of data by simplified least squares procedures. *Analytical Chemistry,* **36,** 1627-1639.

Sen Gupta, S. & Ghosh, M. (2013). In Vitro Antioxidative Evaluation of-and-Carotene, Isolated from Crude Palm Oil. *Journal of Analytical Methods in Chemistry*, **2013**.

Stellenbosch University https://scholar.sun.ac.za

Sendin, K., Manley, M., Baeten, V., Pierna, J. A. F. & Williams, P. J. (2019). Near Infrared Hyperspectral Imaging for White Maize Classification According to Grading Regulations. *Food Analytical Methods,* **12,** 1612-1624.

Wang, L., Sun, D.-W., Pu, H. & Zhu, Z. (2016). Application of hyperspectral imaging to discriminate the variety of maize seeds. *Food Analytical Methods,* **9,** 225-234.

Weyer, L. G. (1985). Near-infrared spectroscopy of organic substances. *Applied Spectroscopy Reviews,* **21,** 1-43.

Stellenbosch University https://scholar.sun.ac.za

CHAPTER 4:

WAVEBAND SELECTION FOR MUTISPECTRAL WHITE MAIZE, DEFECT AND FOREIGN MATERIAL CLASSIFICATION

ABSTRACT

The number of wavebands in the original hyperspectral image data from 288 was reduced to a more realistic number to inform the development of an affordable, rapid and accurate white maize grading system. Three methods to reduce the number of wavebands were explored, namely the use of waveband windows (48 wavebands), waveband optimisation based on VIP scores (21 wavebands), and waveband optimisation using the CovSel algorithm (13 wavebands). PLS-DA-based hierarchical decision pathways were calculated based on these three reduced waveband sets. The waveband windows approach allowed for the removal of 87% of the wavebands with only a 6% decrease in overall classification accuracy. The number of wavebands was further halved by selecting the most important windows based on VIP scores, with a further 3% loss of classification accuracy. The CovSel waveband set was the smallest but did not represent important wavebands in the range 2250 to 2512 nm (associated with starch and cellulose). While the overall classification accuracy only dropped a further 2%, sound white maize and yellow maize were misclassified too frequently. Considering the trade-off between the performance and cost of all three potential multispectral systems, the results indicate that the optimal waveband set for white maize grading is based on VIP scores as follows: 964, 1127, 1159, 1323, 1356, 1388, 1421, 1716, 1847, 1879, 1912, 1945, 2043, 2239, 2272, 2305, 2337, 2403, 2435, 2468 and 2501 nm.

Stellenbosch University https://scholar.sun.ac.za

INTRODUCTION

Hyperspectral imaging has been used extensively in cereal science research to evaluate a large array of cereal properties, including hardness classification, chemical composition, variety identification, sprouting detection, physical quality classification, fungal contamination detection and parasitic contamination detection (Sendin et al., 2018). However, due to crucial drawbacks of the technique, it is seldom implemented for routine analysis in industry. These drawbacks include the high cost and relatively low speed of the hyperspectral imaging instruments found in research laboratories. A viable solution to these issues is the development of a multispectral imaging instrument that is tailor-made for one application. A bonus is that by eliminating multicollinearity issues, the accuracy of the predictions may improve. To develop these multispectral systems, a study on hyperspectral image data is usually conducted to identify important wavebands most related to the property under investigation. A previous study investigated the use of a pre-built multispectral imaging instrument (VideometerLab2, Videometer, Hørsholm, Denmark) to classify similar maize classes based on 19 wavebands in the range 375 to 970 nm (Sendin et al., 2018). However, the selected spectral regions were not optimised for maize classification and the two-way PLS-DA models performed with lower classification accuracies than a full NIR hyperspectral imaging instrument.

Waveband selection studies have been successfully conducted for separating grain from foreign material (Wallays et al., 2009), identifying maize, rice and black bean variety (Wang et al., 2014; Wang et al., 2015a; Sun et al., 2016), detecting genetically modified maize (Feng et al., 2017), tracking texture deterioration in fresh maize (Wang et al., 2015b) and determining spelt flour authenticity (Su & Sun, 2016). Generally, these studies greatly reduced the number of wavebands in the original dataset (*ca.* 200 – 400) to a handful (*ca.* 10) using sophisticated waveband optimisation techniques, including successive projection algorithm (SPA), competitive reweighted adaptive sampling (CARS), genetic algorithm (GA), first-derivative and mean centring iteration algorithm (FMCIA), and regression coefficients. While GA has been utilised successfully in the analysis of spectral data for many years (Leardi & Gonzalez, 1998), the use of SPA and CARS has been on the rise in recent years.

SPA is a forward selection method that aims to minimise collinearity between spectral variables by means of successive projections on interlinked sub-spaces (Roger et al., 2011). At each step, a waveband is selected based on the maximum projection in the orthogonal sub-space generated by the previously selected variable. However, as SPA is based only on the **X**-data, resulting selections are based solely on the spectral data without considering the class information (**y**-data) (Vigneau & Thomas, 2012). In the case of closely-related classes, the class information should be considered to identify wavebands highlighting the differences between two classes. Inspired by SPA, covariance selection (CovSel) was developed to work in a similar way, but this method accounts for the covariance between the **X**- and **y**-data. Simply put, the difference between the two is comparable with the differences between principal component analysis (PCA) and partial least squares (PLS). In each successive step, the waveband presenting the highest covariance is identified and all the other wavebands and the y-responses are orthogonalised to it (Biancolillo et al., 2019). Iterations continue until a

Stellenbosch University https://scholar.sun.ac.za

fixed number of variables has been selected. This allows CovSel to select the wavebands that are most relevant to regression or classification (supervised), and not just separation of samples in general (unsupervised).

The aim of this study was to reduce the number of wavebands in the original hyperspectral image data from 288 to a more realistic number to inform the development of an affordable, rapid and accurate white maize grading system. Three methods to reduce the number of wavebands were explored, namely the use of waveband windows, waveband optimisation based on VIP scores, and waveband optimisation using the CovSel algorithm. PLS-DA-based hierarchical decision pathways were calculated based on these three reduced waveband sets.

MATERIALS AND METHODS

Waveband selection was conducted based on the same hyperspectral dataset as Chapter 3. See Chapter 3 for further information on the samples, NIR hyperspectral imaging system, image acquisition, image correction and cleaning, particle analysis and PLS-DA model calculation.

Hyperspectral image analysis

Optimal waveband selection

Reduced spectral channels (windows)

The number of spectral channels was reduced by dividing the 288 wavebands (953 – 2517 nm) into 48 windows of 6 wavebands. The third waveband in each window was chosen as the centre point. 964, 996, 1029 1062, 1095, 1127, 1159, 1193, 1225, 1258, 1291, 1323, 1356, 1388, 1421, 1454, 1487, 1520, 1552, 1585, 1618, 1651, 1683, 1716, 1749, 1781, 1814, 1847, 1879, 1912, 1945, 1978, 2010, 2043, 2076, 2108, 2141, 2174, 2206, 2239, 2272, 2305, 2337, 2370, 2403, 2435, 2468 and 2501 nm.

Variable importance in projection scores

VIP scores were calculated in Chapter 3. These scores were evaluated according to the maximum value appearing in each of the 48 waveband windows. A VIP score value greater than 1 indicated that a window was highly influential for the separation of a particular class. 15 sets of VIP scores were calculated according to the PLS-DA models at the main levels and sub-levels of the full spectrum hierarchical model (Chapter 3). Any window scoring >1 in 7 or more of the 15 PLS-DA models was chosen as part of the optimised waveband set. The 21 selected wavebands were: 964, 1127, 1159, 1323, 1356, 1388, 1421, 1716, 1847, 1879, 1912, 1945, 2043, 2239, 2272, 2305, 2337, 2403, 2435, 2468 and 2501 nm.

Covariance selection

CovSel was calculated based on methods described by Roger et al. (2011) and Biancolillo et al. (2019). The process takes place in two main steps: (i) identifying the variable with the highest covariance by calculating the covariance between all the **X**- and **y**-variables; and (ii) projecting all the **X**- and **y**-variables orthogonally to the identified variable until an optimal number of wavebands was selected. The 13 selected wavebands were: 953, 1122, 1340, 1416, 1574, 1721, 1869, 1901, 1939, 1994, 2097, 2250 and 2512 nm.

Stellenbosch University https://scholar.sun.ac.za

Mean spectrum pre-treatment

The calibration and validation mean spectrum tables calculated in Chapter 3 were used. The selected wavebands from each set were used as the spectral variables in the calculations. The data associated with the non-selected wavebands were simply removed, and no averaging or binning was conducted. A combination of mean-centring and SNV were applied (Barnes et al., 1989). Savitzky-Golay transformation was not applied to these discrete datasets, as the transformation involves smoothing and the calculation of derivatives which require continuous points.

Hierarchical model development and calibration

Three series of PLS-DA models were recalculated using the 48 window wavebands, 21 wavebands selected based on VIP scores and 13 wavebands selected using CovSel. A hierarchical model was assembled for each of the three waveband sets. The method for hierarchical model structure development detailed in Chapter 3 was followed. However, the specific order of the sub-levels in each hierarchical model was optimised individually according to the performance of the PLS-DA models. See Tables S1, S2 and S3 for the structures of the windows, VIP and CovSel hierarchical models, respectively.

Hierarchical model validation

The hierarchical models were tested using the validation mean spectrum table and classification images were generated, as detailed in Chapter 3.

RESULTS AND DISCUSSION

The classification of maize samples using reduced waveband sets were simulated by only including selected wavebands from the original set of 288 wavebands. This resulted in the classification of the 17 classes using PLS-DA models based on 16.7, 7.3 and 4.5% of the original spectral variables using the windows, VIP and CovSel sets, respectively. The main category classification describes correct classification according to the 5 main categories, and the overall classification accuracy decreased from 93.3% using the full spectrum to 87.1, 84.5 and 81.9% using the windows, VIP and CovSel waveband sets (Table 1). The classification images for the three wavebands sets are given as Figs. S1, S2 and S3 in the supplementary data.

The positions of the wavebands in each of the three sets are given in Fig. 1. The windows waveband set was not chosen according to an optimisation technique, but the broad spectral features associated with NIR allowed for all regions with high absorbance to be represented by one or more of the 48 wavebands. The wavebands selected using VIP and CovSel were similar in some areas and differed in others. Both sets of wavebands were optimised at similar points in the region ca. 960 to 2100 nm. However, the VIP waveband set included eight wavebands in the region 2250 to 2512 nm, while the CovSel set included only two. This region is mainly attributed to absorption by C–H and C–C bonds in starch and cellulose, both major chemical

Stellenbosch University https://scholar.sun.ac.za

components in maize and other cereals. The lack of representative wavebands from this region in the CovSel set likely contributed to the superior classification by the VIP hierarchical model (Table 1).

Table 4.1 Validation results for the validation image (1044 samples in total) when classifying main category using the hierarchical models based on the full spectrum (288 wavebands), windows wavebands (48), VIP wavebands (21) and CovSel wavebands (13).

Main category	Sub-categories	Full (288)	Windows (48)	VIP (21)	CovSel (13)
Sound white maize	-	**88.3%**	**76.7%**	**78.3%**	**63.3%**
Defective white maize	Average	**93.3%**	**86.7%**	**83.2%**	**81.0%**
	Screenings	93.3%	78.3%	78.3%	73.3%
	Fusarium	100%	88.3%	86.7%	83.3%
	Diplodia	90.0%	90.0%	71.7%	78.3%
	Heat	95.0%	76.7%	76.7%	61.7%
	Water	90.0%	88.3%	81.7%	76.7%
	Frost	96.7%	90.0%	86.7%	85.0%
	Pest	95.8%	93.3%	82.5%	88.3%
	Sprouted	86.7%	90.0%	86.7%	93.3%
	Immature	92.6%	85.2%	98.1%	88.9%
Pinked white maize	-	**83.3%**	**75.0%**	**78.3%**	**80.0%**
Yellow maize	-	**75.0%**	**60.0%**	**56.7%**	**48.3%**
Foreign materials	Average	**100%**	**96.7%**	**95.7%**	**94.32%**
	Soy	100%	100%	100%	100.0%
	Sorghum	100%	98.3%	100%	98.3%
	Sunflower	100%	100%	100%	100%
	Wheat	100%	85.0%	83.3%	83.3%
	Plant	100%	100%	95.0%	90.0%
OVERALL		**93.3%**	**87.1%**	**84.5%**	**81.9%**

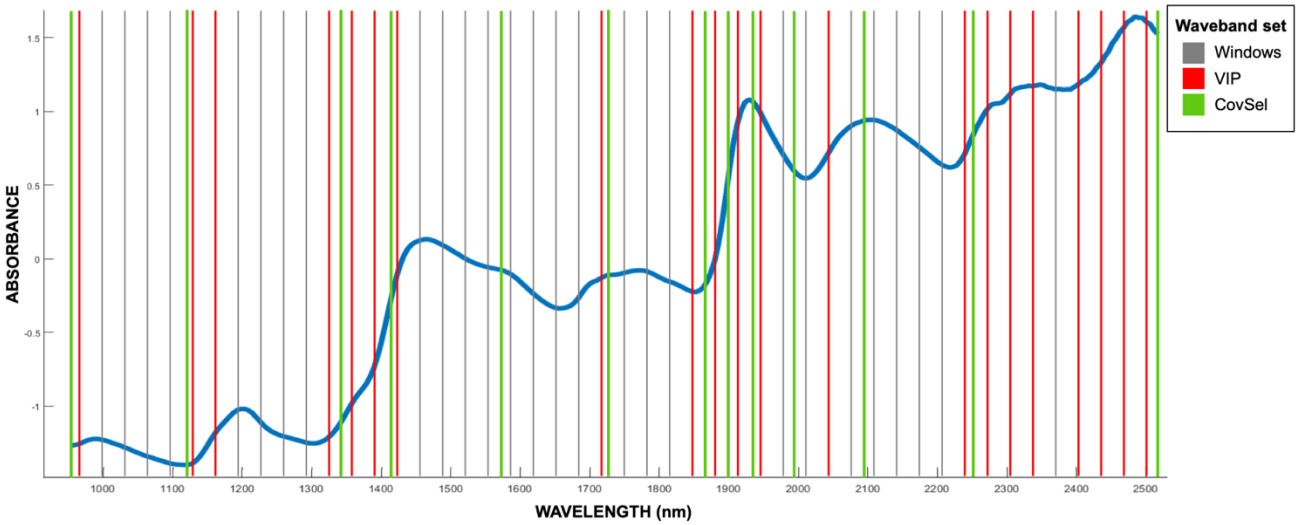

Figure 4.1 The pre-processed mean spectrum (SNV transformation) with the windows (grey and red), VIP (red) and CovSel (green) waveband sets indicated.

Stellenbosch University https://scholar.sun.ac.za

Reduced spectral channels (windows)

Spectral features in NIR spectroscopy (e.g. harmonics and combination bands) are associated with broad peaks. Pure substances are often characterised by natural bandwidths larger than 10 nm, while mixtures are usually broader (Galvão et al., 1999; Golic et al., 2003). Examples of these large bandwidths include 22.5 nm for sucrose(2046 nm), 30.1 nm for maize oil (2305 nm), 110.4 nm for moisture (1928 nm) and 162 nm for wheat starch (2103 nm) (Metrohm AG, 2019). The hyperspectral instrument's full spectrum contained wavebands spaced at intervals of 5.45 nm, and each window of 6 wavebands was spaced at 32.7 nm. Thus, many of the spectral features that play a role in classifying maize kernels spanned one or more windows (Fig. 1).

The number of channels acquired by a spectroscopic instrument plays a role in determining its spectral resolution, as a large number of channels will require a spectrograph with a high spectral resolution. The spectral resolution describes an instrument's ability to resolve adjacent spectral features and bands, and the resolution required depends on the application involved. An instrument with a high spectral resolution will be expensive, as a more costly sensor is required. When considering the requirements of an instrument for a specific application, a trade-off between performance and price is often unavoidable. The windows-based hierarchical model did not perform as accurately as the full spectrum model, with a drop in accuracy from 93.3 to 87.1%. The hierarchical model exhibited a decreased classification accuracy across all classes in comparison with the full spectrum (Tables 1 and 2). Furthermore, the windows waveband set did not offer better classification performance than the other two reduced waveband sets in a number of classes. While an instrument that acquires only 48 wavebands will cost less than the hyperspectral instrument with 288 wavebands, it would be the most expensive of the three optimised sets presented. The trade-off between instrument performance and cost associated with the windows waveband set was not favourable.

Variable Importance in Projection (VIP)

The selection of optimal wavebands based on VIP scores is a relatively basic method in comparison with some of the sophisticated algorithms recently cited in literature. The VIP score of a waveband is based on its significance in all LVs of a PLS-DA model. As 15 PLS-DA models were included in the main and sub-levels of the hierarchical model, a waveband was selected as optimal if it scored >1 in seven or more of the models. This resulted in the selection of 21 wavebands, some of which were discussed as important drivers in the full spectrum hierarchical model. A large number of these wavebands were attributed to starch, including 1879 nm (O–H stretch and C–O stretch), 2272 nm (O–H stretch and C–C stretch), 2435 nm, 2468 and 2501 nm (all C–H stretch and C–C stretch). Absorption bands related to cellulose were in close proximity to the starch associated wavebands, as the two chemical components are very similar, and included 1847 nm (O–H and C–O stretch) and 2337 nm (C–H stretch and deformation). Wavebands attributed to protein or amino acids included 1127 nm (N–H stretch), 2043 nm (N–H symmetrical stretch) and 2239 nm (N–H stretch and NH_3 deformation). While CH_2 and CH_3 groups are common in organic molecules, fats are the main chemical components in maize associated with these functional groups and were related to 1159 nm (C–H stretch), 1323 nm (C–H stretch and deformation), 1716 nm (C–H stretch) and 2305 nm (C–H stretch and deformation). The wavebands linked to

Stellenbosch University https://scholar.sun.ac.za

moisture were among the less significant VIP scores, which included 964 nm (O–H stretch), 1945 nm (O–H stretch and deformation) and 2403 nm (O–H deformation). The absorption bands at 1421 and 1912 nm (both O–H stretch) were associated with alcohol groups. Specifically, 1421 nm is attributed to absorption by an aromatic alcohol and may be related to the amino acid tyrosine, as maize is known to be rich in this minor component (FAO, 1992).

The performance of the hierarchical models based on the windows and VIP wavebands sets were comparable. While the windows waveband set resulted in an 86.7% reduction in the number of spectral variables, this was further reduced to give an overall elimination of 92.7% with almost no further loss of classification accuracy. The classification accuracy of white maize was 78.3%, which is a 10% drop from the full spectrum classification. This was concerning, as the majority of a white maize grading sample is expected to belong to this class and a large error is likely to result in an unacceptably high rate of misclassification. However, of the three reduced waveband sets, the VIP set performed best for the sound maize class. The classification accuracy for the defective white maize main category also decreased by 10%. This change was most notable in the subtle defects. Screenings (15% decrease compared to full spectrum) are broken maize kernels, where some of the pieces of maize kernel have a very similar spectral signature to whole maize kernels. *Diplodia* fungal damage (19% decrease) is a subtle defect that is less pronounced than *Fusarium* fungal damage. This class was the most frequently misclassified defect when using only the VIP wavebands. The large drop in

Table 4.3 Validation results for the validation image (1044 samples in total) using the VIP hierarchical model. Sub-category classification indicates classification as the true class only, with main category classification as either the true class or a relevant sub-category, where applicable.

Main category	Sub-categories	Sub-category classification accuracy	Main category classification accuracy
Sound white maize	-	**78.3%**	**78.3%**
Defective white maize	Average	**46.41%**	**83.23%**
	Screenings	61.7%	78.3%
	Fusarium	23.3%	86.7%
	Diplodia	28.3%	71.7%
	Heat	58.3%	76.7%
	Water	45.0%	81.7%
	Frost	48.3%	86.7%
	Pest	45.8%	82.5%
	Sprouted	20.0%	86.7%
	Immature	87.0%	98.1%
Pinked white maize	-	**78.3%**	**78.3%**
Yellow maize	-	**56.7%**	**56.7%**
Foreign materials	Average	**95.3%**	**95.7%**
	Soy	100%	100%
	Sorghum	98.3%	100%
	Sunflower	100%	100%
	Wheat	83.3%	83.3%
	Plant	95.0%	95.0%
OVERALL		**64.0%**	**84.5%**

Stellenbosch University https://scholar.sun.ac.za

classification accuracy of heat damage (18% decrease) was unexpected, as this defect results in a deep yellow colour that is easily distinguishable from sound white maize. However, this error was linked to the large decrease in classification accuracy for yellow maize (15% decrease), as a large proportion of the heat damaged kernels were misclassified as yellow maize and *vice versa*. The classification of sprouted kernels (0% change) remained the same using the reduced waveband set, while the classification accuracy of immature kernels improved (5.5% increase). Pinked maize was difficult to classify using the full spectrum, and while a 5% decrease was observed in comparison to the full spectrum, the VIP hierarchical model outperformed the windows hierarchical model by 3%. Lastly, a small number of the foreign materials were misclassified (4% decrease), but the occurrence of these materials is very rare due to the use of dockage sorters early in the processing of maize. A classification accuracy of 95.7% is considered high in NIR hyperspectral imaging applications, and comparable to the performance of the windows hierarchical model (96.7%).

Covariance selection

CovSel is a variable selection method that has not been reported extensively in literature, but is a hybrid of the popular SPA technique. It was prudent to use CovSel in this application, as the samples within each class were highly heterogenous. An unsupervised technique (e.g. SPA) will identify sources of variation between all the

Table 4.4 Validation results for the validation image (1044 samples in total) using the CovSel hierarchical model. Sub-category classification indicates classification as the true class only, with main category classification as either the true class or a relevant sub-category, where applicable.

Main category	Sub-categories	Sub-category classification accuracy	Main category classification accuracy
Sound white maize	-	**63.3%**	**63.3%**
Defective white maize	Average	**36.4%**	**81.0%**
	Screenings	61.7%	73.3%
	Fusarium	30.0%	83.3%
	Diplodia	41.7%	78.3%
	Heat	36.7%	61.7%
	Water	51.7%	76.7%
	Frost	8.3%	85.0%
	Pest	28.3%	88.3%
	Sprouted	30.0%	93.3%
	Immature	38.9%	88.9%
Pinked white maize	-	**80.0%**	**80.0%**
Yellow maize	-	**48.3%**	**48.3%**
Foreign materials	Average	**92.98%**	**94.32%**
	Soy	98.3%	100%
	Sorghum	98.3%	98.3%
	Sunflower	100%	100%
	Wheat	80.0%	83.3%
	Plant	88.3%	90.0%
OVERALL		**55.7%**	**81.9%**

Stellenbosch University https://scholar.sun.ac.za

spectra, regardless of class, and would thus include intra-class variation. By considering the covariance between the **X**- and **y**-variables, only differences between the classes were considered. None of the wavebands selected using CovSel matched the VIP wavebands exactly. However, nine of the thirteen were associated with the same spectral features as the VIP wavebands due to the broad bandwidths found in NIR spectra. These included 953 nm (linked to 964 nm), 1122 nm (1127 nm), 1340 nm (1323 nm), 1721 nm (1716 nm), 1869 and 1901 nm (1879 nm), 1939 nm (1945 nm), 1994 nm (2043 nm) and 2512 nm (2501 nm). The waveband at 1416 nm was closely related to the aromatic alcohol band in the VIP set (1421 nm), however 1416 nm is attributed to C–H stretching and deformation in aromatic rings, and not to the alcohol group (O–H). Of the three wavebands unique to the CovSel, two were associated with starch, namely 2097 nm (O–H deformation and C–O stretch) and 2250 nm (O–H stretch and deformation). Lastly, the band at 1574 nm (N–H stretch) is specifically related to the peptide bonds (-CONH-) linking amino acids in proteins.

All three of the reduced waveband sets resulted in decreased model performance. However, the CovSel hierarchical model gave the poorest results. A notable difference between the VIP and CovSel sets lies in the range 2250 to 2512 nm. As seen in Fig. 1, there are numerous high absorbance bands in this part of the spectrum and all the VIP windows in this region were included. These features were attributed to C–C and C–H bonds in starch and cellulose, two chemical components which contribute to large proportions of a maize kernel. It is very likely that the omission of this region from the CovSel waveband set resulted in its poor performance. The class of most concern was sound white maize, which was classified with a relatively low classification accuracy of 63% (25% decrease). Yellow maize was also classified poorly with an accuracy of 48% (27% decrease). Yellow maize was difficult to classify when the full spectrum was used. The main difference between white and yellow maize is the production of beta-carotene in yellow maize, and the pigment does not interact with NIR radiation. While the removal of redundant wavebands was expected to allow for better classification of yellow maize, this was not observed. Fortunately, pinked maize did not exhibit the same dramatic decrease in classification accuracy (3% drop) and was the only main category in which the windows and VIP hierarchical models were outperformed.

While the capacity of a human to conduct manual classification with reliably and consistently is limited (Lorente et al., 2012), the performance of the CovSel hierarchical model would not be an attractive option for the industry. The cost of building an instrument based on this set would be the cheapest, as the fewest wavebands were used. However, the loss of classification ability by removing 95% of the spectral variables was too high.

CONCLUSION

Waveband reduction and optimisation was performed for the classification of sound white maize, maize grading defects and foreign materials. Three approaches were investigated, namely the use of waveband windows, VIP scores and CovSel variable selection. All three were associated with a decrease in performance in comparison with a hierarchical model based on the full spectrum (288 wavebands). Removal of 83% of the wavebands using windows was associated with a 6% drop in classification accuracy, removal of 93% of the wavebands using VIP scores resulted in a 9% drop, and removal of 95% of the wavebands using CovSel resulted in a 11% drop.

Stellenbosch University https://scholar.sun.ac.za

The use of 48 waveband windows was effective in avoiding the need of a high-resolution spectrograph while providing good classification performance. The VIP method aimed at selecting the windows that were most relevant, and the remainder were removed. While more than half of the window bands were removed, the classification accuracy only dropped by 3%. This set of 21 wavebands is a more realistic option for industry implementation and offers better trade-off between performance and cost than the windows waveband set. Classification using the 13 CovSel wavebands resulted in decreased classification accuracy of two important main categories, sound white maize and yellow maize. While human inspection is associated with error, the number of misclassifications using the CovSel hierarchical model was too high to be a viable option for industry application.

The results of this study suggest that the following 21 wavebands be used for white maize grading according to South African legislation: 964, 1127, 1159, 1323, 1356, 1388, 1421, 1716, 1847, 1879, 1912, 1945, 2043, 2239, 2272, 2305, 2337, 2403, 2435, 2468 and 2501 nm. The performance of the hierarchical classification model based on these wavebands was good but must be improved further. Most importantly, more samples must be acquired from the maize industry to provide a more robust classification. Maize samples are very heterogenous, which leaves room for misclassification if an adequate calibration sample set is not used. Furthermore, the use of a larger sample set will allow for the application of non-linear modelling approaches, which would lead to improved classification performance. The routine application of reduced waveband spectral imaging for white maize grading is a promising option for the South African maize industry and offers high throughput and real-time results for a fraction of the price of hyperspectral imaging.

REFERENCES

Barnes, R. J., Dhanoa, M. S. & Lister, S. J. (1989). Standard normal variate transformation and de-trending of near-infrared diffuse reflectance spectra. *Applied Spectroscopy,* **43,** 772-777.

Biancolillo, A., Marini, F., & Roger, J. M. (2019). SO-CovSel: A novel method for variable selection in a multiblock framework. *Journal of Chemometrics*, e3120.

Food and Agriculture Organization (1992). Chemical Composition and Nutritional Value of Maize. In: *Maize in Human Nutrition*. Pp. 13-30. Rome, Italy: FAO.

Feng, X., Zhao, Y., Zhang, C., Cheng, P. & He, Y. (2017). Discrimination of transgenic maize kernel using NIR hyperspectral imaging and multivariate data analysis. *Sensors,* **17,** 1894.

Galvão, L. S., Vitorello, Í. & Almeida Filho, R. (1999). Effects of band positioning and bandwidth on NDVI measurements of tropical savannas. *Remote Sensing of Environment,* **67,** 181-193.

Golic, M., Walsh, K. & Lawson, P. (2003). Short-wavelength near-infrared spectra of sucrose, glucose, and fructose with respect to sugar concentration and temperature. *Applied Spectroscopy,* **57,** 139-145.

Leardi, R. & Gonzalez, A. L. (1998). Genetic algorithms applied to feature selection in PLS regression: how and when to use them. *Chemometrics and Intelligent Laboratory Systems,* **41,** 195-207.

Stellenbosch University https://scholar.sun.ac.za

Lorente, D., Aleixos, N., Gómez-Sanchis, J., Cubero, S., García-Navarrete, O. L. & Blasco, J. (2012). Recent advances and applications of hyperspectral imaging for fruit and vegetable quality assessment. *Food and Bioprocess Technology,* **5,** 1121-1142.

Metrohm AG (2019). A Technology Comparison of Near-Infrared Spectroscopy. *AZoM*. Retrieved on November 01, 2019 from https://www.azom.com/article.aspx?ArticleID=14371.

Roger, J., Palagos, B., Bertrand, D. & Fernandez-Ahumada, E. (2011). CovSel: Variable selection for highly multivariate and multi-response calibration: Application to IR spectroscopy. *Chemometrics and Intelligent Laboratory Systems,* **106,** 216-223.

Sendin, K., Manley, M. & Williams, P. J. (2018). Classification of white maize defects with multispectral imaging. *Food Chemistry,* **243,** 311-318.

Sendin, K., Manley, M., Baeten, V., Pierna, J. A. F. & Williams, P. J. (2019). Near Infrared Hyperspectral Imaging for White Maize Classification According to Grading Regulations. *Food Analytical Methods,* **12,** 1612-1624.

Su, W.H. & Sun, D.-W. (2016). Facilitated wavelength selection and model development for rapid determination of the purity of organic spelt (Triticum spelta L.) flour using spectral imaging. *Talanta,* **155,** 347-357.

Sun, J., Jiang, S., Mao, H., Wu, X. & Li, Q. (2016). Classification of black beans using visible and near infrared hyperspectral imaging. *International Journal of Food Properties,* **19,** 1687-1695.

Vigneau, E. & Thomas, F. (2012). Model calibration and feature selection for orange juice authentication by 1H NMR spectroscopy. *Chemometrics and Intelligent Laboratory Systems,* **117,** 22-30.

Wallays, C., Missotten, B., De Baerdemaeker, J. & Saeys, W. (2009). Hyperspectral waveband selection for on-line measurement of grain cleanness. *Biosystems Engineering,* **104,** 1-7.

Wang, L., Liu, D., Pu, H., Sun, D. W., Gao, W. & Xiong, Z. (2014). Use of hyperspectral imaging to discriminate the variety and quality of rice. *Food Analytical Methods*, **8**, 515-523.

Wang, L., Pu, H., Sun, D. W., Liu, D., Wang, Q. & Xiong, Z. (2015). Application of hyperspectral imaging for prediction of textural properties of maize seeds with different storage periods. *Food Analytical Methods,* **8,** 1535-1545.

Wang, L., Sun, D. W., Pu, H. & Zhu, Z. (2015). Application of Hyperspectral Imaging to Discriminate the Variety of Maize Seeds. *Food Analytical Methods,* **9,** 1-10.

Stellenbosch University https://scholar.sun.ac.za

CHAPTER 5:

DETECTION OF ASYMPTOMATIC *FUSARIUM* INFECTION IN MAIZE USING NIR HYPERSPECTRAL IMAGING

ABSTRACT

NIR hyperspectral imaging was investigated as an alternative to manual inspection for assessing maize safety regarding *Fusarium* fungal infection. Four maize samples were acquired from the Southern African Grain Laboratory after routine industry grading and mycotoxin analysis. These included two maize grade WM1 and two WM2 samples containing 1.0 to 11.1% visibly *Fusarium* damaged kernels with fumonisin levels ranging from not detected to 8 ppm (double the legal limit). 56 visibly sound kernels from each sample were imaged (224 total), placed in individual containers and germinated. Kernels with asymptomatic *F. verticillioides* infection exhibited fungal growth during germination, which was confirmed by sub-culturing and DNA analysis. While only 3.3% of kernels exhibited visible rotting symptoms (flagged during visual inspection), 32.1% of kernels were asymptomatically infected and capable of producing harmful fumonisin mycotoxins. This emphasised the need for safety testing beyond manual inspection. A PLS-DA model was calibrated using the hyperspectral image data of the visibly sound kernels that exhibited growth as one class (infected) and the kernels with no growth as another (uninfected). Unfortunately, the PLS-DA model performed poorly with an overall classification accuracy of 67.0% and a large number of errors. This was likely due to a lack in depletion of chemical components with which NIR radiation is known to interact, such as carbohydrates, proteins and moisture. While more expensive and labour intensive than spectroscopic methods, the conventional methods for mycotoxin testing (LS-MS and immunoassay methods) are recommended to accurately verify that maize is safe for human consumption.

Stellenbosch University https://scholar.sun.ac.za

INTRODUCTION

Fusarium species is a fungus ubiquitous throughout South Africa's maize growing regions. It causes two diseases that affect the quality and safety of maize kernels. The first is Fusarium ear rot, primarily caused by *F. verticillioides*, and Gibberella ear rot, caused by the *Fusarium graminearum* species complex (Munkvold, 2003). Both of these diseases produce mycotoxins that pose a serious threat to both human and animal health. Besides the obvious pathogenic state of the fungus that causes visible rotting symptoms, *Fusarium* is capable of intercellular endophytism or latent infection, where the fungus can be metabolically active without causing visible damage to the maize kernel (Kuldau & Yates, 2000). Literature indicates that the majority of *Fusarium* infected maize kernels are asymptomatic. A study by Strumpf et al. (2013) found that 58% of the maize kernels tested were *Fusarium* infected, but only 7% exhibited visible symptoms. In addition, many of these asymptomatic kernels were well over the recommended mycotoxin limits for human consumption. However, if a human grader had assessed these samples, they would have been declared safe. This study emphasised the fact that visible symptoms are not highly correlated to *Fusarium* infection or mycotoxin levels, and thus a safety control method cannot rely on the presence of visible symptoms.

Until 2016, the primary method for flagging *Fusarium* contamination in South African maize consignments was visual inspection, which takes place during maize grading. However, there is one major issue with this method. *Fusarium* infections take place from within the maize kernel, not at the surface, and mycotoxins may be produced without the kernel developing any visible symptoms. New legislation has been introduced that limits fumonisin content in maize to 4 ppm. However, current mycotoxin testing methods are expensive and require a large amount of sample preparation. There has been resistance from the industry to test every consignment of maize for mycotoxins, which was previously done voluntarily and at random. As fumonisins cannot be produced in the absence of *Fusarium* infection, an accurate method for flagging both symptomatic (visibly rotten) and asymptomatic (visibly healthy) *Fusarium* infections would ensure that samples be sent for expensive mycotoxin testing only when necessary.

NIR spectroscopy is an analytical technique that utilises non-visible wavebands, and thus has the potential to detect properties of a sample that are not visible to the human eye. By spatially resolving this spectral information, spectral imaging easily allows the study of individual kernels in a single scan as opposed to a bulk measurement. NIR hyperspectral imaging has been used to differentiate visibly *Fusarium* damaged kernels from sound maize kernels with a classification accuracy of 100% in Chapter 3. Furthermore, the technique has been used to track changes in white maize kernels artificially surface inoculated with *F. verticillioides* (Williams et al., 2012). The technique was able to detect changes during infection onset before symptoms were visibly observable. It has not yet been investigated whether the technique is capable of detecting the infection when internally inoculated, as would occur naturally during commercial maize production.

The aim of this study was to establish if NIR hyperspectral imaging was capable of differentiating between uninfected white maize kernels and asymptomatic *Fusarium* infected white maize kernels. The kernels were germinated to establish which were infected and uninfected, which allowed an investigation into the correlation between white maize grade, visible *Fusarium* infection, asymptomatic *Fusarium* infection and

Stellenbosch University https://scholar.sun.ac.za

mycotoxin levels. The images of kernels with asymptomatic *Fusarium* infection were differentiated from the uninfected kernels using a PLS-DA classification model based on the pregermination hyperspectral images acquired before germination.

MATERIALS AND METHODS

Brief overview

Maize kernels which appear healthy to the human eye were imaged using a NIR hyperspectral imaging system. Each kernel was coded, imaged and placed in a marked sterile container. Each kernel was germinated, causing *Fusarium* fungus inside a kernel to grow out and become visible. This revealed which kernels were uninfected and which kernels were internally infected with *Fusarium*. As each kernel was assigned a code, the images of the kernels acquired pre-germination could be divided into two classes, namely the uninfected and infected kernels. Object-wise PLS-DA classification was used to separate the two classes. Conventional confirmation of the observed fungal species and mycotoxin analysis were conducted to further support these findings.

Samples

White maize kernels were obtained from the Southern African Grain Laboratory (SAGL, Pretoria, South Africa) in June, 2019. Four bulk white maize samples with varying fumonisin levels, *Fusarium* damage and grade were provided namely: (1) Control sample: no fumonosins detected, no visibly *Fusarium* damaged kernels, white maize grade 1 (WM1); (2) Sample 322: 4 ppm fumonisins, 1% visibly *Fusarium* damaged kernels, WM1; (3) Sample 104: 7 ppm fumonisins, 11% visibly *Fusarium* damaged kernels, WM2; and (4) Sample 351: 8 ppm fumonisins, 1% visibly *Fusarium* damaged kernels, WM2.

These bulk samples were silo samples, meaning that they are of mixed origin, cultivar and harvested from the 2017/18 season. All samples selected for imaging and germination were visibly uninfected (healthy, undamaged appearance) and suitable for human consumption according to expert graders in accordance with the South African grading regulations (Act, 2009). The bulk samples for mycotoxin analysis contained all kernels, including visibly damaged kernels where applicable.

As the true *Fusarium* infection status (healthy or infected) of the asymptomatic maize kernels was unknown at the start of the experimental process, a large sample size was used to ensure a representative number of samples in each class. In total, 224 white maize kernels were used. This included 28 kernels from each of the four maize samples for calibration and 28 for validation (56 kernels from each sample). Samples were surface sterilised in 70% ethanol solution for 30 seconds. This treatment was sufficient to remove all surface microbial contamination without risk of penetrating the maize kernel's hard, dry exterior.

NIR hyperspectral system

See Chapter 3 for NIR hyperspectral imaging system details.

Stellenbosch University https://scholar.sun.ac.za

Image acquisition

A total of eight images were acquired, namely two images of 28 kernels for each of the four samples. The eight images were coded as A – H, and samples were arranged in a grid of seven columns and four rows. Image A and B were of the control sample, C and D of sample 322, E and F of sample 104, and G and H of sample 351. In image A, the kernel from column 1 and row 1 was assigned code A1, and so on (Fig. 1). A digital photograph was taken, followed by hyperspectral image acquisition. Each maize kernel was transferred to a small, sterile plastic container marked with the kernel's reference code (Fig. 1).

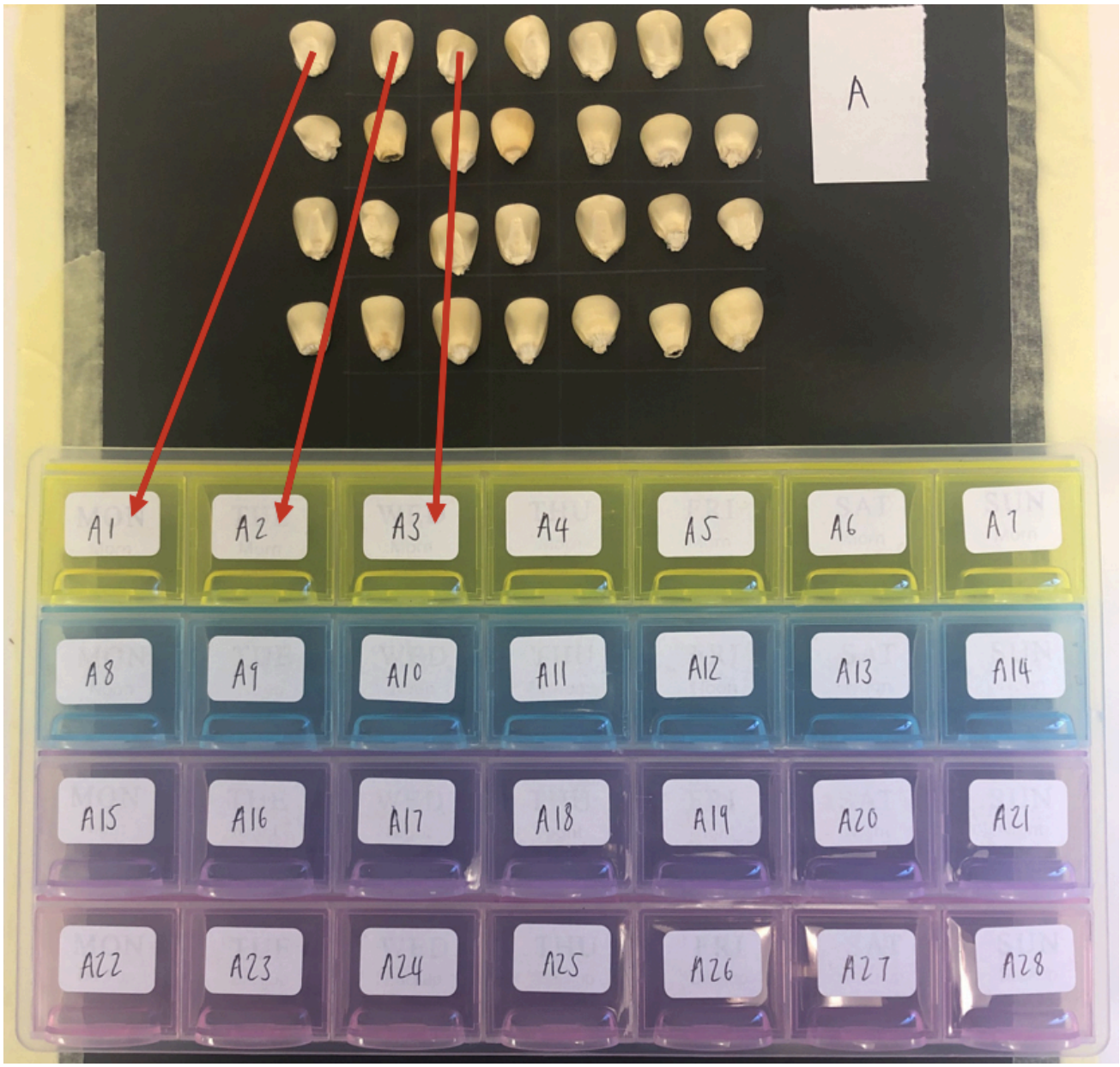

Figure 5.1 Maize kernels were arranged in eight grids of 28 kernels each for imaging and transferred to labelled containers for germination.

Stellenbosch University https://scholar.sun.ac.za

Maize kernel germination

Individual maize kernels were germinated by placing the kernel on sterile cotton wool moistened with distilled water. Containers were stored in a dark room at ambient temperature (*ca.* 21 °C) for 4 days when germination was observed. In the case of asymptomatic *Fusarium* infection, the fungus grew from the kernel during germination and was observed as brown discolouration of the maize kernel with mould growth on the cotton wool. These kernels formed the study's 'infected' class. The uninfected kernels maintained a healthy white appearance and formed the 'uninfected' class. The reference code of each uninfected and infected kernel was noted.

Verification of Fusarium sp. infection

Non-selective growth media

All maize kernels that exhibited fungal growth were placed on potato dextrose agar media in individual petri dishes. The petri dishes were incubated at 25 °C for five days. The resulting fungal growth was examined by a highly experienced plant pathologist to confirm *Fusarium* spp. presence.

DNA extraction and confirmation

The germinated maize kernels were milled and passed through a 1-mm mesh using a Cyclotech sample mill (Foss Tecator, Hoganas, Sweden). DNA was isolated using a commercial kit and protocol described by Boutigny et al. (2012) which utilised a DNeasy® Plant Mini kit (QIAGEN) in combination with the CTAB/PVP lysis method. 10 mL CTAB/PVP lysis buffer [0.1 M Tris, 1.4 M NaCl, 0.02 M EDTA, 2% CTAB (w/v), 1% PVP (w/v) pH 8.0] and 40 µL proteinase K (10 mg mL^{-1}) were added to each sample. The samples were placed in an incubator shaker (Labcon, USA) at 65°C for 2 hrs with shaking at 200 rpm, followed by centrifugation for 10 min at 4000 rpm at 25°C. 1 mL of the supernatant was transferred to a sterile 1.5 mL tube and 30 µL RNAse (10 mg mL^{-1}) was added. The samples were incubated at 65°C for 15 min and centrifuged for 10 min at 12000 rcf. The supernatant (*ca.* 400 µL) was transferred to a 1.5 mL tube. A NanoDrop ND-1000 Spectrophotometer (Inqaba Biotechnical Industries (Pty) Ltd., Pretoria, South Africa) was used to verify the quantity of the DNA and the purity of the DNA was evaluated by comparing absorbance ratios at 260 and 280 nm, and 260 and 230 nm. Good quality DNA was diluted to a concentration of 10 ng $µl^{-1}$ for the detection and absolute quantification of *F. verticillioides* in the maize samples using quantitative real-time polymerase chain reaction (qRT-PCR). The qRT-PCR assays included one replicate of each maize sample, a negative control containing no template DNA, and a standard pathogen DNA that was diluted 16-fold in maize DNA (10 ng $µl^{-1}$) free of *F. verticillioide*s infection. The *F. verticillioides* isolate MRC 826 was used for the DNA standard. Regression equations to detect *F. verticillioides* in the maize samples were highly significant ($R^2 > 0.99$).

Mycotoxin analysis

Fumonisin levels were determined by the SAGL during their routine analysis of white maize samples for their annual maize crop quality survey. The inhouse LC-MS/MS method is accredited for the analysis of multi-

Stellenbosch University https://scholar.sun.ac.za

mycotoxins in grain, cereals and related feed samples according to ISO 17025 by the South African National Accreditation System (SANAS) (Meyer et al., 2019).

A bulk sample of the ungerminated kernels from all samples (control, 322, 104 and 351) were tested. The maize kernels were milled with a Retsch ZM 200 mill with a 1-mm sieve and were thoroughly mixed, as mycotoxins are heterogeneously dispersed in the grain. A 10 g sub-sample of the milled maize was blended with 40 ml of the extraction fluid (50:25:25 H_2O:MeOH:AcCN (v/v)). The blended sample was transferred to a centrifuge tube, extracted for 15 min on a mechanical shaker and centrifuged at 3000 rpm for 10 min. A 5 mL aliquot was mixed with 5 mL of the dilution solution (25% MeOH in H_2O (v/v)) and filtered through 13 mm 0.22 µm syringe filters (Nylon, Membrane Solutions) into HPLC amber vials.

An ultra-performance liquid chromatograph (Waters Acquity UPLC) equipped with a C_{18} column (Acquity BEH, 1.7 µm, 50 × 2.1 mm i.d.) at 30 °C was used. A reverse phase chromatographic separation of 13 mycotoxins (including fumonisins B_1, B_2 and B_3) was performed with a programmed gradient elution of water containing 0.5 mM ammonium acetate and 0.1% formic acid (mobile phase A) and acetonitrile with 0.1% formic acid (mobile phase B) at a column flow rate of 0.4 mL and a run time of 15 min. A Waters tandem quadrupole mass spectrometer (Acquity TQD) equipped with an ESI source operating in positive ionization mode (ESI+) was used. The optimised TQD parameters were source temperature of 120 °C, desolvation temperature of 500 °C, nitrogen gas flow of 650 L/hour and cone gas flow of 50 L/hour. Argon was used as collision gas in the collision cell. The cone voltages and collision energy values were optimised for each precursor ion, where the M+1 ions were used. One precursor ion and two product ions (MRMs) were optimised, selecting one product ion for quantification, and a second one for confirmation of the compound. Matrix-matched working standards of the 13 mycotoxins, including fumonisins, were prepared regularly for the calibration of the LC-MS/MS.

Hyperspectral image analysis

Image correction, cleaning and particle analysis

See Chapter 3 for image correction, cleaning and particle analysis methods.

Partial least squares discriminant analysis

PLS-DA classification models were used to distinguish between two classes, namely ‘uninfected’ and ‘infected’. This was achieved by sorting image objects (kernels) in the pre-germination images into classes according to their germination result and assigned code. Calibration and validation sets consisted of images A, B, C and D for calibration and B, D, F and H for validation, i.e. one image of each sample for calibration and one for validation. Object-wise PLS-DA models were calculated with full cross-validation. The mean spectrum of all pixels in an object was used during object-wise analyses. The PLS-DA models were applied to the validation image data, and a classification image was generated.

Classification accuracy, false positive error, and false negative error were calculated according to Eq. 1, 2 and 3, respectively. An ‘infected’ classification was a positive response and a ‘uninfected’ classification was a negative response. A false positive occurred when an uninfected kernel was incorrectly classified as

Stellenbosch University https://scholar.sun.ac.za

infected, and a false negative was when an infected kernel was incorrectly classified as uninfected.

$$\text{Classification accuracy (\%)} = \frac{\text{Correct Infected + Correct Uninfected}}{\text{Total}} \times 100\% \quad (5.1)$$

$$\text{False positive error (\%)} = \frac{\text{False Positives}}{\text{Total}} \times 100\% \quad (5.2)$$

$$\text{False negative error (\%)} = \frac{\text{False Negatives}}{\text{Total}} \times 100\% \quad (5.3)$$

Where:

Correct Infected = Correctly classified class 'Infected' kernels

Correct Uninfected = Correctly classified class 'Uninfected' kernels

False Positives = 'Uninfected' class kernels incorrectly classified 'Infected' class

False Negatives = 'Infected' class kernels incorrectly classified 'Uninfected' class

Total = Sum of 'Infected' and 'Uninfected' kernels

Sensitivity and Specificity were calculated according to Eq. 4 and 5, respectively. The sensitivity describes the probability that infected kernels will be detected and correctly classified and is sometimes described as the true positive rate. Specificity is the probability that an uninfected kernel will be classified correctly, also known as the true negative rate.

$$\text{Sensitivity (\%)} = \frac{\text{Correct Infected}}{\text{Total Infected}} \times 100\% \quad (5.4)$$

$$\text{Specificity (\%)} = \frac{\text{Correct Uninfected}}{\text{Total Uninfected}} \times 100\% \quad (5.5)$$

Where:

Correct Infected = Correctly classified class 'Infected' kernels

Correct Uninfected = Correctly classified class 'Uninfected' kernels

Total infected = Total 'Infected' kernels (Correct Infected + False Negatives)

Total Uninfected = Total 'Uninfected' kernels (Correct Uninfected + False Positives)

RESULTS AND DISCUSSION

Fusarium symptoms, infection and fumonisin content

Four samples with a known percentage visibly *Fusarium* damaged (symptomatic) kernel content, grade and fumonisin content were germinated to reveal rates of asymptomatic *Fusarium* infection (Table 1). Visibly fungal damaged kernels were present in three of the four samples, ranging 1.0 to 11.1%. The incidence of asymptomatic infection was far higher and ranged 3.4 to 66.1%. Of the 224 visibly sound samples germinated, 71 (31.7%) were asymptomatically infected. All 71 infected kernels were sub-cultured and characteristic *Fusarium verticillioides* growth was observed. DNA sequencing analysis confirmed that all instances were linked to *F. verticillioides*. *F. verticillioides* is capable of colonising a maize plant and invade kernels without causing symptoms (e.g. discolouration or rotting), which explains the lack of correlation between *Fusarium* damaged kernel content and overall *Fusarium* incidence (Munkvold, 2003; Strumpf et al., 2013). The samples with the

Stellenbosch University https://scholar.sun.ac.za

lowest amount of *Fusarium* damaged kernels and fumonisin levels, namely the control sample (0% and ND, respectively) and 322 (1.0% and 4ppm, respectively), had the highest instance of asymptomatic *Fusarium* infection. Conversely, the sample with the highest number of visibly rotten kernels had little asymptomatic infection. These results illustrate that the presence of symptoms is not a reliable indication of *Fusarium* risk.

The bulk maize samples were graded according to South African legislation, where *Fusarium* fungal damaged kernels are classed as defective kernels. The limits for the defective kernel category are <8% for WM1 (best grade), <16% for WM2 and <30% for WM3. All samples were found to be safe for human consumption according to the visual inspection method, with two of the samples (control and 322) graded as WM1 and the remaining two (104 and 351) as WM2. While sample 351 had a Fusarium damage content of only 1.1%, the sample contained other defects which gave a total defective kernel content above 8%. No WM3 (lowest grade) samples were used, as this grade is only fit for animal feed. Mycotoxin levels were measured for the four samples (control, 322, 104 and 351) using bulk samples that consisted of sound, symptomatic and asymptomatic kernels. Levels of fumonisins varied from not detected (ND) to 8 ppm (Table 1), and these levels were not correlated to the incidence of visible damaged kernels. Thus, while all samples were deemed fit for human consumption using the manual inspection method, two of the four maize samples were found to be unsafe when tested for fumonisins.

Sample 322 contained a small amount of visibly damaged kernels (1.0%) but exhibited an incredibly high asymptomatic infection rate of 66.1%. This high level of overall infection contributed to a fumonisin content at the threshold of safe human consumption (4 ppm), according to South African legislature. Unexpectedly, the overall infection rate of samples 104 and 351 were lower than the others despite containing unsafe levels of fumonisins (7 and 8 ppm, respectively). Previous studies have established that *Fusarium* can be present in a maize plant as early as the seedling stage in a symptomless or endophytic state. This state continues throughout plant development without any visual signs of infection and contributes to mycotoxin contamination before and during kernel development (Bacon & Hinton, 1996). Although behaving asymptomatically, the hyphae of endophytic *F. verticillioides* are not dormant, particularly in the early stages of seedling infection, and this metabolic activity has been linked to the accumulation of the fumonisins (Kuldau & Yates, 2000). While the production of fumonisins does lead to increased virulence of *F. verticillioides*, it is not necessary for disease development (Munkvold & Desjardins, 1997). Thus, *F. verticillioides* infection can occur with any possible combination of symptomatic/asymptomatic appearance and fumonisin absence/contamination.

The control sample was intended as a *Fusarium* free control, as it showed no instance of visible *Fusarium* infection and fumonisins were not detected. However, this sample had unexpectedly high levels of asymptomatic infection upon germination (41.1%). It is likely that these kernels were infected by *Fusarium* spores, e.g. due to field infection, but conditions did not favour the proliferation of the fungus nor the production of mycotoxins. Despite the presence of fungal spores, which proliferated upon germination, this maize sample was fit for human consumption as there was no fungal damage (quality control) and mycotoxins were not

Stellenbosch University https://scholar.sun.ac.za

detected (safety). The findings of the germination study emphasise that there is little correlation between *Fusarium* symptoms, *Fusarium* infection and fumonisin production.

Table 5.1 The details of the maize samples used, including grade (WM1 = human grade (best); WM2 = human grade; WM3 = animal grade), percentage *Fusarium* damaged (symptomatic) kernels, asymptomatic kernels and fumonisin content.

	Grade	Symptomatic infection (%)	Asymptomatic infection (%)	Total infection (%)	Fumonosins (ppm)	Unsafe (<4ppm)
Control	WM1	0.0	41.1	41.1	ND	No
322	WM1	1.0	66.1	67.1	4	No
104	WM2	11.1	3.6	14.7	7	Yes
351	WM2	1.1	17.9	19.0	8	Yes
OVERALL	**-**	**3.3**	**32.1**	**35.4**	**-**	**-**

NIR hyperspectral imaging for detection of asymptomatic Fusarium infection

The germination results were used to group the hyperspectral images taken prior to germination into classes of infected (*Fusarium* growth) and uninfected (no *Fusarium* growth) kernels. A PLS-DA model was calibrated using one image of each sample group (Control - Image A; 322 – Image C; 104 – Image E; 351 – Image G) and validated using one image of each (Control - Image B; 322 – Image D; 104 – Image F; 351 – Image H). The validation samples, which comprised 24.1% *Fusarium* infected and 75.9% uninfected kernels, were classified with an accuracy of 67.0% (Table 2). False positives (uninfected misclassified as infected) occurred more frequently than false negatives (infected misclassified as uninfected), but this was likely due to the larger proportion of uninfected kernels. An overall sensitivity of 43.8% and specificity of 64.8% were achieved, where the sensitivity is the ability of the model to flag infected kernels and the specificity pertains to correct classification rate of the healthy kernels. This indicates that while the model could generally find a kernel without *Fusarium* infection, it was often not capable of identifying asymptomatic *Fusarium* when present. This is likely due to the varying degrees of *Fusarium* infection present in the sample group, where each kernel has an individual degree of fungal proliferation while in the endophytic state. Although a spore may be present within the kernel, which gave rise to fungal growth upon germination, the fungus may have remained completely dormant. In these cases, there was no depletion of the chemical constituents that gave rise to a measurable NIR spectrum.

The classification accuracy ranged broadly, namely 39.3% for sample 322 (4 ppm fumonisins), 64.3% for the control (0 ppm), 85.7% for sample 104 (8 ppm) and 92.9% for sample 351 (7 ppm). There appeared to be a trend of increased prediction accuracy with higher fumonisin content, which could be used as an indicator for degree of fungal proliferation. Considering that the infected and uninfected classes were visually identical and showed no signs of fungal damage, the classification results of samples 104 and 351, which were not safe for human consumption, were impressive. However, an alternative explanation is that these two samples contained low proportions of infected kernels. As discussed, the specificity of the models was higher due to

Stellenbosch University https://scholar.sun.ac.za

better prediction of the healthy kernels, and the samples with a large number of uninfected kernels performed with higher classification accuracy.

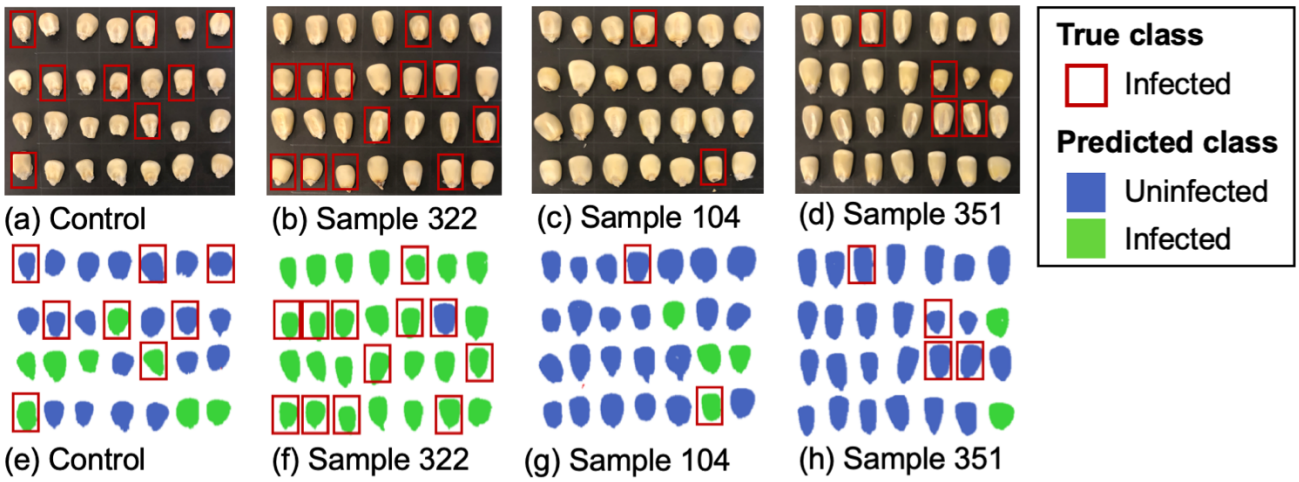

Figure 5.2 Digital images of the samples, with asymptomatically infected kernels indicated by a red square, specifically (a) control sample (image B), (b) sample 322 (image D), (c) sample 104 (image F), and (d) sample 351 (image H). Classification images with kernels predicted as uninfected in blue and infected in green, specifically (e) control sample (image B), (f) sample 322 (image D), (g) sample 104 (image F), and (h) sample 351 (image H).

Table 5.2 Validation results for the PLS-DA classification of asymptomatically *Fusarium* infected and uninfected white maize kernels

	Infected (positive) (%)	Uninfected (negative) (%)	Classification accuracy (%)	False positives (%)	False negatives (%)	Sensitivity (%)	Specificity (%)
Control	32.1	67.9	64.3	17.9	17.9	33.3	78.9
322	42.9	57.1	39.3	57.1	3.6	91.7	0.0
104	7.1	92.9	85.7	10.7	3.6	50.0	88.5
351	14.3	85.7	78.6	7.1	14.3	0.0	91.7
OVERALL	**24.1**	**75.9**	**67.0**	**23.2**	**9.8**	**43.8**	**64.8**

Shortcomings of NIR hyperspectral imaging for asymptomatic Fusarium detection

While a study generally aims to highlight the promise of a technique, in this case NIR hyperspectral imaging, it is often equally important to understand the limitations. Fig. 2 revealed that classification by the PLS-DA model was erratic and random, and a large number of *Fusarium* infected kernels were not detected. The most likely reason is that the *Fusarium* fungus had not depleted the chemical components in the kernel with which NIR radiation interacts. When *Fusarium* is in an endophytic state, the hyphae can be active, or be less developed and even absent. In fact, this can vary to a large extent depending on a wide variety of biotic and abiotic factors. The injury to the kernel caused due to absorption of intercellular nutrients in the apoplasm is not as severe when these specialised intracellular absorbing hyphae are less numerous. Without sufficient nutrients, both primary and secondary metabolism is stunted (Bacon, 2008).

Stellenbosch University https://scholar.sun.ac.za

The most prominent bands seen during NIR analyses are due to overtones of stretching vibrations and stretching-bending combinations involving major X–H bonds (Ozaki et al., 2006). Thus, differences between components containing O–H bonds (e.g. moisture, carbohydrate and fat), C–H bonds (most organic compounds), N–H bonds (e.g. proteins and amino acids) and S–H bonds (e.g. proteins and amino acids) should be present in order to separate objects based on an NIR signature. Specifically, a previous study of artificial surface inoculation of *F. verticillioides* on white maize found that fungal proliferation caused differences in absorption at 1405 nm (associated with starch), 1660 – 1668 nm (associated with an aromatic structure), 1900 nm (associated with starch) and 2136 nm (associated with protein) (Williams et al., 2012). Furthermore, the study found that the inoculated kernels required an incubation in ideal growth conditions (28 °C) for a minimum of 20 hours before sufficient proliferation took place to calibrate a reliable PLS-DA classification model. The *Fusarium* infected samples used in the current study were naturally occurring internal infections (not surface inoculations) and had not been incubated. If the kernels had not grown in environmental conditions that was optimal for *F. verticillioides* proliferation (e.g. hot and dry conditions, particularly after flowering), then it is likely that chemical composition of the infected kernels remained unaltered, and thus undetectable by NIR spectral imaging.

Despite the fumonisin levels of the calibration samples being known, classification of samples according to *Fusarium* infection was chosen over regression of fumonisin content. While it may seem that detecting fumonisin levels directly would be more in line with the maize industry's needs, this was not a viable option. It is generally accepted that NIR spectroscopic data cannot be used to detect contaminants at the levels at which mycotoxins occur, although some studies claim to have done so (e.g. 10 ppm aflatoxin B1 by Wang et al. (2014)). NIR spectroscopy is not a trace analytical method and can be considered inappropriate for detection of trace amounts beyond the low percentage range (0.1% or 1000 ppm) (Bart et al., 2012). In favourable cases, slightly higher sensitivity can be expected in liquid media (0.01% or 100 ppm). This limitation in sensitivity is due to the relatively low intensity of excitation occurring in the NIR region. The technique relies on overtones and combinations thereof that occur less frequently than other interactions with higher energy frequencies of radiation (e.g. fundamental vibrations from infrared). This leads to broad, flat bands that have a relatively low signal-to-noise ratio (SNR). Thus, one of the greatest challenges in NIR spectroscopy is collecting enough signal to achieve adequate SNR, and this is often not possible at low concentrations where little absorption occurs. Mycotoxin levels in the order of 1 ppm (0.0001%) must often be detected to ensure safety for human consumption. Thus, this study rather opted to detect the presence of *Fusarium* fungus using NIR spectral imaging instead of attempting to predict these trace levels of fumonisins. However, the results of this study suggest that NIR hyperspectral imaging is not suitable for the detection of asymptomatically *Fusarium* infected kernels based on changes in major chemical components.

CONCLUSION

The germination of visibly healthy maize kernels revealed a large proportion of asymptomatically *F. verticillioides* infections. This was due to the ability of the fungus to exist in an endophytic state, as opposed to

Stellenbosch University https://scholar.sun.ac.za

the more commonly studied pathogenic state. The average symptomatic infection rate was only 3.3%, while the asymptomatic rate was 32.1%. Furthermore, there was no clear trend between high infection rates and fumonisin content. The germination results emphasised the lack of correlation between *F. verticillioides* infection, Fusarium ear rot symptoms and fumonisin content. This demonstrated that visual inspection for visible rotting symptoms is not sufficient for ensuring the safety of maize consignments. Fumonisins cannot be produced without *Fusarium* infection and a hyperspectral imaging method was investigated for identifying asymptomatic infections, as symptomatic infections were detected with a classification accuracy of 100% in Chapter 3 of this thesis. An unacceptably low overall classification accuracy of 67.0% was achieved for detection of asymptomatic infection due to a low sensitivity for detecting the asymptomatic infection in some kernels. This was likely due to the low metabolic activity of the fungus in the endophytic state, which caused little difference in chemical composition between the some of the infected and uninfected maize kernels. Despite the presence of mycotoxins in the absence of symptoms, it is not recommended that an NIR spectroscopy-based technique be used to detect trace levels of mycotoxins due to the technique's limited sensitivity. However, the *Fusarium* germination aspect of this study provided insight into the status of *Fusarium* infection and fumonisins in the South African maize industry that have not yet appeared in literature. Established LC-MS and immunoassay techniques should be implemented for testing all maize consignments until a more industry friendly alternative is found, due to the serious implications of fumonisins to human health.

REFERENCES

Bacon, C. & Hinton, D. (1996). Symptomless endophytic colonization of maize by Fusarium moniliforme. *Canadian Journal of Botany,* **74,** 1195-1202.

Bart, J. C., Gucciardi, E. & Cavallaro, S. (2012). Quality assurance of biolubricants. In: *Biolubricants: science and technology*. Pp. 396-450. Cambridge, UK: Elsevier.

Kuldau, G. A. & Yates, I. E. (2000). Microbial endophytes. In: *Evidence for Fusarium Endophytes in Cultivated and Wild Plants* (edited by Bacon, C. W. & White, J.). Pp. 85-120. New York City, USA: CRC press.

Meyer, H., Skhosana, Z. D., Motlanthe, M., Louw, W., & Rohwer, E. (2019). Long Term Monitoring (2014–2018) of Multi-Mycotoxins in South African Commercial Maize and Wheat with a Locally Developed and Validated LC-MS/MS Method. *Toxins,* **11**, 271.

Munkvold, G. P. (2003). Epidemiology of Fusarium diseases and their mycotoxins in maize ears. *European Journal of Plant Pathology,* **109,** 705-713.

Munkvold, G. P. & Desjardins, A. E. (1997). Fumonisins in maize: can we reduce their occurrence? *Plant disease,* **81,** 556-565.

Stumpf, R., Santos, J. d., Gomes, L. B., Silva, C., Tessmann, D. J., Ferreira, F., Machinski Junior, M. & Del Ponte, E. M. (2013). Fusarium species and fumonisins associated with maize kernels produced in Rio Grande do Sul State for the 2008/09 and 2009/10 growing seasons. *Brazilian Journal of Microbiology*, **44,** 89-95.

Stellenbosch University https://scholar.sun.ac.za

Williams, P. J., Geladi, P., Britz, T. J. & Manley, M. (2012). Investigation of fungal development in maize kernels using NIR hyperspectral imaging and multivariate data analysis. *Journal of Cereal Science,* **55,** 272-278.

Stellenbosch University https://scholar.sun.ac.za

CHAPTER 6:
GENERAL DISCUSSION AND CONCLUSION

NIR hyperspectral imaging was investigated as a potential analytical technique to address two important needs of the South African white maize industry, namely white maize grading and the detection of mycotoxigenic *Fusarium* infections. Maize is South Africa's most important grain crop and is grown widely in many parts of the country. While hyperspectral imaging has a high initial investment cost, white maize is of huge economic importance and improvements in processing have far-reaching effects that could justify this hefty price tag.

Maize grading is used to determine the price of maize throughout the market value chain. The current manual inspection method requires a human grader to sample 150 g of a maize consignment (*ca.* 1000 maize kernels), spread the kernels out on a work bench and visually identify any kernel that is not sound (healthy). A human grader can be easily overwhelmed during this process and achieving a reproducible and accurate result is unlikely (Lorente et al., 2012). Automation of this process would avoid the error associated with human sorting and fatigue, and allow for higher throughput and larger bulk samples. While conventional computer imaging has been successfully and cheaply implemented in simple applications throughout the food industry, these systems are not capable of completing complex tasks such as sorting closely related samples. NIR hyperspectral imaging is a more suitable analytical technique for maize grading automation, as it uses radiation that interacts widely with the chemical components of a maize kernel (Sendin et al., 2018).

The South African maize grading regulations require the classification of 5 main categories, which can be further classified into 17 sub-categories. Separating this large number of classes is unusual in NIR hyperspectral imaging studies, which usually focus on 2 to 5 classes. To overcome this issue, the complex task was broken down to simple binary steps that were assembled in a single hierarchical decision pathway. This decision pathway first sorted the most easily separated classes and gradually proceeded to the most closely-related classes. For this reason, the maize kernels and foreign materials were separated in the first step. The maize kernels were sorted at the next decision point in the following order: screenings, heat damage, *Fusarium* fungal damage, immature kernels, water damage, *Diplodia* fungal damage, yellow maize, sound white maize, sprouted maize, frost damage, pinked white maize and pest damage. The foreign materials were sorted into cellulose-rich (sunflower seeds and plant material) and starchy (sorghum, soy beans and wheat) groups, and then simply classified by a binary and ternary PLS-DA model, respectively. The hierarchical model classified the kernels according to their full mean spectrum with an overall accuracy of 93.3% for the main categories (5 classes) and 75.5% for the sub-categories (17 classes). A large number of the sub-category errors were due to one defect being misclassified as another, as many kernels have undergone the onset of more than one defect. The legislation simply requires a grader to identify a defective kernel (main category) and the specific defect (sub-category) does not need to be identified when assigning the grade. Thus, instances in which the automated system and human grader did not agree will not affect the overall accuracy. While the accuracy of human grading is difficult to determine and accurately compare with an alternative method, the performance of the NIR

Stellenbosch University https://scholar.sun.ac.za

hyperspectral imaging method was impressive. However, some classes were classified more accurately than others. The classification of sound white maize (88.3%), pinked white maize (83.3%) and yellow maize (75.0%) should ideally be improved before the method is implemented for industry grading. This could be achieved by expanding the calibration data set to allow for a more robust model, or by including visible wavebands as spectral variables. Pinked white maize and yellow maize are distinguishable due to the presence of anthocyanin and beta-carotene, respectively, which both exhibit maximum absorption in the visible region and do not interact with NIR radiation. Thus, a hyperspectral camera operating in the NIR region cannot detect these pigments that are obvious to a human grader's eye. Unfortunately, the instrument used in this study did not include the visible region.

Following the encouraging success of maize grading using the full NIR spectrum, waveband reduction and optimisation was conducted to establish if a spectral imaging solution could be provided to the South African maize industry at a lower cost. Furthermore, a system that acquires a smaller dataset would potentially operate more quickly. Three approaches to waveband selection were investigated, namely waveband windows, VIP waveband selection and CovSel waveband selection. The waveband windows approach simply reduced the number of spectral variables from 288 to 48 only selecting every sixth waveband from the full spectrum. As NIR spectra are associated with broad, flat spectral features that tend to span a large number of wavebands, all of the major features were included when the waveband spacing was increased from 5.45 nm to 32.7 nm. The main category classification dropped from 93.3% for the full spectrum model to 87.1% for the windows hierarchical model based on 16.7% of the spectral variables. The decreased accuracy was consistent across the main categories, although yellow maize suffered a considerable drop to 60% classification accuracy. VIP scores were calculated to identify the wavebands with the highest weighting throughout the individual PLS-DA models in the hierarchical model and 21 wavebands were selected. This hierarchical model performed with similar main category classification accuracies in comparison with the windows model, despite using only 7.3% of the spectral variables. An overall main category classification of 84.5% was achieved. CovSel is a complex waveband optimisation algorithm that selects wavebands based on the co-variance between the **X**- and **y**-data. The algorithm identified a set of 13 wavebands (4.5% of the spectral variables) and achieved an overall main category classification of 81.9%. This waveband set selected few wavebands in the range 2250 to 2512 nm, which was an important region for the classification of many of the white maize classes. The further loss of model performance from the VIP and to the CovSel hierarchical model was largely attributed to this omission. In this attempt to offer the industry a simple and affordable option, a trade-off between performance and price was unavoidable. Considering the results of all three waveband reduction and optimisation approaches, the 21 wavebands selected based on VIP scores (964, 1127, 1159, 1323, 1356, 1388, 1421, 1716, 1847, 1879, 1912, 1945, 2043, 2239, 2272, 2305, 2337, 2403, 2435, 2468 and 2501 nm) are recommended for white maize grading using reduced waveband spectral imaging.

This study addressed a second issue in the South African maize industry, namely the detection of asymptomatic *Fusarium* infections. Until very recently, the industry relied solely on the manual grading process to flag maize consignments with unacceptably high levels of *Fusarium* infection. However, *Fusarium* can infect

Stellenbosch University https://scholar.sun.ac.za

a maize kernel and produce harmful fumonisin mycotoxins without causing visible damage. These infections are referred to as asymptomatic and are attributed to the fungus's ability to exist in an endophytic state in addition to the more commonly known pathogenic and saprophytic states (Bacon et al., 2008; Kuldau & Yates, 2000). Legislation was introduced in 2016 that stipulated a maximum fumonisin level of 4 ppm, which necessitates the regular use of expensive analytical testing. As maize producers are reluctant to implement these new changes, this study investigated a spectral imaging method to flag maize consignments with asymptomatic *Fusarium* infected white maize kernels, as mycotoxins can only be produced if kernels are infected. Maize kernels with symptomatic *Fusarium* infection were already detected with 100% classification accuracy in the grading section of this project. Maize consignments free from symptomatic and asymptomatic *Fusarium* infections are not at risk of containing dangerous levels of fumonisins. NIR hyperspectral images of 224 visibly sound (healthy) kernels were acquired prior to germination of the kernels in individual sterile containers. Germination caused internal *Fusarium* infections to become visibly identifiable as external fungal growth. The fungal growth from all of the kernels was confirmed to be *F. verticillioides* by further conventional microbial testing. The results revealed that while only 3.3% of the kernels in the bulk samples exhibited visible rotting symptoms (flagged during visual inspection), 32.1% of germinated kernels were asymptomatically infected and capable of producing harmful fumonisin mycotoxins. Some of these bulk samples contained fumonisin levels of 8 ppm (double the limit) but would have been declared safe for human consumption if only manual inspection had been conducted. This lack of correlation between visible symptoms and safety emphasised the need for additional analytical methods to determine *Fusarium* related risks. The pre-germination spectral images of the uninfected and asymptomatically infected kernels were divided into two classes and used to calibrate and validate (50:50) a PLS-DA classification model. The model performed with an overall classification accuracy of 67.0% and exhibited better specificity than sensitivity. Simply, some of the infected kernels were not sufficiently altered by the fungal infection to allow for detection using NIR hyperspectral imaging. Considering the high food safety risk associated with fumonisins, NIR hyperspectral imaging is not a viable method for detecting asymptomatic *Fusarium* infections during South African white maize processing.

While more complex chemometric methods were available, further attempts to improve the results in this project were avoided. When processing spectroscopic data, there is often a temptation to use every available data analysis tool to generate impressive results in the isolation of a study. However, this can lead to poor robustness of the system when applied in a practical setting as models become over-fitted. For example, non-linear methods were not explored in this study as the calibration sample sizes (60 per class for the grading studies; 112 for asymptomatic *Fusarium* study) were too small. These techniques, including support vector machines (SVM), artificial neural networks (ANN) and back-propagation neural networks (BPNN), have become increasingly popular in NIR hyperspectral imaging studies, as well as in conventional NIR spectroscopy (Sendin et al., 2018). It is generally accepted that applications involving extremely heterogenous agricultural samples (e.g. maize kernels) require hundreds or even thousands of samples to calibrate a non-linear model without over-fitting. It must be noted that the pixel spectra in a spectral image do not count as individual samples. While a technique such as SVM is expected to give improved results in comparison with PLS-DA, the

Stellenbosch University https://scholar.sun.ac.za

model would have likely had a high rate of misclassification when presented with an unknown sample set. Unfortunately, despite being collected over the course of several months during collaboration with two partners in the South African maize industry, samples of some defects were not sufficiently numerous to allow for larger sample sets in this study.

The results of this study demonstrated that NIR hyper- and multispectral imaging are promising analytical techniques for automated maize grading, but not for the detection of asymptomatic *Fusarium* infection. To further improve the classification performance of the maize grading hierarchical models, it is advised that larger sample sets are collected for each maize grading category over several harvest seasons. Not only will a larger spectral library allow for improved accuracy and robustness of the linear PLS-DA classification models, but will eventually justify their recalculation using a non-linear technique such as SVM. Furthermore, the inclusion of the visible wavebands at which anthocyanin (550 nm) and beta-carotene (450 nm) exhibit maximum absorption is recommended to further improve the classification of pinked white maize and yellow maize, respectively. Hierarchical modelling allowed for the classification of 17 classes and shows promise for extending the application of NIR hyperspectral imaging to more complex applications in the food and agro-product industries. If maize grading facilities decide to implement the spectral imaging maize classification system, a simple programme for counting the percentage of each main category can be used to determine if the content of the undesirable main categories (defective white maize kernels, pinked white maize kernels, yellow maize kernels and foreign materials) fall under the legislative limits for white maize grade WM1, WM2 or WM3 (Table 3.1 and Addendum 1). Lastly, while the asymptomatic *Fusarium* infection PLS-DA classification model did not perform as hoped, the data gathered to calibrate the model was an equally important objective of the project. No literature is currently available linking *Fusarium* infection, symptoms and fumonisin levels in South African white maize. *Fusarium* and fumonisins are an incredibly important and often frustrating issue in South African maize production, and this study further demonstrated that legislation and monitoring must be strict and insist that fumonisin testing be conducted.

REFERENCES

Bacon, C. W., Glenn, A. & Yates, I. E. (2008). Fusarium verticillioides: managing the endophytic association with maize for reduced fumonisins accumulation. *Toxin Reviews,* **27,** 411-446.

Kuldau, G. A. & Yates, I. E. (2000). Microbial endophytes. In: *Evidence for Fusarium Endophytes in Cultivated and Wild Plants* (edited by Bacon, C. W. & White, J.). Pp. 85-120. New York City, USA: CRC press.

Sendin, K., Williams, P. J., & Manley, M. (2018). Near infrared hyperspectral imaging in quality and safety evaluation of cereals. *Critical Reviews in Food Science and Nutrition, 58*(4), 575-590.

Stellenbosch University https://scholar.sun.ac.za

SUPPLEMENTARY FIGURES AND TABLES

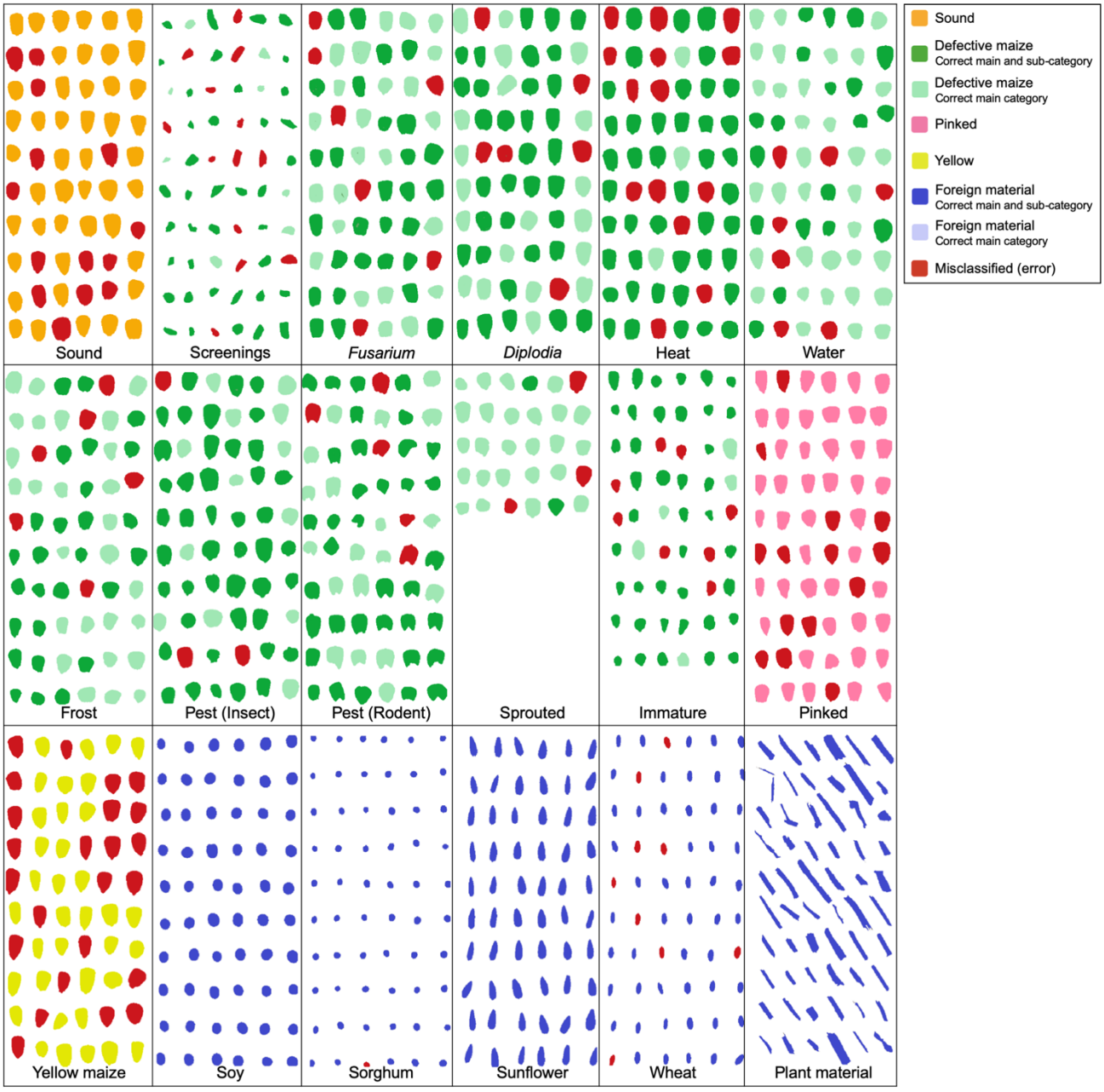

Figure S1 Classification image of the validation image dataset (1044 total) using the windows hierarchical model. Dark shaded objects indicate correct main category and sub-category classification, light shaded objects indicate correct main category classification, and red shaded objects indicate misclassification (error).

Stellenbosch University https://scholar.sun.ac.za

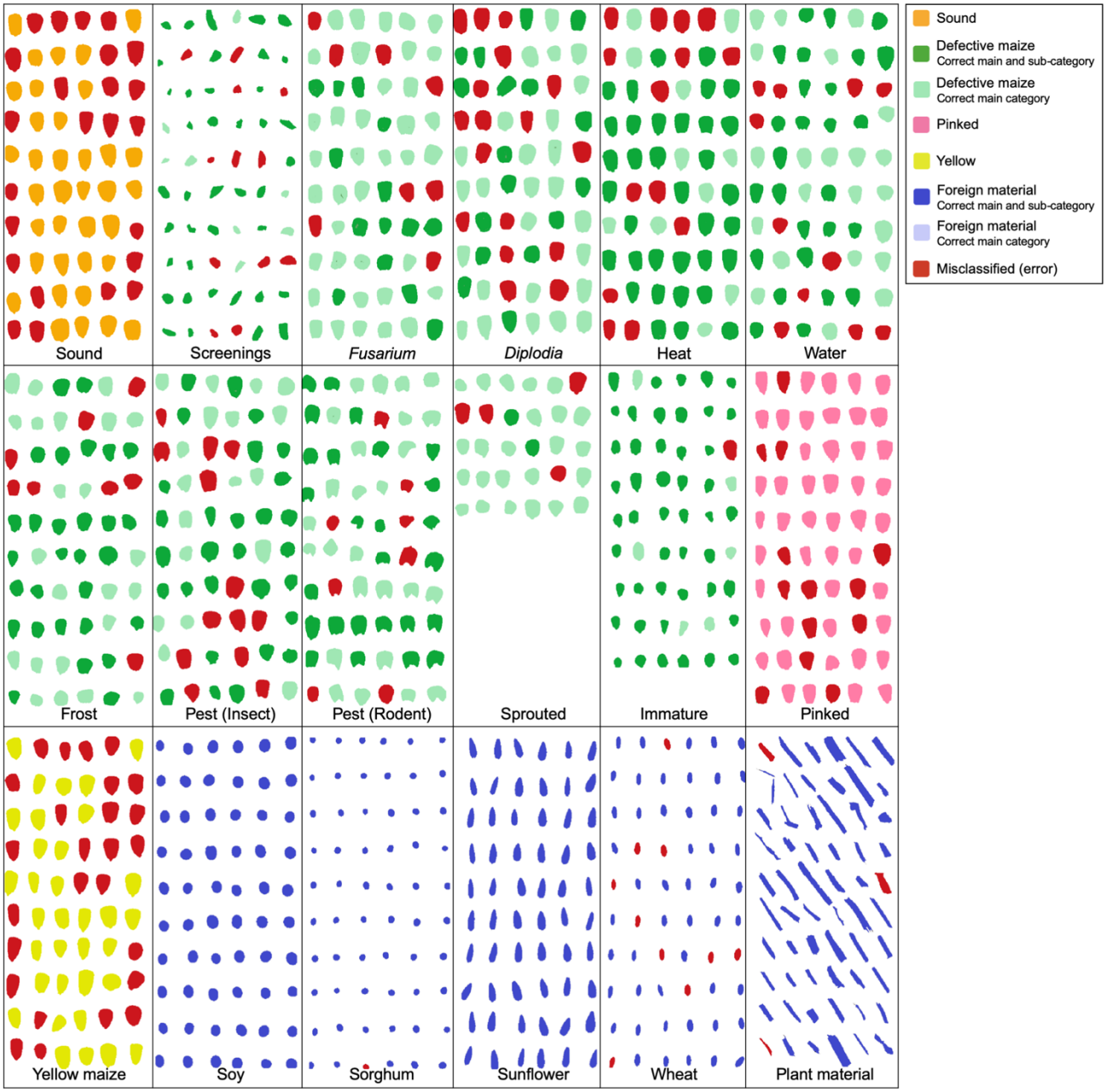

Figure S2 Classification image of the validation image dataset (1044 total) using the VIP hierarchical model. Dark shaded objects indicate correct main category and sub-category classification, light shaded objects indicate correct main category classification, and red shaded objects indicate misclassification (error).

Stellenbosch University https://scholar.sun.ac.za

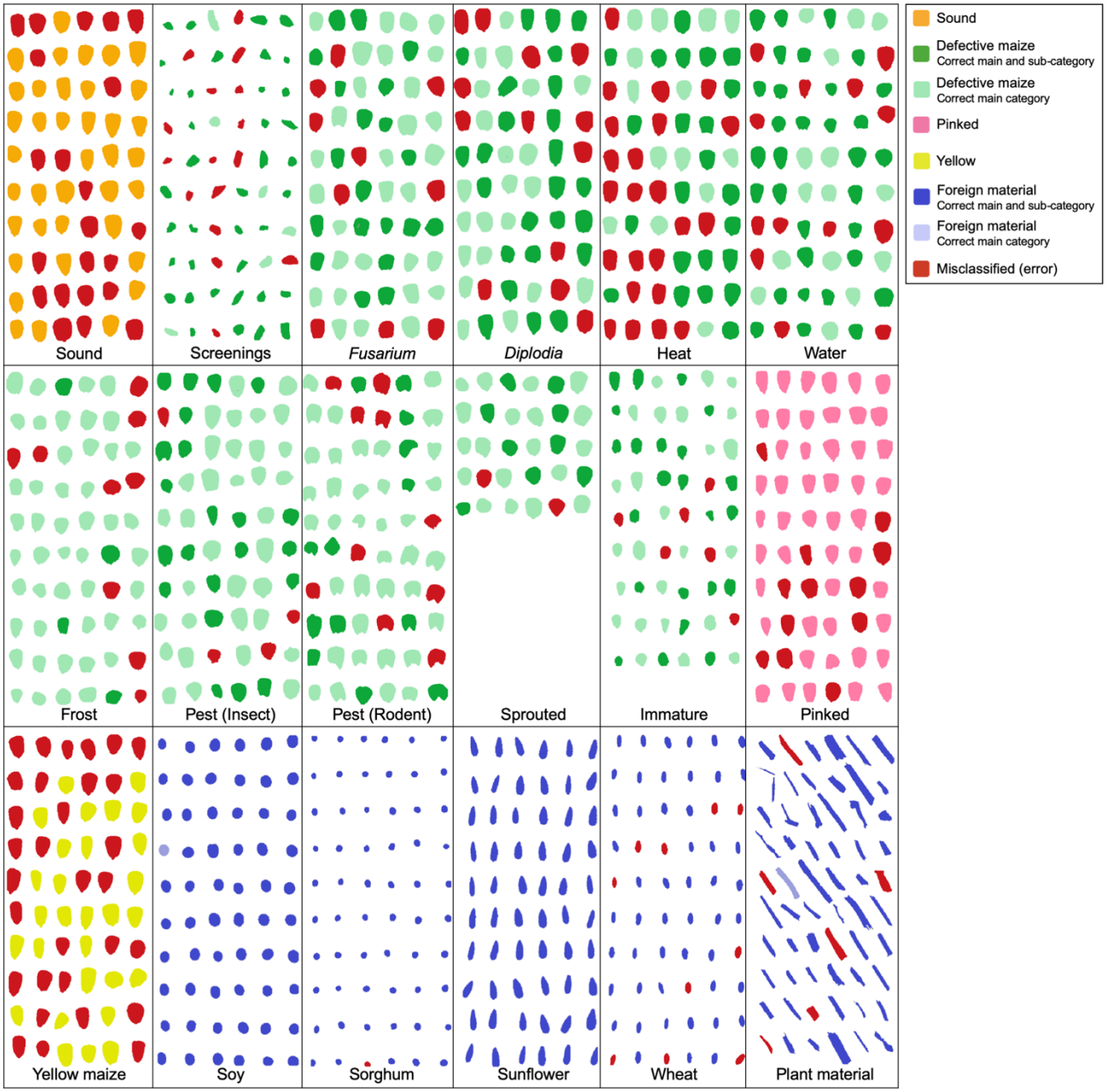

Figure S3 Classification image of the validation image dataset (1044 total) using the CovSel hierarchical model. Dark shaded objects indicate correct main category and sub-category classification, light shaded objects indicate correct main category classification, and red shaded objects indicate misclassification (error).

Stellenbosch University https://scholar.sun.ac.za

Table S1 Windows ierarchical model structure, consisting of 3 main levels, 15 sub-levels and 25 PLS-DA classification models. Each object enters the decision pathway at Level 1 and follows the relevant instructions according to classification result by the PLS-DA model.

	CLASS ONE	CLASS TWO	CLASS THREE	2nd CLASSIFICATION	LVs; Q^2
LEVEL 1: MAIZE vs. FOREIGN MATERIALS					
1	Group: sound, all defects, pinked & yellow *Proceed to LEVEL 2*	Group: soy, sorghum, sunflower, wheat & plant *Proceed to LEVEL 3*	-	-	1: 16; 0.759
LEVEL 2: MAIZE CATEGORIES & SUBCATEGORIES					
2a	Immature *Final classification 'Immature'*	Group: screenings, frost, sprouted, *Diplodia*, *Fusarium*, pest, water, sound, pinked, yellow and heat *Proceed to 2b*	-	-	2a: 14; 0.456
2b	Screenings *Proceed to 2nd classification step*	Group: frost, sprouted, *Diplodia*, *Fusarium*, pest, water, sound, pinked, yellow and heat *Proceed to 2c*	-	Screenings vs. pest *Final classification = predicted class*	2b: 9; 0.421 2nd: 12; 0.777
2c	Frost *Proceed to 2nd classification step*	Group: sprouted, *Diplodia*, *Fusarium*, pest, water, sound, pinked, yellow and heat *Proceed to 2d*	-	Frost vs. heat vs. pest *Final classification = predicted class*	2c: 13; 0.327 2nd: 14; 0.561
2d	Sprouted *Proceed to 2nd classification step*	Group:, *Diplodia*, *Fusarium*, pest, water, sound, pinked, yellow and heat *Proceed to 2e*	-	Sprouted vs. *Fusarium* vs. *Diplodia* *Final classification = predicted class*	2d: 9; 0.286 2nd: 17; 0.627
2e	*Diplodia* *Proceed to 2nd classification*	Group: *Fusarium*, pest, water, sound, pinked, yellow and heat *Proceed to 2f*	-	*Diplodia* vs. pest *Final classification = predicted class*	2e: 12; 0.329 2nd: 13; 0.575
2f	*Fusarium* *Proceed to 2nd classification*	Group: pest, water, sound, pinked, yellow and heat *Proceed to 2g*	-	*Fusarium* vs. pest *Final classification = predicted class*	2f: 13; 0.523 2nd: 13; 0.682

Stellenbosch University https://scholar.sun.ac.za

2g	Pest *Final classification 'Pest'*	Group: water, sound, pinked, yellow and heat *Proceed to 2h*	-	-	2g: 7; 0.331
2h	Water *Final classification 'Sound'*	Group: sound, pinked, yellow and heat *Proceed to 2i*	-	-	2h: 13; 0.559
2i	Sound *Proceed to 2nd classification*	Group: pinked, yellow and heat *Proceed to 2j*	-	Sound vs. pinked vs. *Diplodia* *Final classification = predicted class*	2i: 14; 0.557 2nd: 12; 0.602
2j	Pinked *Proceed to 2nd classification*	Group: yellow and heat *Proceed to 2k*	-	Pinked vs. water vs. sound *Final classification = predicted class*	2j: 11; 0.590 2nd: 14; 0.650
2k	Yellow *Proceed to 2nd classification (1)*	Heat *Proceed to 2nd classification (2)*	-	(1) Yellow vs. *Diplodia* vs. sound (2) Heat vs. *Diplodia* vs. pest *Final classification = predicted class*	2k: 9; 0.685 2nd (1): 15; 0.64 2nd (2): 15; 0.57
LEVEL 3: STARCHY vs. CELLULOSE-RICH FOREIGN MATERIALS					
3	Soy, sorghum & wheat *Proceed to 3b*	Sunflower & plant *Proceed to 3c*	-	-	3a: 4; 0.855
3b	Soy *Final classification 'Soy'*	Sorghum *Final classification 'Sorghum'*	Wheat *Final classification 'Wheat'*	-	3b: 5; 0.892
3c	Sunflower *Final classification 'Sunflower'*	Plant *Final classification 'Plant'*	-	-	3c: 2; 0.923

Stellenbosch University https://scholar.sun.ac.za

Table S2 VIP hierarchical model structure, consisting of 3 main levels, 15 sub-levels and 25 PLS-DA classification models. Each object enters the decision pathway at Level 1 and follows the relevant instructions according to classification result by the PLS-DA model.

	CLASS ONE	CLASS TWO	CLASS THREE	2nd CLASSIFICATION	LVs; Q^2
LEVEL 1: MAIZE vs. FOREIGN MATERIALS					
1	Group: sound, all defects, pinked & yellow *Proceed to LEVEL 2*	Group: soy, sorghum, sunflower, wheat & plant *Proceed to LEVEL 3*	-	-	1: 13; 0.666
LEVEL 2: MAIZE CATEGORIES & SUBCATEGORIES					
2a	Screenings *Proceed to 2nd classification step*	Group: immature, frost, sprouted, water, *Diplodia*, pest, *Fusarium*, sound, pinked, yellow and heat *Proceed to 2b*	-	Screenings vs. wheat *Final classification = predicted class*	2a: 6; 0.309 2nd: 8; 0.705
2b	Immature *Proceed to 2nd classification step*	Group: frost, sprouted, water, *Diplodia*, pest, *Fusarium*, sound, pinked, yellow and heat *Proceed to 2c*	-	Immature vs. frost vs. water *Final classification = predicted class*	2b: 12; 0.350 2nd: 12; 0.588
2c	Frost *Proceed to 2nd classification step*	Group: sprouted, water, *Diplodia*, pest, *Fusarium*, sound, pinked, yellow and heat *Proceed to 2d*	-	Frost vs. pest *Final classification = predicted class*	2c: 14; 0.185 2nd: 10; 0.623
2d	Sprouted *Proceed to 2nd classification step*	Group:, water, *Diplodia*, pest, *Fusarium*, sound, pinked, yellow and heat *Proceed to 2e*	-	Sprouted vs. *Fusarium* vs. pinked *Final classification = predicted class*	2d: 13; 0.199 2nd: 13; 0.545
2e	Water *Proceed to 2nd classification*	Group: *Diplodia*, pest, *Fusarium*, sound, pinked, yellow and heat *Proceed to 2f*	-	Water vs. pest *Final classification = predicted class*	2e: 12; 0.292 2nd: 7; 0.583
2f	*Diplodia* *Final classification = predicted class*	Group: pest, *Fusarium*, sound, pinked, yellow and heat *Proceed to 2g*	-	*Diplodia* vs. pest vs. sprouted *Final classification = predicted class*	2f: 7; 0.202 2nd: 13; 0.369

Stellenbosch University https://scholar.sun.ac.za

2g	Pest *Final classification 'Pest'*	Group: *Fusarium*, sound, pinked, yellow and heat *Proceed to 2h*	-	-	2g: 7; 0.251
2h	*Fusarium* *Final classification 'Sound'*	Group: sound, pinked, yellow and heat *Proceed to 2i*	-	-	2h: 7; 0.681
2i	Sound *Proceed to 2nd classification*	Group: pinked, yellow and heat *Proceed to 2j*	-	Sound vs. pinked vs. *Diplodia* *Final classification = predicted class*	2i: 7; 0.495 2nd: 14; 0.475
2j	Pinked *Proceed to 2nd classification*	Group: yellow and heat *Proceed to 2k*	-	Pinked vs. water vs. sound *Final classification = predicted class*	2j: 12; 0.645 2nd: 12; 0.489
2k	Yellow *Proceed to 2nd classification (1)*	Heat *Proceed to 2nd classification (2)*	-	(1) Yellow vs. pinked vs. sound (2) Heat vs. pest *Final classification = predicted class*	2k: 13; 0.539 2nd (1): 16; 0.49 2nd (2): 9; 0.463
LEVEL 3: STARCHY vs. CELLULOSE-RICH FOREIGN MATERIALS					
3	Soy, sorghum & wheat *Proceed to 3b*	Sunflower & plant *Proceed to 3c*	-	-	3a: 5; 0.790
3b	Soy *Final classification 'Soy'*	Sorghum *Final classification 'Sorghum'*	Wheat *Proceed to 2nd classification*	Wheat vs. sprouted	3b: 6; 0.886
3c	Sunflower *Final classification 'Sunflower'*	Plant *Proceed to 2nd classification*	-	Plant vs. immature *Final classification = predicted class*	3c: 4; 0.903

Stellenbosch University https://scholar.sun.ac.za

Table S3 CovSel hierarchical model structure, consisting of 3 main levels, 15 sub-levels and 25 PLS-DA classification models. Each object enters the decision pathway at Level 1 and follows the relevant instructions according to classification result by the PLS-DA model.

	CLASS ONE	CLASS TWO	CLASS THREE	2nd CLASSIFICATION	LVs; Q^2
LEVEL 1: MAIZE vs. FOREIGN MATERIALS					
1	Group: sound, all defects, pinked & yellow *Proceed to LEVEL 2*	Group: soy, sorghum, sunflower, wheat & plant *Proceed to LEVEL 3*	-	-	1: 7; 0.593
LEVEL 2: MAIZE CATEGORIES & SUBCATEGORIES					
2a	Water *Proceed to 2nd classification step*	Group: screenings, *Fusarium*, sprouted, *Diplodia*, frost, pest, immature, pinked, sound, yellow and heat *Proceed to 2b*	-	Water vs. pinked *Final classification = predicted class*	2a: 8; 0.122 2nd: 5; 0.570
2b	Screenings *Proceed to 2nd classification step*	Group: *Fusarium*, sprouted, *Diplodia*, frost, pest, immature, pinked, sound, yellow and heat *Proceed to 2c*	-	Screenings vs. pest *Final classification = predicted class*	2b: 9; 0.307 2nd: 10; 0.596
2c	*Fusarium* *Proceed to 2nd classification step*	Group: sprouted, *Diplodia*, frost, pest, immature, pinked, sound, yellow and heat *Proceed to 2d*	-	*Fusarium* vs. pest *Final classification = predicted class*	2c: 9; 0.276 2nd: 8; 0.321
2d	Sprouted *Final classification 'Sprouted'*	Group: *Diplodia*, frost, pest, immature, pinked, sound, yellow and heat *Proceed to 2e*	-	-	2d: 8; 0.197
2e	*Diplodia* *Proceed to 2nd classification*	Group: frost, pest, immature, pinked, sound, yellow and heat *Proceed to 2f*	-	*Diplodia* vs. immature *Final classification = predicted class*	2e: 6; 0.193 2nd: 7; 0.834
2f	Frost *Final classification* 'Diplodia'	Group: pest, immature, pinked, sound, yellow and heat *Proceed to 2g*	-	-	2f: 5; 0.289

Stellenbosch University https://scholar.sun.ac.za

2g	Pest *Proceed to 2nd classification*	Group: immature, pinked, sound, yellow and heat *Proceed to 2h*	-	Pest vs. sprouted *Final classification = predicted class*	2g: 9; 0.508 2nd: 7; 0.545
2h	Immature *Final classification 'Sound'*	Group: pinked, sound, yellow and heat *Proceed to 2i*	-	-	2h: 14; 0.809
2i	Pinked *Proceed to 2nd classification*	Group: sound, yellow and heat *Proceed to 2j*	-	Pinked vs. yellow *Final classification = predicted class*	2i: 7; 0.572 2nd: 10; 0.640
2j	Sound *Proceed to 2nd classification*	Group: yellow and heat *Proceed to 2k*	-	Sound vs. *Diplodia* vs. heat *Final classification = predicted class*	2j: 8; 0.568 2nd: 10; 0.366
2k	Yellow *Proceed to 2nd classification (1)*	Heat *Proceed to 2nd classification (2)*	-	(1)Yellow vs. *Diplodia* vs. sound (2) Heat vs. pinked *Final classification = predicted class*	2k: 8: 0.241 2nd (1): 9; 0.35 2nd (2): 8; 0.61
LEVEL 3: STARCHY vs. CELLULOSE-RICH FOREIGN MATERIALS					
3	Soy, sorghum & wheat *Proceed to 3b*	Sunflower & plant *Proceed to 3c*	-	-	3a: 7; 0.724
3b	Soy *Final classification 'Soy'*	Sorghum *Proceed to 2nd classification*	Wheat *Final classification 'Wheat'*	Sorghum vs. *Fusarium* vs. immature *Final classification = predicted class*	3b: 6; 0.835 2nd: 7; 0.723
3c	Sunflower *Final classification 'Sunflower'*	Plant *Proceed to 2nd classification*	-	Plant vs. screenings *Final classification = predicted class*	3c: 3; 0.882 2nd: 4; 0.593

Stellenbosch University https://scholar.sun.ac.za

ADDENDUM 1

SOUTH AFRICAN MAIZE GRADING REGULATIONS

Regulations relating to the grading, packing and marking of maize products intended for sale in the Republic of South Africa

Stellenbosch University https://scholar.sun.ac.za

DEPARTMENT OF AGRICULTURE

AGRICULTURAL PRODUCT STANDARDS ACT, 1990
(ACT No. 119 OF 1990)

REGULATIONS RELATING TO THE GRADING, PACKING AND MARKING OF MAIZE INTENDED FOR SALE IN THE REPUBLIC OF SOUTH AFRICA

The Minister of Agriculture, acting under section 15 of the Agricultural Product Standards Act, 1990 (Act No. 119 of 1990), made the regulations in the Schedule; and

(a) determined that the said regulations shall come into operation on date of publication.

SCHEDULE

Definitions

1. In these regulations any word or expression to which a meaning has been assigned in the Act shall have that meaning and, unless the context otherwise indicates -

"**bag**" means a bag manufactured from -

(a) jute or phormium or a mixture of jute and phormium; or

(b) polypropylene that complies with SABS specification CKS632;

"**bulk container**" means any vehicle or container in which bulk maize is stored or transported;

"**consignment**" means -

(a) a quantity of maize of the same class, which belongs to the same owner, delivered at any one time under cover of the same consignment note, delivery note or receipt note, or delivered by the same vehicle or bulk container, or loaded from the same bin of a grain elevator or from a ship's hold; or

(b) in the case where a quantity referred to in paragraph (a), is subdivided into different grades, each such quantity of each of the different grades;

"**container**" means a bag or a bulk container;

"**defective maize kernels**" means maize kernels and pieces of maize kernels that;

(a) are shrivelled, obviously immature, frost-damaged, mouldy or chalky;

(b) discoloured by external factors such as water and sun: Provided that discoloration on both sides of the maize kernel limited to less than a quarter from the bottom tip of the maize kernel shall not be considered as defective;

(c) have sprouted, including kernels of which the shoot (plumule) in the germ is visibly discoloured;

(d) have cavities in the germ or endosperm caused by insects or rodents;

(e) are visibly soiled (smeared) or contaminated by smut, fire, soil, smoke or coal-dust;

(f) can pass through the 6,35 mm round-hole sieve;

Stellenbosch University https://scholar.sun.ac.za

(g) are of subspecies other than *Zea mays indentata* or *Zea mays indurata*.

Provided that -

(i) irregularity of shape and size of maize kernels shall not affect the grading thereof; and

(ii) chipped or cracked maize kernels or pieces of maize kernels which are in a sound condition and which appear in a sample of maize, but which do not pass through a 6,35 mm round-hole sieve, shall not be regarded as defective maize kernels under these regulations.

"**discoloured maize kernels**" means maize kernels that are as a result of environmental conditions more than 50% discoloured on both sides of the kernel, excluding pinked maize kernels;

"**foreign matter**" means all matter other than maize, glass, stone above the sieve , coal, dung or metal;

"**frost damaged**" means maize kernels that are covered with wrinkles on both sides of the kernel to the crown and have a pearl-like appearance. Maize kernels of which the bran is flaking is considered frost damaged if signs of frost damage are present;

"**heat damaged**" means kernels that are as a result of external heat or internal fermentation affected with excess moisture and have at least one of the following characteristics:

(a) Kernels or pieces of kernels that are completely brown, dark-brown or amber discoloured.

(b) Kernels of which the germ has dark-brown to black discoloration.

"**insect**" in relation to maize, means any live insect which is injurious to stored grain, irrespective of the stage of development of the insect;

"**maize**" means the threshed kernels or pieces of kernels of the plants of *Zea mays indurata* and *Zea mays indentata* or one or more crossings of the two types;

"**mouldy**" means kernels or pieces of kernels that;

(a) are visibly infected by fungi and are characterised by black, blue, green, yellow or white fungi growth anywhere on the kernel, or are characterised by fungi growth underneath the bran layer of the kernel;

(b) are infected by ear-rot and are characterised by red, pink or brown discolorations. The kernels are partially to completely infected;

"**poisonous seeds**" means seeds or part of seeds of plant species that may in terms of the Foodstuffs, Cosmetics and Disinfectants Act, 1972 (Act No. 54 of 1972) represent a hazard to human or animal health when consumed, including seeds of *Argemone mexicana, Convolvulus* spp., *Crotalaria* spp., *Datura* spp., *Ipomoea* spp. *Lolium temulentum*, *Ricinus communis* or *Xanthium* spp.;

"**other colour maize kernels**" in relation to -

(a) white maize, means maize kernels or pieces of maize kernels of which the endosperm as a result of genetic (characteristics) composition have another colour than white, excluding pinked maize kernels;

(b) yellow maize, means maize kernels or pieces of maize kernels of which the endosperm as a result of genetic (characteristics) composition have another colour than yellow ;

"**pinked maize kernels**" means kernels and pieces of kernels of white maize of which the pericarp or part

Stellenbosch University https://scholar.sun.ac.za

thereof is shaded red or pink in colour;

"**shrivelled or obviously immature maize kernels**" means maize kernels with a thin and shrunken appearance;

"**sprouted maize kernels**" means maize kernels which have sprouted so far that developing roots and/or sprouts are clearly visible, or the shoot (plumule) in the germ is visibly discoloured;

"**the Act**" means the Agricultural Product Standards Act, 1990 (Act No. 119 of 1990); and

"**the 6,35 mm round-hole sieve**" means a sieve ;

(a) with a flat metal sheet bottom of 1,0 mm thickness perforated with round holes of 6,35 mm in diameter that are arranged with the centres of the holes at the points of intersection of an equilateral triangular grid with a pitch of 8 mm;

(b) of which the upper surface of the bottom is smooth;

(c) the frame of which is at least 40 mm high;

(d) with the inner width of at least 200 mm and the inner length of at least 300 mm, or, in the case of a circular sieve, the inner diameter of at least 278 mm; and

(e) that fits onto a tray with a solid bottom and must be at least 20 mm above the bottom of the tray.

Restrictions on sale of maize

2. (1) No person shall sell maize in the Republic of South Africa -

(a) unless the maize is sold according to the classes set out in regulation 3;

(b) unless the maize complies with the standards for the class concerned set out in regulation 4;

(c) unless the maize complies with the grades of maize and the standards for grades, where applicable, set out in regulations 5 and 6 respectively;

(d) unless the maize is packed in accordance with the packing requirements set out in regulation 7;

(e) unless the containers or sale documents, as the case may be, are marked in accordance with the marking requirements set out in regulation 8; and

(f) if such maize contains a substance that renders it unfit for human consumption or for processing into or utilisation thereof as food or feed.

(2) The Executive Officer may grant written exemption, entirely or partially to any person on such conditions as he or she may deem necessary, from the provisions of subregulation 1:Provided that such exemption is done in terms of section 3 (1) (c) of the Act.

Stellenbosch University https://scholar.sun.ac.za

QUALITY STANDARDS

Classes of maize

3. The classes of Maize shall be -

(a) Class White Maize;

(b) Class Yellow Maize; and

(c) Class Other Maize.

Standards for classes of maize

4. (1) A consignment of maize shall be classified as Class White Maize if -

(a) subject to the allowable deviation in respect of other colour maize kernels that apply to the different grades of white maize, it consists of maize the endosperm of which is by nature white in colour; and

(b) it complies with the standards for one of the grades of white maize set out in regulation 6.

(2) A consignment of maize shall be classified as Class Yellow Maize if -

(a) subject to the allowable deviation in respect of other colour maize kernels that apply to the different grades of yellow maize, it consists of maize the endosperm of which is by nature yellow in colour; and

(b) it complies with the standards for one of the grades of yellow maize set out in regulation 6.

(3) A consignment of maize shall be classified as Class Other Maize if the consignment does not comply with the standards for Class White Maize or Class Yellow Maize.

Grades of maize

5. (1) Maize of the Class White Maize shall be graded as WM1, WM2 or WM3.

(2) Maize of the Class Yellow Maize shall be graded as YM1, YM2 or YM3.

(3) No grades are determined for Class Other Maize.

Standards for grades of Class White Maize and Class Yellow Maize

6. All grades of maize -

(a) shall be free from a musty, sour or other undesired odour;

(b) shall be free from glass, metal, coal or dung;

(c) shall be free from a substance which renders it unfit for human consumption or for processing into or utilisation thereof as food or feed;

(d) shall be free from insects;

(e) shall be free from stones which cannot pass through the 6,35 mm round-hole sieve;

Stellenbosch University https://scholar.sun.ac.za

(f) shall contain not more than one gram of stones, which can pass through the 6,35 mm round-hole sieve, per 10 kg;

(g) shall contain not more poisonous seeds than permitted in terms of the Foodstuffs, Cosmetics and Disinfectants Act, 1972 (Act No. 54 of 1972);

(h) shall have a moisture content of not more than 14 per cent; and

(i) shall not exceed the maximum percentage of permissible deviation as determined in the table in the Annexure for each grade.

II
PACKING AND MARKING REQUIREMENTS

Packing requirements

7. Maize of different classes and grades shall be packed in different containers.

Marking requirements

8. Each container or the accompanying sales documents of a consignment of maize shall be marked or endorsed with -

(a) the class of the maize; and

(b) the grade, in the case of Class White Maize or Class Yellow Maize.

III
SAMPLING

Obtaining sample

9. (1) A sample of a consignment of maize shall -

(a) in the case of maize delivered in bags and subject to regulation 10, be obtained by sampling at least ten per cent of the bags, chosen from that consignment at random, with a bag probe: Provided that at least 25 bags in a consignment shall be sampled and where a consignment consists of less than 25 bags, all the bags in that consignment shall be sampled; and

(b) in the case of maize delivered in bulk and subject to regulation 10, be obtained by sampling that consignment throughout the whole depth of the layer, in at least six different places, chosen at random in that bulk quantity, with a bulk sampling apparatus.

(2) The collective sample obtained in subregulation (1) (a) or (b) shall -

(a) have a total mass of at least 10 kg; and

(b) be thoroughly mixed before further dividing.

(3) If it is suspected that the sample referred to in subregulation (1)(a) is not representative of that consignment, an additional five per cent of the remaining bags, chosen from that consignment at random, shall be emptied into a suitable bulk container and sampled in the manner contemplated in subregulation (1)(b).

(4) A sample taken in terms of these regulations shall be deemed representative of the consignment from which it was taken.

Stellenbosch University https://scholar.sun.ac.za

Sampling if contents differ

10. (1) If, after an examination of the maize taken from different bags in a consignment in terms of regulation 9(1), it appears that the contents of those bags differ substantially -

(a) the bags concerned shall be placed separately;

(b) all the bags in the consignment concerned shall be sampled in order to do such separation; and

(c) each group of bags with similar contents in that consignment shall for the purposes of these regulations be deemed to be a separate consignment.

(2) If, after the discharge of a consignment of maize in bulk has commenced, it is suspected that the consignment could be of a class or grade other than that determined by means of the initial sampling, the discharge shall immediately be stopped and the part of the consignment remaining in the bulk container, as well as the grain that is already in the collecting tray, shall be sampled anew with a bulk sampling apparatus or by catching at least 20 samples at regular intervals throughout the whole offloading period with a suitable container from the stream of grain that is flowing in bulk.

Working sample

11. A working sample shall be obtained by dividing the representative sample of the consignment according to the ICC 101/1 (Approved 1982) method.

IV
DETERMINATION OF OTHER SUBSTANCES

Determination of undesirable odours and harmful substances

12. A sample of a consignment of maize shall be sensorial assessed or chemically analysed in order to determine -

(a) whether it has a musty, sour or other undesirable odour; and

(b) whether it contains a substance that renders the maize unfit for human consumption or for processing into or for utilisation as food or feed.

Determination of glass, metal, coal, dung, stone, poisonous seed and insect content

13. A consignment of maize shall be sensorial assessed and a sample of that consignment shall be sensorial assessed and sorted by hand in order to determine whether the sample contains glass, metal, coal, dung, insects, stones and poisonous seeds.

Determination of percentage of foreign matter

14. The percentage of foreign matter in a consignment of maize shall be determined as follows:

(a) Obtain a working sample with a mass of at least 150g from the sample of the consignment.

(b) Remove all foreign matter from the working sample and determine the mass thereof.

(c) Express the mass thus determined as a percentage of the total mass of the working sample.

(d) Such percentage shall represent the percentage of foreign matter in the consignment concerned.

Stellenbosch University https://scholar.sun.ac.za

V
MAIZE KERNELS

Determination of percentage of defective maize kernels

15. The percentage of defective maize kernels in a consignment of maize shall be determined as follows:

(a) Obtain a working sample with a mass of at least 150g from the sample of the consignment.

(b) Place the working sample on the 6, 35 mm round-hole sieve that is fitted onto a matching tray, sieve it in such a manner that all the material on the sieve passes at least 20 times over the entire surface of the sieve and determine the mass of the maize kernels and pieces of maize kernels that passed through the sieve.

(c) Express the mass determined in terms of paragraph (b) as a percentage of the total mass of the working sample.

(d) Remove all defective maize kernels from that part of the working sample remaining on the sieve and determine the mass of the defective maize kernels thus removed.

(e) Express the mass determined in terms of paragraph (d) as a percentage of the total mass of the working sample.

(f) Calculate the sum total of the masses determined in terms of paragraphs (b) and (d).

(g) Express the combined mass calculated in terms of paragraph (f) as a percentage of the total mass of the working sample.

(h) In the case of yellow maize the percentage obtained -

(i) in terms of paragraph (c), represents the percentage of defective maize kernels in the consignment concerned, which can pass through the 6,35 mm round-hole sieve; and

(ii) in terms of paragraph (e), represents the percentage of defective maize kernels in the consignment concerned, which can not pass through the 6,35 mm round-hole sieve.

(i) In the case of white maize, the percentage obtained in terms of paragraph (g) represents the percentage of defective maize kernels in the consignment concerned.

Determination of percentage of other colour maize kernels

16. The percentage of other colour maize kernels in a consignment of maize shall be determined as follows:

(a) Obtain a working sample with a mass of at least 150g from the sample of the consignment.

(b) Remove all other colour maize kernels from the working sample and determine the mass thereof.

(c) Express the mass thus determined as a percentage of the total mass of the working sample.

(d) Such percentage shall represent the percentage of other colour maize kernels in the consignment concerned.

Stellenbosch University https://scholar.sun.ac.za

Determination of percentage of pinked maize kernels

17. The percentage of pinked maize kernels in a consignment of maize shall be determined as follows:

(a) Obtain a working sample with a mass of at least 150g from the sample of the consignment.

(b) Remove all pinked maize kernels from the working sample and determine the mass thereof.

(c) Express the mass thus determined as a percentage of the total mass of the working sample.

(d) Such percentage shall represent the percentage of pinked maize kernels in the consignment concerned.

VI
MOISTURE CONTENT

Determination of moisture content

18. The moisture content of a consignment of maize may be determined according to any suitable method: Provided that the results thus obtained are in accordance with the maximum permissible deviation for a class 1 moisture meter as detailed in ISO 7700/1-1994(E) based on the results of the 72 hour, 103°C oven dried method (AACC Method 44/15A/1981).

VII
OFFENCE AND PENALTIES

19. Any person who contravenes or fails to comply with any provision of these regulations shall be guilty of an offence and upon conviction be liable to a fine or imprisonment in terms of section 11 of the Act.

Stellenbosch University https://scholar.sun.ac.za

ANNEXURE/AANHANGSEL
TABLE/TABEL

STANDARDS FOR GRADES OF CLASS WHITE MAIZE AND CLASS YELLOW MAIZE/
STANDAARDE VIR GRADE VAN KLAS WITMIELIES EN KLAS GEELMIELIES

	Maximum permissible deviation/ Maksimum toelaatbare afwyking					
Deviation/Afwyking	White maize/ Witmielies			Yellow maize/ Geelmielies		
	WM1	WM2	WM3	YM1	YM2	YM3
1	2	3	4	5	6	7
1. Foreign matter [regulation 14] Vreemde voorwerpe [regulasie 14]	0,3%	0,5%	0,75%	0,3%	0,5%	0,75%
2. Defective maize kernels, above and below the 6,35 mm round-hole sieve [regulations 15,]/ Gebrekkige mieliepitte, bo en onder die 6,35 mm-rondegatsif [regulasies 15,]	7%	13%	30%	9%	20%	30%
3. Other colour maiz kernels [regulation 16]/Mieliepitte van 'n ander kleur [regulasie 16]	3%	6%	10%	3%	6%	10%
4. Deviations referred to in items 1, 2, and 3 collectively: Provided that the deviations are individually within the specified limits/Afwykings in items 1, 2, en 3 bedoel, gesamentlik: Met dien verstande dat die afwykings individueel binne die gespesifiseerde perke is	8%	16%	30%	9%	20%	30%
5. Pinked maize kernels [regulation 17]/ Verrooide mieliepitte [regulasie 17]	20%	20%	*	*	*	*

* Not specified/Nie gespesifiseer nie.